



1 Critical Load Exceedances for North America and Europe using an
2 Ensemble of Models and an Investigation of Causes for Environmental
3 Impact Estimate Variability: An AQMEII4 Study

4 Paul A. Makar¹, Philip Cheung¹, Christian Hogrefe², Ayodeji Akingunola¹, Ummugulsum Alyuz-
5 Ozdemir³, Jesse O. Bash², Michael D. Bell⁴, Roberto Bellasio⁵, Roberto Bianconi⁵, Tim Butler⁶, Hazel
6 Cathcart¹, Olivia E. Clifton^{7,8}, Alma Hodzic⁹, Iannis Kioutsioukis¹⁰, Richard Kranenburg¹¹, Aura
7 Lupascu^{6,12}, Jason A. Lynch¹³, Kester Momoh³, Juan Luis Perez-Camanyo¹⁴, Jonathan Pleim², Young-Hee
8 Ryu¹⁵, Roberto San Jose¹⁴, Donna Schwede^{2,16}, Thomas Scheuschner¹⁷, Mark Shephard¹, Ranjeet S.
9 Sokhi³, Stefano Galmarini¹⁸

- 10 [1] Environment and Climate Change Canada, Toronto, Canada
11 [2] ORD, U.S. EPA, Research Triangle Park, NC, USA
12 [3] Centre for Climate Change Research (C3R), U. Hertfordshire, UK
13 [4] Air Resources Division, US National Park Service, USA
14 [5] Enviroware srl, Concorezzo, MB, Italy
15 [6] Research Institute for Sustainability – Helmholtz Centre Potsdam, Germany
16 [7] NASA Goddard Institute for Space Studies, New York, NY, USA
17 [8] Center for Climate Systems Research, Columbia University, New York, NY, USA
18 [9] NCAR, Boulder, CO, USA
19 [10] Department of Physics, University of Patras, Patras, Greece
20 [11] NOASR, Utrecht, the Netherlands
21 [12] ECMWF, Bonn, Germany
22 [13] OAR, US EPA, USA
23 [14] Tech. U. of Madrid (UPM), Madrid, Spain
24 [15] Yonsei University, Seoul, South Korea
25 [16] (Retired)
26 [17] CCE/Federal Environment Agency, Germany
27 [18] JRC, European Commission, Ispra, Italy
28

29 Correspondence to: Paul Andrew Makar (paul.makar@ec.gc.ca)

30 **Abstract**

31 Exceedances of critical loads for deposition of sulphur (S) and nitrogen (N) to different ecosystems were
32 estimated using European and North American ensembles of air quality models, under Phase 4 of the Air
33 Quality Model Evaluation International Initiative (AQMEII4), to identify where risk of ecosystem harm is
34 expected to occur based on model deposition estimates. The ensembles were driven by common
35 emissions and lateral boundary condition inputs. Model output was regridded to common North
36 American and Europe 0.125° resolution domains, which were then used to calculate critical load
37 exceedances. New, targeted deposition diagnostics implemented in AQMEII4 allowed an unprecedented
38 level of post-simulation analysis to be carried out and facilitated the identification of specific causes of
39 model-to-model variability in critical load exceedance estimates.

40 New datasets for North American critical loads for acidity for forest soil water and aquatic ecosystems
41 were combined with the ensemble deposition predictions to show a substantial decrease in the area and
42 number of locations in exceedance between 2010 and 2016 (forest soils: 13.2% to 6.1%; aquatic
43 ecosystems: 21.2% to 11.4%). All models agreed in the direction of the ensemble exceedance change



44 between 2010 and 2016. The North American ensemble also predicted a decrease in both severity and
45 total area in exceedance between the years 2010 and 2016 for eutrophication-impacted ecosystems in the
46 USA (sensitive epiphytic lichen: 81.5% to 75.8%). The exceedances for herbaceous community richness
47 also decreased between 2010 and 2016, from 13.9% to 3.9%. The uncertainty associated with the North
48 American eutrophication results is high; there were sharp differences between the models in both
49 predictions of total N deposition and the change in N deposition, and hence in the predicted
50 eutrophication exceedances between the two years. The European ensemble was used to predict
51 relatively static exceedances of critical loads with respect to acidification (4.48% to 4.32% from 2009 to
52 2010) while eutrophication exceedance increased slightly (60.2% to 62.2%).

53 While most models showed the same changes in critical load exceedances as the ensemble between the
54 two years, the spatial extent and magnitude of exceedances varied significantly between the models. The
55 reasons for this variation were examined in detail by first ranking the relative contribution of different
56 sources of sulphur and nitrogen deposition in terms of deposited mass and model-to-model variability in
57 that deposited mass, followed by their analysis using AQMEII4 diagnostics, along with evaluation of the
58 most recent literature.

59 All models in both the North American and European ensembles had net annual negative biases with
60 respect to observed wet deposition of sulphate, nitrate and ammonium. Diagnostics and recent literature
61 suggest that this bias may stem from insufficient cloud scavenging of aerosols and gases, and may be
62 improved through the incorporation of multiphase hydrometeor scavenging within the modelling
63 frameworks. The inability of North American models to predict the timing of the seasonal peak in wet
64 ammonium ion deposition (observed maximum was in April, while all models predicted a June
65 maximum) may also relate to the need for multiphase hydrometeor scavenging (absence of snow
66 scavenging in all models employed here). High variability in the relative importance of particulate
67 sulphate, nitrate and ammonium deposition fluxes between models was linked to the use of updated
68 particle dry deposition parameterizations in some models. However, recent literature and further
69 development of some of the models within the ensemble suggests these particulate biases may also be
70 ameliorated via the incorporation of multiphase hydrometeor scavenging. Annual sulphur and nitrogen
71 deposition prediction variability was linked to SO₂ and HNO₃ dry deposition parameterizations, and
72 diagnostic analysis showed that the cuticle and soil deposition pathways dominate the deposition mass
73 flux of these species. Further work improving parameterizations for these deposition pathways should
74 reduce variability in model acidifying gas deposition estimates. The absence of base cation chemistry in
75 some models was shown to be a major factor in positive biases in fine mode particulate ammonium and
76 particle nitrate concentrations. Models employing ammonia bidirectional fluxes had both the largest and
77 the smallest magnitude biases, depending on the model and bidirectional flux algorithm employed. A
78 careful analysis of bidirectional flux models suggests that those with poor NH₃ performance may
79 underestimate the extent of NH₃ emissions fluxes from forested areas.

80 Based on these results, an increased process-research focus is therefore recommended for the following
81 model processes and on observations which may assist in model evaluation and improvement:
82 multiphase hydrometeor scavenging combined with updated particle dry deposition, cuticle and soil
83 deposition pathway algorithms for acidifying gases, base cation chemistry and emissions, and NH₃
84 bidirectional fluxes. Comparisons with satellite observations suggest that oceanic NH₃ emissions sources
85 should be included in regional chemical transport models. The choice of land use database employed
86 within any given model was shown to significantly influence deposition totals in several instances, and
87 employing a common land use database across chemical transport models and critical load calculations is
88 recommended for future work



89 Introduction

90 The concept of a Critical load (CL) was first proposed as a means for evaluating the ecosystem impacts of
91 the deposition of sulphur and nitrogen in response to the Convention on Long-Range Transboundary Air
92 Pollution (CLRTAP), an international agreement for mitigation and control of acidifying pollution, which
93 entered into force in 1983 (CLRTAP, 2023). The Convention provided some of the initial impetus for the
94 development of comprehensive air-quality models. The models provide a means of estimating the
95 deposition fluxes of sulphur- and nitrogen-containing chemicals of anthropogenic origin, which may then
96 be used to estimate the corresponding ecosystem impacts. Critical load exceedance estimates are the
97 broadly accepted methodology for estimating the potential for ecosystem harm related to acidification and
98 eutrophication. A critical load in this context was defined (Nilsson and Grennfelt, 1988) as “A
99 quantitative estimate of an exposure to one or more pollutants below which significant harmful effects on
100 specified sensitive elements of the environment do not occur, according to present knowledge”. This
101 definition is parsed in detail for readers unfamiliar with the Critical Load concept, in the Supplemental
102 Information (SI).

103 The creation of critical loads for acidification, and the calculation of their exceedances is based on the
104 concept of chemical charge balance steady-state within soil water or aquatic ecosystems. The fluxes of
105 anions and cations entering or leaving an ecosystem are used to determine whether an excess cation flux
106 is available to the ecosystem, which could balance anion fluxes associated with acidifying deposition.
107 Anion fluxes added to the system from anthropogenic sources include forms of deposited sulphur and
108 nitrogen noted above. The S-containing forms of deposition (S_{dep}) are assumed to rapidly oxidize and are
109 treated within critical load calculations as the sulphate ion. Every mole of deposited sulphur is assumed
110 to be associated with two negative charges as the sulphate ion, $\text{SO}_4^{2-}(\text{aq})$, hence the deposition flux is
111 tracked as *charge equivalents per hectare per year*; $\text{eq ha}^{-1} \text{ yr}^{-1}$. N-containing forms of deposition (N_{dep})
112 are assumed to rapidly oxidize and are treated as the nitrate ion - every mole of deposited nitrogen
113 (including those of ammonia and ammonium) is assumed to be associated with one negative charge of
114 nitrate ion deposition, $\text{NO}_3^-(\text{aq})$. Base cations and their deposition (Ca^{2+} , Mg^{2+} , K^+ , and Na^+) are
115 included in critical load calculations (collectively, BC_{dep}), and may incorporate anthropogenic base cation
116 fluxes. The anthropogenic deposition fluxes to the ecosystem from the atmosphere are used in
117 calculations of critical load exceedances. The critical loads themselves include estimates of natural
118 atmospheric fluxes as well as other terms for fluxes of anions and cations. For example, in the steady-
119 state or simple mass balance model (SMB) often used to define surface water critical loads for terrestrial
120 ecosystems (Sverdrup and DeVries, 1994), BC_{dep} includes the release of soil base cations due to
121 weathering, non-marine chloride deposition, harvesting of base cation and/or nitrogen-containing
122 biomass, denitrification, nitrogen immobilization in the rooting zone, run-off volume, and a critical value
123 of the non-sodium base cation to aluminum ion ratio. Aquatic ecosystem critical loads with respect to
124 acidity are usually calculated using the steady-state water chemistry (SSWC) or the first-order acidity
125 balance (FAB) methodologies (Henriksen and Posch, 2001; CLRTAP2023, de Vries *et al.*, 2015), or other
126 similar approaches (McDonnell *et al.*, 2014). The SSWC makes use of the difference between an
127 estimate of the sea-salt corrected pre-acidification concentration of base cations in the surface water, and
128 a specified biological indicator species' acid neutralizing capacity limit above which no significant
129 damage is expected to occur. The FAB methodology assumes the runoff fluxes at a lake outlet are charge-
130 balanced, relates these runoff terms to fluxes of ions entering the lake and dimensionless retention factors
131 and to terms for nitrogen immobilization, nitrogen growth uptake into vegetation, denitrification,
132 atmospheric deposition, and weathering. An overview of the above methods for critical load (CL)



133 estimation, and how they are used in estimating exceedances, may be found in CLRTAP (2023), Makar *et*
134 *al.* (2018) and the references therein.

135 Critical loads of nutrient nitrogen and their exceedances are used to address the issue of the influx of
136 airborne nitrogen resulting in changes in soil-based processes, plant growth and inter-species
137 relationships. Nitrogen-containing gases and aerosol components may be directly toxic to sensitive
138 individual plant and animal species, while the accumulation of nitrogen (increased nitrogen availability)
139 may also change species composition or relative abundance. Soil-mediated effects of acidification may
140 include eutrophication, and species may have increased susceptibility to secondary stressors such as
141 drought, frost, pathogens or herbivores (CLRTAP, 2023). Critical loads for the eutrophication processes
142 associated with nutrient nitrogen in terrestrial ecosystems may also make use of a version of the SMB
143 model. This critical load model balances the input fluxes of all forms of nitrogen deposition plus
144 biological fixation and soil nitrogen adsorption against ecosystem nitrogen losses (immobilization in soil
145 organic matter, removal via harvesting of vegetation and animals, fluxes to the atmosphere
146 (denitrification), erosion, combustion, ammonia volatilization, and leaching below the root zone).
147 Biological fixation, soil adsorption, combustion, erosion and ammonium leaching are usually considered
148 negligible, and denitrification is assumed to be linearly dependent on the net input of nitrogen, leading to
149 critical loads of nutrient nitrogen dependent only on immobilization, harvesting removal, a sensitive plant
150 or animal species acceptable limit for nitrogen leaching (nitrogen in soil water), and an ecosystem-
151 dependent denitrification fraction (CLRTAP, 2023). The acceptable limits for nitrogen concentrations in
152 soil can range from 6.5 down to 0.2 mg N l^{-1} , depending on vegetation type (CLRTAP, 2023). A further
153 means of estimating eutrophication is via comparison of measured nitrogen deposition with observed
154 ecosystem damage over a large number of sites (Geiser *et al.* 2019; Simkin *et al.* 2016). Exceedances for
155 eutrophication in this case may be estimated as the differences between the estimated nitrogen deposition
156 and the observation-based critical load.

157 As noted in the Supplement, critical load exceedance calculations are carried out on an ongoing basis due
158 to the ongoing cycle of chemical transport model (CTM) process improvement. The results of our
159 analyses should thus be considered a “snapshot” of the state of both CTM science and critical load (CL)
160 knowledge at the time the simulations and critical load data collection took place. CTMs numerically
161 integrate the system of time-dependent differential equations describing the rates of change of chemical
162 species in the atmosphere, in order to predict the changes in chemical concentrations and deposition over
163 time. This is usually done by breaking the net differential equation for the rates of change into component
164 processes (e.g. advection, diffusion, gas-phase chemistry, inorganic particle chemistry, dry deposition,
165 particle microphysics treating the nucleation, condensation of gases, coagulation of particles, cloud
166 processing of gases and aerosols including wet deposition), with the processes being solved in sequence
167 to determine the future state of the atmosphere (Marchuk, 1990). However, there is usually not a
168 complete scientific consensus on the best numerical methods to carry out the time-stepping for each of
169 these processes, and the level of detail in process representation in the models may also vary considerably,
170 depending at times on external constraints such as the processing time available for CTM simulations.
171 The individual processes are usually evaluated based on laboratory or other process-specific data
172 wherever possible, but often the selection of a specific process representation within a CTM is often
173 based on comparisons of the output of entire CTM relative to surface or satellite monitoring data. This
174 latter approach may allow compensating errors in process representation to take place (c.f. Makar *et al.*,
175 2014; Hyder *et al.*, 2018; Huang *et al.*, 2021; Vizueté *et al.*, 2022). These considerations may contribute
176 to the resulting variability in deposition estimates from the different modelling frameworks. The work
177 conducted here, through process analysis, attempts to determine the key causes of these model deposition
178 estimate differences.



179 The ongoing reevaluation and improvement of CTMs is aided by ensemble model comparisons, where
180 models driven by the same lateral boundary and emissions inputs are cross-compared and evaluated
181 against observations. The Air-Quality Model Evaluation International Initiative (AQMEII) has comprised
182 model CTM ensemble evaluation studies, to date in four phases. The initial phase of AQMEII utilized
183 largely off-line regional models used for research and public policy support to simulate a common year,
184 2006, with common emissions inputs, in both North America and Europe, with 22 modelling groups
185 participating (Galmarini *et al.*, 2012). Subsequent phases of AQMEII examined specific issues within the
186 CTM community: AQMEII-2 had as its focus the evaluation of both weather and air-quality predictions
187 for fully coupled, on-line air-quality models, where the particulate matter generated by the models on any
188 given timestep feeds back into the coupled models' weather forecast radiative transfer and cloud
189 formation processes (Galmarini *et al.*, 2015). AQMEII-3 addressed questions of hemispheric transport of
190 air pollutants – the relative contributions of local versus long-range transport towards predicted pollutant
191 concentrations, and their impacts on ecosystem and human health (Galmarini *et al.*, 2017).

192 The variety in underlying scientific theory encapsulated within CTMs and their process representation
193 implies the need for cross-comparison of critical load exceedance predictions from a variety of models.
194 As part of AQMEII-3, 14 air-quality models were used to calculate oxidized sulphur and oxidized and
195 reduced nitrogen deposition, and hence EU critical load exceedances (Vivanco *et al.*, 2018). This
196 comparison revealed a high degree of variability in simulated wet and dry deposition fluxes. The models
197 with the best performance relative to observations were used to provide ensemble critical loads –
198 however, even within this reduced ensemble, local variations of over a factor of four in both sulphur and
199 nitrogen deposition could be seen between the ensemble members, and the predicted percent area in
200 exceedance for sensitive ecosystems varied by more than a factor of two for the best performing models.
201 (Vivanco *et al.*, 2018). These results highlighted the large range of model-dependent variability possible
202 in critical load exceedance estimates – but the causes for that variability, and how it might be reduced,
203 were not investigated to any significant extent.

204 The study protocols of AQMEII phase four (AQMEII4) were designed partly in response to the large
205 variation in model sulphur and nitrogen deposition estimates noted in Vivanco *et al.* (2018), Solazzo *et al.*
206 (2018) and Hogrefe *et al.* (2020). AQMEII4 protocols were also motivated by a similarly large variation
207 in simulated ozone deposition velocities (Hardacre *et al.*, 2015; Zhiyong Wu *et al.*, 2018), and renewed
208 emphasis on the importance of specific ozone deposition pathways (Clifton *et al.*, 2017, 2020a,b).

209 AQMEII4 has two main activities: a regional model intercomparison with enhanced diagnostics for gas-
210 phase dry deposition (Galmarini *et al.*, 2021), and an observation-driven single-point model
211 intercomparison study for ozone dry deposition at sites with ozone flux records (Clifton *et al.*, 2023). The
212 current work continues the regional model intercomparison driven by common boundary conditions, with
213 a focus here on critical load exceedances for acidity and eutrophication, and the use of additional
214 diagnostics to determine the underlying causes for the model-to-model variability in these exceedance
215 estimates.

216 As described later in our analysis, two processes account for much of the variability in CTM predictions
217 of the total deposition of sulphur and nitrogen (S_{dep} and N_{dep}): particle dry deposition and the scavenging
218 of particles by depositing hydrometeors. We note that subsequent to the construction and application of
219 the model versions applied in AQMEII4, new parameterizations for particle dry deposition became
220 available. Emerson *et al.* (2020) compiled multiple particle dry deposition velocity observations and
221 compared these to the predictions of the commonly used Zhang *et al.* (2001) algorithm. Relative to these
222 observations, the Zhang *et al.* (2001) algorithm tended to overestimate deposition velocity on vegetated
223 surfaces at smaller particle sizes ($<0.4 \mu\text{m}$ diameter), while underestimating the deposition velocity for



224 particles between 1 and 10 μm). The accumulation mode of atmospheric particles tend to poorly capture
225 the relationship between particle deposition velocity and particle size in the accumulation mode (Clifton
226 *et al.*, 2024). Emerson *et al.* (2020) also noted a substantial overestimate of the Zhang *et al.* (2001)
227 particle deposition velocity over water surfaces relative to observations. Emerson *et al.* (2020) proposed
228 a modified version of the Zhang *et al.* (2001) algorithm, demonstrating a better fit to the ensemble of
229 deposition velocity observations. The differences between the two parameterizations were substantial,
230 with decreases in particle deposition velocities in the sub- μm range of one to two orders of magnitude
231 relative to Zhang *et al.* (2001) across multiple land use types, and increases over vegetated surfaces of up
232 to an order of magnitude for particle diameters from 1 to 10 μm . The decrease in sub- μm deposition
233 velocities might be expected to result in increases in air concentrations of Aitken to mid-Accumulation
234 mode particles, and decreases in those of mid-Accumulation mode to Coarse-mode particles. Ryu and
235 Min (2022) applied the Emerson *et al.* (2020) parameterization to the WRF-Chem model, and found that
236 PM_{2.5} positive biases increased in magnitude, while PM₁₀ negative biases were partially offset with the
237 use of the new algorithm. Pleim *et al.* (2022) also re-examined aerosol dry deposition velocities in the
238 context of the CMAQ model, noting an increase in accumulation mode dry deposition velocities of almost
239 an order of magnitude in forested areas, an overall reduction in PM_{2.5} concentrations, and an
240 improvement in PM_{2.5} prediction accuracy. The latter work does not necessarily contradict the Emerson
241 *et al.* (2020) results, which imply possible increases in PM mass within the Aitken and Accumulation
242 modes. The increase in the removal of mass between the mid-Accumulation mode to larger sizes may
243 dominate over the particle deposition velocity decreases between the Aitken to mid-Accumulation mode
244 noted in the observations collected by Emerson *et al.* (2020).

245 Studies using sectional aerosol size representations have recently found that improved aerosol deposition
246 velocity algorithms need to be combined with improved wet hydrometeor scavenging, to result in net
247 improvements of regional model performance. Ryu and Min (2022) found that the best overall WRF-
248 Chem performance resulted from a combination of updates (when the new dry deposition algorithm was
249 combined with updates for cloud scavenging employing cloud fractions for rainout and a revised
250 parameterization for below-cloud scavenging incorporating separate terms for rain and snow removal
251 rates). Ghahreman *et al.* (2024), in updating the cloud scavenging parameterization of the GEM-MACH
252 model, noted differences in rain and snow below-cloud scavenging rates of up to two orders of magnitude
253 between the previously applied, temperature-based parameterization Slinn (1984) and the newly
254 implemented parameterization of multiphase scavenging (from both the underlying meteorological model
255 and the empirical scavenging parameterization of Wang *et al.* (2014)). Differences in scavenging rates
256 were found to be strongly dependent on temperature, aerosol size, and the precipitation rate. The revised
257 parameterizations resulted in an overall improvement in performance for wet SO_4^{2-} deposition, where the
258 Emerson *et al.* (2020) algorithm was employed for the particle dry deposition simulation in all the model
259 runs.

260 A large part of the model-to-model variability and uncertainty resides in the above two processes, as
261 demonstrated in our analysis. We next describe our methodology (including an overview of the two
262 AQMEII4 model domains, descriptions of the construction of the critical load data employed herein, and
263 descriptions of the models, their inputs and boundary conditions). Our analysis follows, first presenting
264 estimates of critical load exceedances for two different simulation years in each domain, and the
265 exceedances estimated using ensembles of model deposition predictions. The bulk of the analysis then
266 examines individual contributions of different sulphur and nitrogen species towards their total deposition,
267 for each model, and for the ensemble. The causes of the differences between the models are determined
268 through process analysis. Our concluding section includes research recommendations based on the



269 analysis in order to improve the performance of individual models, and to reduce the variability between
270 their estimates of critical load exceedances.

271 Methodology

272 1.0 Critical Load Data

273 Six critical load (CL) datasets were used in conjunction with our ensembles of CTM deposition
274 estimates. North American CL datasets included terrestrial (forest) ecosystem acidity critical loads for the
275 continent, aquatic ecosystem acidity critical loads combining data from Canada and the USA, and USA-
276 specific sensitive epiphytic lichen species and herbaceous plant species eutrophication critical loads.
277 European CL datasets combined CL information from multiple countries for terrestrial and aquatic
278 ecosystem acidity and terrestrial ecosystem eutrophication. Each CL dataset is described in this section.

279 1.1 North American Forest Soil Critical Loads of Acidity using the Steady-State Mass Balance Model

280 Forest soil critical loads maps were assembled from several studies within the U.S. and Canada (Figure 1
281 and Table 1). Critical loads were (in all but one study) calculated using the Steady-State (or Simple) Mass
282 Balance (SMB) model (Sverdrup & Warfvinge, 1990; Sverdrup & De Vries, 1994) which has simple input
283 parameter requirements and assumes the ecosystem is at long-term equilibrium. The SMB model defines
284 the critical load as a line connecting three points in (S_{dep}, N_{dep}) space, $CL_{max}S$ (the maximum sulphur
285 critical load), $CL_{max}N$ (the maximum nitrogen critical load) and the $CL_{min}N$ (the minimum nitrogen critical
286 load). The regions above the (S_{dep}, N_{dep}) line connecting the points $(CL_{max}S, 0)$, $(CL_{max}S, CL_{min}N)$ and
287 $(0, CL_{max}N)$ are said to be in exceedance of the critical load (see Figure 1). $CL_{max}S$ is determined by
288 alkaline inputs to the ecosystem such as base cation deposition (BC_{dep}) and base cation weathering (BC_w)
289 minus acidic inputs (chloride deposition, Cl_{dep}), losses through (non-sodium) base cation uptake through
290 harvesting or grazing (BC_u) (Equation 1), and the critical leaching of the acid neutralizing capacity
291 ($ANC_{le,crit}$, Equation 2).

$$292 \quad CL_{max}S = BC_{dep} + BC_w - Cl_{dep} - BC_u - ANC_{le,crit} \quad (1)$$

$$293 \quad ANC_{le,crit} = -Q^{2/3} \cdot \left(1.5 \cdot \frac{BC_{dep} + BC_w - BC_u}{K_{gibb} \cdot (Bc/Al)_{crit}} \right) \quad (2)$$

294 The Acid Neutralizing Capacity refers to the soil's ability to neutralize input fluxes of acidifying ions
295 through the release of cations from the soil into the soil water. The addition of these neutralizing ions to
296 soil water is a process known as leaching. However, the removal of base cations from soil water may also
297 result in damage to plants via reductions in root growth, stem growth and crops, with the extent of
298 damage dependent on the plant species. The plant-species-specific critical base cation to aluminum soil
299 water ratio in equation (2), $(Bc/Al)_{crit}$, is linked to corresponding percent reductions of plant growth. If
300 a larger percent reduction is deemed acceptable, the value of $(Bc/Al)_{crit}$ will be smaller, the magnitude of
301 $ANC_{le,crit}$ will be larger, and the value of $CL_{max}S$ will be larger, and larger amounts of deposition will be
302 required to exceed the critical load. Conversely, if a smaller impact is deemed acceptable, the value of
303 $(Bc/Al)_{crit}$ will be larger, the magnitude of $ANC_{le,crit}$ will be smaller, the value of $CL_{max}S$ will be smaller,
304 and smaller amounts of deposition will be required to exceed the critical load. Examples of
305 $(Bc/Al)_{crit}$ values for different tree types and ground vegetation may be found in CLRTAP (2023),
306 Chapter V, Table V.8). The critical base cation to aluminum ratio, $(Bc/Al)_{crit}$ (multiplied by the gibbsite
307 equilibrium constant K_{gibb}) is thus the chemical criterion usually used to define the acceptable level of
308 potential damage to biota, specifically via the definition of $ANC_{le,crit}$, which includes the effect of soil
309 runoff (Q).

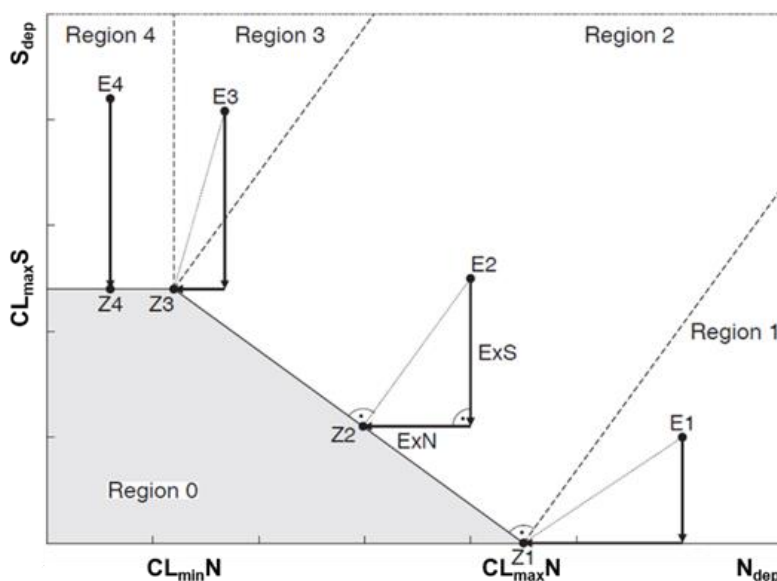


310 The $CL_{min}N$ represents the long-term removal of N from the ecosystem as defined by nitrogen
 311 immobilization (N_i) and uptake (N_u) (Equation 3). The $CL_{max}N$ value is determined using $CL_{min}N$ and
 312 $CL_{max}S$, which is divided by unity minus the denitrification fraction (f_{de}) (Equation 4). Deposition points
 313 of S_{dep} and N_{dep} which fall outside (above) the critical load exceedance line defined by $CL_{min}N$, $CL_{max}N$,
 314 and $CL_{max}S$ are considered to be in *exceedance of their critical loads* (see Figure 1, Regions 1 through 4).
 315 Note that these critical loads may be specific to a political jurisdiction, and hence caution should be
 316 applied when considering the critical loads and exceedance maps where there are cross-border
 317 discontinuities in data sources, parameterization and methodology, and resolution.

318
$$CL_{min}N = N_i + N_u \quad (3)$$

319
$$CL_{max}N = CL_{min}N + \left(\frac{CL_{max}S}{(1-f_{de})} \right) \quad (4)$$

320 Figure 1 illustrates the manner in which critical loads with respect to acidity are calculated using the SMB
 321 methodology. Based on the sulphur and nitrogen deposition amounts (S_{dep} , N_{dep}), the Region in which
 322 exceedance is occurring is first defined. The amount of exceedance is defined as the shortest possible
 323 path (in eq of deposition) to the shaded “no-exceedance” Region 0 of Figure 1, bordered by the line
 324 described above. Deposition amounts which fall above the critical load function defined by Region 0 are
 325 considered to be in exceedance of their critical loads. The shape of the critical load function is defined by
 326 $CL_{max}S$, $CL_{min}N$ and $CL_{max}N$, which in turn are functions of the ecosystems and at-risk species under
 327 consideration.



328
 329 Figure 1. SMB Critical Load Function for acidification, showing exceedance regions 1 through 4 and “below exceedance” region
 330 0. Deposition in exceedance of critical loads correspond to regions 1 through 4, while the grey region encompasses deposition
 331 below critical loads. The change in sulphur and nitrogen deposition required to bring a given ecosystem in exceedance to below
 332 exceedance is described by ExS, ExN, and the amount in exceedance is the dotted line linking E_i to Z_i . After CLRTAP, 2023,
 333 Figure 7.3

334



335 Table 1: Data sources, model types and major parameters for North American forest soil critical loads maps. A database of maps
 336 within the U.S.A was provided in National Atmospheric Deposition Program (NADP, 2022). Table adapted from Lynch *et al.*
 337 (2022).

Source	Model	Resolution	Extent	Chemical criteria	BC _w approach	Uptake
(McNulty <i>et al.</i> , 2007, 2013)	SMB	1 km ²	U.S.A-wide	Bc/Al, Coniferous forest: 1, deciduous forest: 10	Clay correlation - substrate method	B _{cu} , N _u
(Duarte <i>et al.</i> , 2011, 2013)	SMB	5 km ²	New England	Bc/Al = 10	Clay correlation - substrate method	B _{cu} , N _u
(Phelan <i>et al.</i> , 2014; data corrected 2016)	SMB	1 m ²	Pennsylvania	Bc/Al = 10	PROFILE	B _{cu} , N _u
(Sullivan, 2011; Sullivan <i>et al.</i> , 2012)	MAGIC	Watershed	Virginia and New York	Bc/Al, Ca/Al = 1 and 10, Bsat = 5 and 10	MAGIC	B _{cu}
Cathcart <i>et al.</i> (in prep.)	SMB	250 m x 250 m	Canada-wide	Bc/Al = site specific	Soil texture approximation	B _{cu} , N _u

338

339 1.2 North American Aquatic Ecosystems Acidity Critical Loads

340 The North American Aquatic Ecosystem acidity critical load dataset constructed here combined
 341 individual datasets from the Canada and the USA.

342 1.2.1 Canadian Aquatic Ecosystem Data

343 Environment and Climate Change Canada data corresponding to the subset of 2,997 lake surveys which
 344 reside within the common AQMEII4 North American grid were used in conjunction with the Steady-State
 345 Water Chemistry (SSWC) critical load model (Sverdrup *et al.*, 1990) as described in Aherne and Jeffries
 346 (2015). The SSWC model has been widely used in regional lake critical load assessments across Europe
 347 (e.g. Posch *et al.*, 2001), Canada (e.g. Cathcart *et al.*, 2016; Henriksen *et al.*, 2002; Jeffries *et al.*, 2010;
 348 Scott *et al.*, 2010; Whitfield *et al.*, 2006; Williston *et al.*, 2016), and the United States (e.g. Dupont *et al.*,
 349 2005; Miller, 2011). Briefly, the critical load exceedance is defined as the difference between the total
 350 sulphur deposition S_{dep} and the acidity critical load value CL(A). The latter is determined from the non-
 351 marine, pre-acidification base cation flux ([BC*]₀) minus the Acid Neutralizing Capacity limit
 352 (ANC_{limit}) for protecting aquatic biota from damage, scaled by the catchment runoff (Q):

$$353 \quad CL(A) = Q([BC^*]_0 - ANC_{limit}) \quad (5)$$

354 Where available, a site-specific modelled isotope mass balance estimate of Q (Gibson *et al.*, 2010) was
 355 used (n=684) in preference to a Q value derived from a GIS-modelled map approach using regional
 356 datasets (Reinds *et al.*, 2015). When Dissolved Organic Carbon (DOC, mgC L⁻¹) values were available
 357 (n=2,875) the organic acid adjusted ANC_{limit} ([ANC]_{oaa}) was used to include the influence of organic acids
 358 in the lake as 1/3 the charge density (m, here set to 10.2 µeq mgC⁻¹) (Lydersen *et al.*, 2004; Hruska *et al.*,
 359 2001),

$$360 \quad [ANC]_{oaa} = [ANC]_{limit} - \frac{m}{3} DOC \quad (6)$$

361 Where the lake acid neutralizing capacity [ANC]_{limit} is defined as the excess equivalents of cations –
 362 anions in lakewater:

$$363 \quad [ANC]_{limit} = BC_{le} + NH_{4le} - SO_{4le} - NO_{3le} - Cl_{le} \quad (7)$$



364 BC_{le} , NH_{4le} , SO_{4le} , NO_{3le} , Cl_{le} are the charge equivalents ($\mu\text{eq L}^{-1}$) of ionic base cations, ammonium,
365 sulphate, nitrate, and chloride in lakewater.

366 For lakes lacking DOC samples, an ANC_{limit} of $40 \mu\text{eq L}^{-1}$ was chosen as a conservative value, previously
367 used in regional Canadian assessments (e.g. Henriksen *et al.*, 2002), and based on the response of brown
368 trout (Lien *et al.*, 1996). Since the SSWC model does not consider non-acidifying nitrogen, only sulphur
369 was used to determine exceedance (i.e. exceedance is defined as the total S deposition minus the critical
370 load of Equation (5)).

371 1.2.2 USA Aquatic Ecosystem Data

372 Aquatic critical loads for the USA were taken from the National Critical Loads Database Version 3.2.1
373 (NCLDV3.2.1, Lynch *et al.*, 2022), which contains both the critical load data used here and supporting
374 information. A total of 21,667 critical loads were used for 14,334 unique lakes and streams across the
375 USA (a combination of different methods for determining the critical loads were included in the USA
376 values, sometimes resulting in more than one CL estimate for the same water body). Most critical loads
377 (78%) were determined using the SSWC model as described above and by equations 5 and 7 (Lynch *et al.*
378 *et al.*, 2022; Scheffe *et al.*, 2014; Dupont *et al.*, 2005, Miller 2011, VDEC (2003, 2004, 2012)). Site-specific
379 catchment Q estimates for these values were based on 30-year Normals that are included as a catchment
380 parameter in the National Hydrography Dataset Plus (NHD+2, US EPA, 2023). The other 22% of critical
381 loads were determined by a dynamic modelling approach (e.g., MAGIC and PnET-BGC models)
382 (Sullivan *et al.*, 2005; Fakhraei *et al.*, 2014; Lawrence *et al.*, 2015) and a combination of dynamic
383 modeling with a regionalization approach (e.g. hurdle/regional regression modeling) to determine the
384 critical load across the landscape (McDonnell *et al.*, 2012, 2014; Sullivan *et al.*, 2012; and McDonnell *et al.*
385 *et al.*, 2021). Site-specific catchment Q estimates were also used; these were based on the specific research
386 project. An ANC_{limit} of $50 \mu\text{eq L}^{-1}$ was used for the Eastern USA, with the exception of streams in the
387 Adirondacks Mountain, NY, which used $20 \mu\text{eq L}^{-1}$ (McDonnell *et al.* 2021) and $20 \mu\text{eq L}^{-1}$ for the
388 western USA. Organic acid-adjusted ANC_{limit} values were not used in generating the USA CL(A) datasets.
389 In many cases, multiple studies estimated CL(A) for the same lake or stream, leading to multiple CL(A)
390 estimates for a single water body. An average critical load value was therefore used for these waterbodies
391 with more than one critical load. A more detailed description of the USA aquatic critical loads used here
392 can be found in Lynch *et al.*, (2022).

393 1.3 USA Sensitive Epiphytic Lichen

394 Critical loads for sensitive epiphytic lichen species richness made use of 9,000 community
395 surveys across the USA from 1990-2012 (Geiser *et al.* 2019), where a 90% quantile regression was used
396 to model relationships between deposition levels and observed species richness in order to estimate
397 critical loads. Here, Geiser *et al.* (2019) sets a -20% decline in species richness (their “Low ecological
398 risk” critical load) as the level of ecosystem damage that can occur before the loss of species impacts the
399 presence of plentiful forage, nesting materials or insect habitat; hence determining the critical load. The
400 models show that there is a consistent relative response of lichen communities across climates, which
401 results in a single critical load of $3.1 \text{ kg-N ha}^{-1} \text{ yr}^{-1}$ for sensitive epiphytic lichen, which can be applied
402 across all ecosystems in which the lichen can be found. This value was applied to all broadleaf, conifer,
403 or mixed forest landcover types as designated by the National Land Cover Database (NLCD, Dewitz
404 2021). The original 30m resolution NLCD dataset was aggregated to a 240m resolution grid including all
405 cells with greater than 10% forest cover. Exceedances of the above critical load were calculated for each
406 240m resolution cell based on the annual deposition of the overlapping 0.125° resolution AQMEI4 CTM
407 model cell.



408 1.4 USA Herbaceous Plants

409 The USA herbaceous plants dataset uses the critical load of total nitrogen for a decline in
410 herbaceous species community richness, developed using over 14,000 vegetation survey plots across
411 nitrogen deposition gradients (Simkin *et al.*, 2016). An observation-based approach using median
412 quantile regressions for herbaceous species richness response to deposition was employed, to generate
413 critical loads with respect to nitrogen deposition linked to various atmospheric and soil conditions. A
414 model was developed for open canopy ecosystems where the critical load varies with observed soil pH,
415 precipitation, and mean temperature. A second model was developed for closed canopy ecosystems
416 where the critical load varies with observed soil pH alone. The pant level critical loads were mapped
417 across the continental U.S. using land cover from the NLCD. Open canopy systems were defined as the
418 combination of the NLCD grassland and shrubland landcover types, while closed canopy ecosystems
419 were defined as the combination of the NLCD's broadleaf, conifer, or mixed forest landcover classes.
420 The resulting critical loads were aggregated to a 240m grid including all cells with greater than 10%
421 cover. Using the United States Department of Agriculture gridded National Soil Survey Geographic
422 Database (gNATSGO) soil pH dataset (<https://www.nrcs.usda.gov/resources/data-and-reports/gridded-national-soil-survey-geographic-database-gnatsgo>,
423 last access July 12, 2024), and PRISM temperature and precipitation models (Daly *et al.*, 2008), the CL of N for open canopy systems ranged from 6.2 to
424 12.3 kg-N ha⁻¹yr⁻¹ and the CLs of N for closed canopy systems ranged from 6.1 to 23.7 kg-N ha⁻¹yr⁻¹. The
425 two datasets were then merged into a single CL raster using the minimum CL when cells overlapped.
426 Exceedances of the resulting critical loads for nitrogen deposition were then generated using the annual
427 deposition of the overlapping 0.125° resolution AQMEII4 CTM model cell.
428

429 1.5 EU: Acidification of Terrestrial Ecosystems

430 The critical load database and the exceedance calculation for Europe were provided by the Coordination
431 Centre for Effects (CCE) under the United Nations Economic Commission for Europe Convention on
432 Long-range Transboundary Air Pollution (UNECE LRTAP Convention), hosted by the Umweltbundesamt
433 (UBA) in Germany, which develops and maintains the European critical loads database (Geupel *et al.*,
434 2022). The most recent database available was used here and was also used within the review process of
435 the Gothenburg protocol. It typically contains critical load values for acidification and eutrophication, and
436 has two different components. The first component is data delivered by the member countries of the
437 International Cooperative Programme on Modelling and Mapping. This data is collected within an
438 officiated “Call for Data” (CfD) process within the framework of the Working Group on Effects (WGE).
439 The most recent CfD was finalized in the year 2021. The methods used to determine acidification loads
440 are country-dependent, but all make use of the Simple Mass Balance as described above (Sverdrup & De
441 Vries, 1994; CLRTAP, 2023). The country-specific detailed methods and participating countries may be
442 found in Geupel *et al.* (2022). If countries do not deliver their own CL data, the CCE fills these data gaps
443 with its own background database (Reinds *et al.*, 2021).

444 The decision of the chemical criterion used to define exceedance (e.g., critical aluminium concentration,
445 critical pH, and critical base saturation) and the chosen critical limit value is usually country-specific.
446 The background CCE database makes use of a fixed value based on a critical pH value of 4.2.

447 1.6 EU: Eutrophication of Terrestrial Ecosystems

448 Critical loads for EU eutrophication (CL_{nutN}) are also based on the SMB method applied to nitrogen
449 deposition – (Equation 8). Generally, the methods to derive the parameters of this equation are similar for
450 national datasets and the CCE dataset (e.g. the estimation of the nitrogen uptake (N_u) is linked to growth
451 potential of the vegetation, the fraction of the nitrogen which is denitrified (f_{de}) is connected to the soil



452 type). One major difference occurs when it comes to the derivation of the accepted nitrogen leaching
453 ($N_{le(acc)}$) term. There are two ways to estimate the $N_{le(acc)}$. One way is to simply assign how much nitrogen
454 is allowed to leave the ecosystem based on observations. Another way is to calculate the $N_{le(acc)}$ by using
455 the amount of soil runoff (Q) and multiply it with a critical limit for nitrogen concentration. The latter
456 limits can be linked to negative effects for the related ecosystems (such as fine root damage). The choice
457 of the values for the critical limit for nitrogen is one of the main sources for differences in the modelled
458 EC SMB eutrophication CL (see also CLRTAP, 2023). Another main source for differences in the CL
459 values between countries is the integration of so-called empirical critical loads. These empirical values
460 can be used as upper and lower boundaries for the SMB modelling results in order to avoid rather extreme
461 results in ecosystems where the SMB model predicts very high or very low eutrophication CL values.
462 Empirical CL were updated recently and are well documented in Bobbink *et al.* (2022).

$$463 \quad CL_{nut}N = N_i + N_u + \left(\frac{N_{le(acc)}}{1-f_{de}} \right) \quad (8)$$

464 The CL exceedance was calculated for every available critical load value in the integrated CL database of
465 the CCE (about 4 million EU data points) and later aggregated on the basis of the AQMEII4 deposition
466 grid cells. The resulting EU CLE are summarized as the share of the receptor area with critical load
467 exceedance (bar charts) and the magnitude of the exceedance within each analysis grid cell (maps). The
468 exceedance in a grid cell is defined as the so-called 'average accumulated exceedance' (AAE), which is
469 calculated as the area-weighted average of the exceedances of the critical loads of all ecosystems in this
470 grid cell. The units for critical loads and their exceedances are equivalents per hectare and year, making S
471 and N deposition comparable on their impacts, which is important for acidity CLs.

472 2.0 AQMEII4 Overview Description

473 The setup of the AQMEII4 regional model comparison is described in detail in Galmarini *et al.* (2021); a
474 brief overview is provided here. The models within this analysis are a "snapshot" of regional chemical
475 transport model development as of the time simulations were completed (2021).

476 Model simulations were carried out for the years 2009 and 2010 for the European region, and 2010 and
477 2016 for North America. North American years were chosen due to policy relevance, with a significant
478 change in SO₂ emissions controls enacted between the two years. European years were chosen due to a
479 large difference in meteorology between 2009 and 2010, hence allowing the effects of potential
480 meteorological on deposition to be estimated. Simulations were carried out by making use of the
481 individual models' grid projection and resolution. Mass-conserving interpolation (for concentrations and
482 fluxes) and nearest neighbour interpolation (for diagnostics) were then used to map these "native grid"
483 outputs to corresponding North American and European AQMEII4 grids. The latter have 0.125° x 0.125°
484 resolution (North America: 23.5° N to 58.5° N, 130° W to 59.5° W; Europe 25° N to 70° N, 30° W to 60
485 ° E). Values extracted from the AQMEII4 grid locations were used for comparison to observations.
486 Models made use of their own meteorological drivers or on-line meteorological components for
487 meteorological field predictions. Models shared common inputs for emissions and chemical lateral
488 boundary conditions. The latter provide a uniform chemical forcing and prevent input variations not
489 associated with the models themselves from influencing simulations results.

490 North American anthropogenic emissions were generated using emissions modelling platforms which
491 included the anthropogenic inventories, temporal and spatial allocation from county or state/province
492 level to native model grids, for each of the two model years, as well as adjustments for specific
493 inventories by year. Emissions processing was carried out by the United States Environmental Protection
494 Agency for the Carbon Bond 6 (revision 3; CB6r3)) and Statewide Air Pollution Research Center -07



495 (SAPRC07) chemical mechanisms (Yarwood *et al.*, 2010; Carter, 2010), and by Environment and Climate
496 Change Canada for the Acid Deposition and Oxidant Mechanism version II (ADOM-II; Stockwell *et al.*,
497 1989). Note that while none of the modelling groups made use of the SAPRC07 mechanism itself within
498 their simulations, this mechanism was sometimes used as a starting point for lumping individual models'
499 VOC species, due to the greater level of detail available within the SAPRC07 speciation. European
500 anthropogenic emissions were prepared for the participating models' chemical mechanisms by the
501 Netherlands Organization for Applied Scientific Research (TNO) as part of the Monitoring Atmospheric
502 Composition and Climate, part 3 (MACC-III) project (Kuenen *et al.*, 2015), with individual groups using
503 their own emissions data for the portion of their native model grids extending beyond the range of
504 MACC-III emissions grid if necessary.

505 North American forest fire emissions were generated by combining the US emissions modelling platform
506 values with Canadian data for 2010, while both USA and Canadian data were based on the 2016
507 emissions modelling platform estimates. These forest fire emissions included criteria air contaminant
508 emission mass, heat flux, and acres burned. Fire plume rise calculations were carried out by individual
509 modeling groups, typically based on large stack plume rise formulae (Briggs, 1971, 1972). European
510 forest fire emissions were provided by the Finnish Meteorological Institute using eight layers from 50 to
511 6200m. Both North American and European forest fire emissions were chemically disaggregated by the
512 participating modelling groups and mapped on a nearest grid cell basis to their native model grids.

513 Lightning NO emissions were also prescribed in both domains, based on GEIA monthly climatology
514 values (Price *et al.*, 1997), diurnally disaggregated following Blakeslee *et al.* (2014) and allocated
515 vertically following Ott *et al.* (2010) by individual modelling groups.

516 Chemical lateral boundary conditions for both EU and NA simulations were taken from 3 hourly, 0.75° x
517 0.75°, 54 vertical level ECMWF CAMS EAC4 reanalysis products (Inness *et al.*, 2019), interpolated by
518 participants to their own vertical and horizontal grid structures, and chemically disaggregated to their own
519 chemical speciation.

520 2.1 Common Model Diagnostics

521 The AQMEII4 protocol for ensemble participants included the reporting of gas-phase species'
522 aerodynamic, bulk surface, stomatal, mesophyll, quasi-laminar sub-layer and within-canopy buoyant
523 resistances (when present in the reporting model). Effective conductances (Paulot *et al.*, 2018; Clifton *et al.*,
524 2020) and effective fluxes (Galmarini *et al.*, 2021) were also reported. These latter two diagnostic
525 terms provide the relative contribution of the four main pathways associated with gas-phase deposition
526 towards the deposition velocity and the deposition flux, respectively. The four main pathways include
527 soil, the lower canopy, leaf cuticles, and stomata. Note that not all models specify a separate lower
528 canopy pathway (the conductance associated with this pathway tends to be relatively small, providing
529 justification for its absence). Effective fluxes are of particular interest to criticalload exceedance analysis,
530 since they provide information on the charge equivalents deposited to different component surface types.
531 Effective fluxes include the impact of other processes in addition to deposition on the concentrations and
532 hence on the net flux of the deposited gases, via the net flux term (F). For example, the soil, lower
533 canopy, cuticle and stomatal effective fluxes in the Wesely (1989) dry deposition parameterization are
534 given by:

$$535 \quad DFLX_{SOIL} = \left(\frac{(r_{ac} + r_{gs})^{-1}}{(r_s + r_m)^{-1} + (r_{lu})^{-1} + (r_{dc} + r_{cl})^{-1} + (r_{ac} + r_{gs})^{-1}} \right) F \quad (9)$$



$$536 \quad DFLX_{LCAN} = \left(\frac{(r_{dc}+r_{cl})^{-1}}{(r_s+r_m)^{-1}+(r_{lu})^{-1}+(r_{dc}+r_{cl})^{-1}+(r_{ac}+r_{gs})^{-1}} \right) F \quad (10)$$

$$537 \quad DFLX_{CUT} = \left(\frac{(r_{lu})^{-1}}{(r_s+r_m)^{-1}+(r_{lu})^{-1}+(r_{dc}+r_{cl})^{-1}+(r_{ac}+r_{gs})^{-1}} \right) F \quad (11)$$

$$538 \quad DFLX_{stom} = \left(\frac{(r_s+r_m)^{-1}}{(r_s+r_m)^{-1}+(r_{lu})^{-1}+(r_{dc}+r_{cl})^{-1}+(r_{ac}+r_{gs})^{-1}} \right) F \quad (12)$$

539 Where F is the net flux to the surface, and the r terms are resistances associated with different pathways
 540 of gas mass transfer to the four surface components (r_{ac} : aerodynamic mass transfer within canopy,
 541 dependent on canopy height and density, r_{gs} : the soil and leaf litter resistance, r_{dc} : canopy buoyant
 542 convection resistance, r_{cl} : resistance associated with leaves, twigs, bark and other exposed surface in the
 543 lower canopy, r_{lu} : resistance of leaf cuticles in healthy vegetation and other outer surfaces, r_s : leaf
 544 stomata, r_m : leaf mesophyll). The effective conductances can be generated from similar formulae, with
 545 the F term in equations (9) through (12) being replaced by the deposition velocity of the gas V_d . Note that
 546 the formulae for individual models vary from the Wesely (1984) example shown above; see Galmarini *et*
 547 *al.* (2021) for details on the formulae for each of the gas-phase deposition algorithms used in the
 548 AQMEII4 regional model ensembles analyzed here.

549 2.2 Model Parameterization Descriptions

550 2.2.1 CMAQ-M3Dry, CMAQ-STAGE, CMAQ (Hertfordshire) – WRF-CMAQ Implementations

551 These three models make use of the WRF-CMAQ off-line modelling framework (CMAQ v5.3.2, US EPA
 552 (2020)), with the North American implementations (CMAQ-M3Dry, CMAQ-STAGE) employing 12 km
 553 cell resolution, and the EU implementation employing 10km cell resolution (Lambert Conformal Conic
 554 projection, 459x299 and 500x681 grid cells, respectively). The CMAQ implementations employed 35
 555 model layers with the lowest layer thickness of ~20m. Both NA models operate in an off-line
 556 configuration using the same driving weather forecast model output (NA: WRF4.1.1, EU: WRF 4.2.1,
 557 Skamarock *et al.*, 2019). All three CMAQ model implementations use the same gas-phase chemical
 558 mechanism (Carbon Bond 6; Luecken *et al.*, 2018)), a modal aerosol size distribution representation with
 559 three modes (Binkowski and Roselle, 2003), aerosol microphysics through the AERO7 module (Appel *et*
 560 *al.*, 2021; Binkowski and Shankar, 1995; Vehkamäki *et al.*, 2002), and thermodynamic equilibrium
 561 partitioning for semivolatile inorganic species between gas and aerosol phases species (involving the
 562 components K^+ - Ca^{2+} - Mg^{2+} - NH_4^+ - Na^+ - SO_4^{2-} - NO_3^- - Cl^- - H_2O) using the ISORROPIA II algorithm
 563 (Fountoukis and Nenes, 2007). Organic aerosol formation and monoterpene oxidation are modelled as
 564 described in AERO7 (Appel *et al.*, 2021, Xu *et al.*, 2018).

565 For all three model implementations, the impact scavenging of aerosols by cloud droplets is carried out
 566 for the Aitken mode particles, while accumulation and coarse mode particles may form cloud
 567 condensation nuclei, resulting in their scavenging via cloud droplet nucleation (Binkowski and Roselle,
 568 2003; Chaumerliac, 1984, Fahey *et al.*, 2017). Aerosol scavenging in the Aitken mode is carried out as a
 569 simple exponential decay for number, surface area and mass concentration assuming a cloud droplet
 570 settling velocity based on Pruppacher and Klett (1978), and an assumed cloud droplet size distribution.
 571 Only Aitken mode particles (roughly 0.01 to 0.1 μm diameter) are impact scavenged, for which only
 572 cloud liquid water is included as a scavenging hydrometeor. Wet deposition of all aqueous species is
 573 represented as a first-order loss rate based on the precipitation rate and total liquid water content (Fahey *et*



574 al., 2017). The number of cloud droplets is parameterized following Bower and Choularton (1992) from
575 the cloud liquid water content provided by the meteorological model.

576 The three CMAQ implementations differ in the algorithms employed for aerosol and gas-phase dry
577 deposition algorithms.

578 CMAQ-M3Dry's aerosol dry deposition methodology was based on Binkowski and Shankar (1995), with
579 updates as described in Venkatram and Pleim (1999), Giorgi (1986), and subsequent corrections to
580 include the effect of mode width in the Stokes number (reducing previous large overpredictions in coarse
581 mode deposition velocities). Further modifications included changes to the Stoke's number for vegetated
582 surfaces, modification of the impaction term, scaling of diffusion layer resistance by LAI for the
583 vegetated fraction of each grid cell, and improved mass conservation for the process of gravitational
584 settling (Appel *et al.*, 2021).

585 CMAQ-STAGE and CMAQ (Hertfordshire)'s aerosol dry deposition methodology followed that of
586 CMAQ-M3Dry, but made use of Slinn (1982) and Zhang *et al.* (2001) for impaction on vegetated
587 surfaces, and Giorgi (1986) for water and soil surfaces, with the resulting deposition velocities for
588 smooth and vegetated surfaces weighted by the area of vegetated surface (Appel *et al.*, 2021).

589 The gas-phase dry deposition algorithms and diagnostic equations of CMAQ-M3Dry, CMAQ-STAGE
590 and CMAQ (Hertfordshire) are described in detail elsewhere (Galmarini *et al.*, 2021, Table B2, with other
591 implementation details in Hogrefe *et al.*, 2023). The algorithms follow the original approach of Wesely *et al.*
592 (1989), but with separate resistance branches for the vegetated and non-vegetated fractions, dry versus
593 wet fractions, and snow-covered versus non-snow covered fractions.

594 Bidirectional fluxes of ammonia were found in the analysis which follows to be a major source of model-
595 to-model variability, hence will be described here in more detail.

596 CMAQ-M3Dry simulated bidirectional fluxes of ammonia by first calculating soil ammonia
597 concentrations using the Environmental Policy Integrated Climate (EPIC) agricultural ecosystem model
598 (Williams, 1995; Ran *et al.*, 2018), prior to the CTM simulations being carried out. Typically, the EPIC
599 model simulation requires a model spin-up period of 25 years or more, and requires a prior simulation of
600 N deposition as input information. The soil NH₃ concentrations from this coupled system were then
601 used as inputs for the AQMEII4 run (Pleim *et al.*, 2019). While all dry deposition diagnostics reported to
602 AQMEII4 for CMAQ-M3Dry were computed making use of a post-processor, the post-processing did not
603 include the generation of bidirectional flux calculations, and hence diagnostics such as the net
604 compensation point concentration and the ground compensation point calculation were not provided from
605 CMAQ-M3Dry for AQMEII4.

606 CMAQ-STAGE (Massad *et al.*, 2010; Bash *et al.*, 2013) also simulated bidirectional fluxes following
607 Williams, (1995), using a previous coupled EPIC simulation only for initial conditions, porting
608 methodology and information on daily fertilization and nitrification from EPIC into the CMAQ-STAGE
609 framework while estimating evasion and deposition locally within the chemical transport model. This
610 methodology, which operates on a land-use specific basis and then aggregates to a grid-cell basis, allowed
611 additional AQMEII4 diagnostic to be incorporated into the CMAQ-STAGE simulations. This allows a
612 greater consistency between the CTM and the resulting soil NH₃ calculations (and allows for the output of
613 all of the diagnostics as specified under the AQMEII4 protocol see Hogrefe *et al.*, 2023). However, these
614 calculations do not include other terms in EPIC dealing with N fixation, mineralization, denitrification,
615 runoff, percolation and plant uptake, and hence will diverge from the EPIC simulated soil ammonia



616 concentrations due to the differences in evasion and deposition parameterizations between CMAQ-
617 STAGE and EPIC.

618 2.2.2 NA WRF-Chem (IASS)/ EU WRF-Chem (IASS), NA WRF-Chem (UPM)/EU WRF-Chem (UPM) ,
619 NA WRF-Chem (UCAR): WRF-Chem implementations

620 All three of these models made use of the WRF-Chem chemical transport modelling framework (Grell *et*
621 *al.*, 2005), employing a 12km Lambert Conformal Conic projection (400x360 grid cells in the European
622 domain, 480x290 grid cells in the North American domain), 2-way coupling between air-quality and
623 meteorology, a sectional aerosol size distribution representation (4 bins), aerosol microphysics and
624 chemistry via the MOSAIC model (Zaveri *et al.*, 2008), organic aerosol formation following Knote *et al.*,
625 (2014, 2015), cloud microphysics following Morrison *et al.* (2009), the Noah land surface model (Noah-
626 MP, Niu *et al.*, 2011), the Rapid Radiative Transfer Model for radiative transfer calculations (RRTM,
627 Iacono *et al.*, 2008), biogenic emissions using the MEGAN model (Guenther *et al.*, 2006, Wiedenmyer *et*
628 *al.*, 2007), and the FAST-J algorithm for photolysis rate calculation (Fast *et al.*, 2009). All three code
629 versions also make use of the Wesely (1989) parameterization for gas dry deposition and the Binkowski
630 and Shankar (1995) approach for aerosol deposition. However, WRF-Chem has a large variety of
631 configurations available for other model processes, allowing the impact of those configurations on
632 deposition results to be studied under AQMEII4. The differences between the model configurations are
633 summarized in Table 2. It should also be noted that WRF-Chem is an on-line modelling framework –
634 differences in the model parameterizations can influence the meteorological predictions through the
635 aerosol direct and indirect effects, and consequently the meteorology generated by the implementations
636 may also differ.

637 Not all of the WRF-Chem model implementations were able to report all of the information required to
638 calculate exceedances: the WRF-Chem (IASS) implementation did not report all of the species
639 contributing to S_{dep} and N_{dep} totals, and also did not report several diagnostics requested under the
640 AQMEII4 protocol. Consequently, the WRF-Chem (IASS) results were not included in ensemble
641 deposition generation and the model ensembles are referred to hereafter as “reduced ensembles”. Our
642 analysis is therefore based on these reduced ensembles, though WRF-Chem (IASS) values for deposition
643 totals have been provided when available in Figures and Tables for comparison purposes.

644



645 Table 2. AQMEII4 WRF-Chem Configuration Differences

Parameterization	WRF-Chem (IASS)	WRF-Chem (UPM)	WRF-Chem (UCAR)
WRF-Chem version number	3.9.1	4.0.3	4.1.2
Wet Deposition	Convective : via Grell and Devenyi (2002); grid-scale following Neu and Prather (2012) for gases, Chapman <i>et al.</i> (2009) for aerosols	Grid scale wet deposition following Easter <i>et al.</i> (2004).	Below cloud: Slinn (1984); in-cloud: Easter <i>et al.</i> (2004)
Land Use/Land Cover Classification	Europe: CORINE 33 classes. North America: USGS-24 (Anderson <i>et al.</i> , 1976), 24 classes	USGS-24 classes, (Anderson <i>et al.</i> , 1976), 24 classes	Modified IGBP MODIS NOAH, 21 classes including oceans and inland water, Friedl <i>et al.</i> (2010);
Cumulus cloud parameterization	Grell and Devenyi, 2002.	Grell and Devenyi, 2002	Grell and Freitas, 2014
Windblown Dust	On-line, Shao- <i>et al.</i> 2011	MOSAIC (Zaveri <i>et al.</i> , 2008)	GOCART, with AFWA modifications Gong <i>et al.</i> (1997), Ginoux <i>et al.</i> (2001).
Gas-Phase Chemistry Mechanism	MOZART, Emmons <i>et al.</i> (2010)	CMBZ, Zaveri and Peters, 1999	MOZART, Emmons <i>et al.</i> (2010)
Vertical resolution	38 levels up to 50 hPa	35 vertical levels	41 vertical levels
PBL Scheme	Mellor–Yamada–Janjic, Janic (2001)	Yonsei University (YSU) Hong <i>et al.</i> (2006), Hong (2010)	Mellor–Yamada Nakahasi Niino, level 2.5 Nakanishi and Niino (2006)

646

647 2.2.3 LOTOS-EUROS (TNO): LOTOS-EUROS

648 LOTOS-EUROS (TNO) used in the AQMEII4 EU simulations is an open-source 3D chemistry transport
 649 model used extensively for air-quality forecasts and scenarios for European domains (Timmermans *et al.*,
 650 2022; Manders *et al.*, 2017). Gas dry deposition fluxes made use of the Wesely (1989)-based approach
 651 (DEPosition of Acidifying Compounds; DEPAC, Van Zanten *et al.*, 2010). Particle dry deposition was
 652 carried out using the approach of Zhang (2001). Wet deposition followed the droplet saturation approach,
 653 and cloud chemistry with sulphate formation dependent on cloud liquid water and droplet pH (Banzhaf *et al.*,
 654 2012). The dry deposition of ammonia makes use of a bidirectional flux approach (Wichink Kruit *et al.*,
 655 2012). Gas-phase chemistry was carried out using a modified form of the CBM-IV scheme (Gery *et al.*
 656 *et al.*, 1989; Whitten *et al.*, 1980). N₂O₅ hydrolysis was included following Schaap *et al.* (2004), and
 657 inorganic thermodynamic particle chemistry was solved using the ISORROPIA II module (Fountoukis
 658 and Nenes, 2007). The model operated using 12 layers in the vertical in a hybrid coordinate system, with
 659 the near surface layer having a thickness of ~20m and a model top of approximately 8 km. The
 660 simulations carried out here made use of a 20x20km grid cell size over Europe. Driving meteorology for
 661 the model was from 3-hourly ECMWF short-term forecasts. Land use data for the model comes from the
 662 Corine2000 Land Cover database (EEA, 2000, 2007).



663 2.2.4 GEM-MACH (Base), GEM-MACH (Zhang), GEM-MACH (Ops): GEM-MACH

664 All three of these NA models are variations on the Environment and Climate Change Canada GEM-
665 MACH model. The first two configurations (GEM-MACH (Base), GEM-MACH (Zhang)) are based on
666 the “research” version of the model, which has more detailed physical parameterizations, whereas GEM-
667 MACH (Ops) is based on the “operational forecast” configuration, where more simplified
668 parameterizations have been employed in order to reduce processing time for operational air-quality
669 forecast simulations. Common elements across all three implementations include a horizontal grid cell
670 size of 0.09° in a rotated latitude-longitude domain (~10km), 83 model levels, biogenic VOCs from
671 BEIS3.09, 3.1.3 (Vukovich and Pierce, 2002; Stroud *et al.*, 2010), a sectional aerosol size distribution (12
672 bins, Gong *et al.* (2003), the ADOM-II gas-phase mechanism (Stockwell *et al.*, 1989), a modified Odum
673 approach for SOA formation (Stroud *et al.*, 2018), and an inorganic aerosol chemistry module solving the
674 thermodynamic equilibrium for the SO_4^{2-} - NO_3^- - NH_4^+ - H_2O system (Makar *et al.*, 2003). The GEM-
675 MACH implementations also all make use of the GEM weather forecast model v4.9.8 for driving
676 meteorology (Côté *et al.*, 1998, Girard *et al.*, 2014)), with the ISBA land surface scheme (Belair *et al.*,
677 2003a,b), and the CCMA Rad2 radiative transfer algorithm (Li and Barker, 2005). As was the case for the
678 WRF-Chem implementations described above, GEM-MACH has several optional process representations
679 used in operational forecast versus research versions of the model, hence the relative importance of model
680 configurations versus deposition parameterizations may be studied. The differences between the
681 configurations are summarized in Table 3. Key differences between the models include:

- 682 (1) Similar to CMAQ-M3Dry and CMAQ-STAGE above, the only difference between GEM-MACH
683 (Base) and GEM-MACH (Zhang) is the gas-phase dry deposition scheme employed (GEM-MACH
684 (Base): Makar *et al.*, 2018; GEM-MACH (Zhang): Zhang *et al.*, 2003), though both models employ
685 the Zhang *et al.* (2010) parameterization for ammonia bi-directional fluxes;
- 686 (2) GEM-MACH (Base) and GEM-MACH (Zhang) make use of the Emerson *et al.* (2020) dry deposition
687 velocity correction to the approach of Zhang *et al.*, 2001) as well as semi-Lagrangian advection rather
688 than a diffusion equation lower flux boundary condition for particle settling and deposition;
- 689 (3) GEM-MACH (Base) and GEM-MACH (Zhang) employ aerosol direct and indirect effect feedbacks
690 between meteorology and chemistry, while GEM-MACH (Ops) does not. This requires the use of an
691 explicit hydrometeor scheme in the former two model configurations and resulting in different
692 meteorology between GEM-MACH (Base), GEM-MACH (Zhang) and GEM-MACH (Ops);
- 693 (4) GEM-MACH (Base) and GEM-MACH (Ops) make use of 15 land use categories aggregated from the
694 26 land use categories employed in GEM-MACH (Ops);
- 695 (5) Leaf Area Index values and seasonality for deposition for GEM-MACH (Base) and GEM-MACH
696 (Zhang) are based on satellite retrieval data rather than the BEIS-based approach used in GEM-MACH
697 (Ops) - the latter uses fixed LAI values for 232 land-use types and area-weights them to determine
698 grid cell LAI;
- 699 (6) GEM-MACH (Base) and GEM-MACH (Zhang) make use of six additional physical parameterizations
700 not present in GEM-MACH (Ops) (see Table 3).

701 Differences between GEM-MACH (Base) and GEM-MACH (Zhang) thus provide an estimate of the
702 relative importance of the gas-phase deposition parameterization towards simulation results, while
703 comparisons between GEM-MACH (Base or Zhang) and GEM-MACH (Ops) show the relative impact of



704 the combination of ammonia bidirectional fluxes and the suite of more complex physical
 705 parameterizations used in the former model configurations compared to the operational framework.

706 Table 3. AQMEII4 GEM-MACH Configuration Differences

Parameterization	GEM-MACH (Base)	GEM-MACH (Zhang)	GEM-MACH (Ops)
Gas dry deposition	Makar <i>et al.</i> (2018)	Zhang <i>et al.</i> (2003)	Makar <i>et al.</i> (2018)
Ammonia bidirectional fluxes	Zhang <i>et al.</i> (2010)	As in GEM-MACH (Base)	None
Particulate matter dry deposition	1-D semi-Lagrangian mass transfer (Makar <i>et al.</i> , 2018), using Emerson <i>et al.</i> (2020) correction to Zhang <i>et al.</i> (2001) coefficients	As in GEM-MACH (Base)	Zhang <i>et al.</i> (2001), applied as flux lower boundary condition in the diffusion equation.
Vertical resolution	83 levels plus 3 additional levels for forest canopy processes (Makar <i>et al.</i> , 2017)	As in GEM-MACH (Base)	83 levels
Meteorological model cloud parameterization	P3 explicit hydrometeor scheme (Morrison and Milbrandt, 2015; Milbrandt and Morrison, 2016).	As in GEM-MACH (Base)	Convective: Kain-Fritsch convective parameterization (Kain and Fritsch, 1990, Kain, 2004). Stratiform: Sundqvist <i>et al.</i> (1989)
Land Use/Land Cover Classification	GEM-MACH 15 Land use scheme (Makar <i>et al.</i> , 2018), aggregated from Zhang <i>et al.</i> , (2002, 2003) 26 land use categories.	Zhang <i>et al.</i> (2002, 2003), 26 land-use categories	As in GEM-MACH (Base)
Leaf Area Index data source	Satellite-derived (Zhang <i>et al.</i> , 2020)	As in GEM-MACH (Base)	BEIS-based (Vukovich and Pierces, 2002)
Seasonality for emissions	Based on satellite LAI (Zhang <i>et al.</i> , 2020)	As in GEM-MACH (Base)	Fixed function of latitude and Julian day
Major point source plumerise algorithm	Akingunola <i>et al.</i> , 2018	As in GEM-MACH (Base)	Briggs (1984)
Gas-phase chemistry solver	KPP2.1 (Sandu and Sander, 2006)	As in GEM-MACH (Base)	Young and Boris (1977)
Vehicle Induced Turbulence	Makar <i>et al.</i> (2021)	As in GEM-MACH (Base)	None
Forest Canopy shading and turbulence	Makar <i>et al.</i> (2017)	As in GEM-MACH (Base)	None
CH ₄ as chemically active tracer	Yes	As in GEM-MACH (Base)	No
Aerosol direct and indirect effect feedback	Yes (Makar <i>et al.</i> , 2015a,b)	As in GEM-MACH (Base)	No
Floor (minimum) PBL height imposed	No	As in GEM-MACH (Base)	Yes (100m)



Area source emissions treatment	Flux lower boundary condition on diffusion equation	As in GEM-MACH (Base)	Mass injection into two lowest model layers
Advection mass conservation	ILMC, 3 sweeps (Sorensen <i>et al.</i> , 2013)	As in GEM-MACH (Base)	ILMC, 2 sweeps, followed by Bermejo-Conde (2002) global mass correction

707

708 3.0 Results

709 3.1 Critical Load Exceedances

710 3.1.1 Europe, Acidification

711 Critical load exceedances for acidification for each of the four European (EU) models are shown in Figure
712 2 for 2010 and in Figure S1 (SI) for 2009. Figure 3 shows the reduced ensemble values for 2009 and
713 2010 (a,b) as well as common AQMEII4 domain total bar charts for all models and the ensembles (c).

714 The EU exceedances for acidity are similar between the two years (compare Figures 2 and S1, and values
715 for each year in Figure 3). However, differences between models within a given year are larger
716 (especially in an absolute sense; WRF-Chem (IASS) <0.4% in exceedance, WRF-Chem (UPM): ~6.5%).
717 Low WRF-Chem (IASS) exceedance levels are in part due to unreported deposition data (see section
718 2.2.2); the reduced ensemble maps in Figure 3 show the ensemble average for LOTOS-EUROS (TNO),
719 WRF-Chem (UPM) and CMAQ (Hertfordshire). The EU reduced ensemble shows the greatest extent of
720 exceedance in the Netherlands along the Netherlands/Belgium border, north-western Germany, southern
721 Norway, and along the border between Poland and Germany (Figure 3(a,b)). Individual models in Figure
722 2 show additional acidity “hotspots” that may appear in one model and not in another (e.g. LOTOS-
723 EUROS (TNO): near Lucerne and Bonn; WRF-Chem (UPM): westernmost Switzerland, south-central
724 Germany, and Belgrade; CMAQ (Hertfordshire): south-west Switzerland, south-central Germany, and
725 south-west Romania).

726 The percent area of EU acidification CLE over the region for which CL data was available, for the
727 reduced ensemble, was 4.48% (range 2.37% to 6.85%) in 2009 and 4.32% (2.06 to 6.52%) in 2010.
728 Average reduced ensemble accumulated exceedance for EU acidity was 13.8 (9.7 to 27.1) eq ha⁻¹ yr⁻¹ in
729 2009, and 12.6 (7.8 to 23.7) eq ha⁻¹ yr⁻¹ in 2010. The quoted range is from the highest and lowest
730 members in the 3-member reduced ensemble.

731 3.1.2 Europe, Eutrophication

732 Critical load exceedances for eutrophication for each of the four EU models are shown in Figure 4 for
733 2010 and in Figure S2 (SI) for 2009. Figure 5 shows the reduced ensemble values for 2009 and 2010
734 (a,b) as well as common AQMEII4 domain summaries for all models and the ensembles (c).

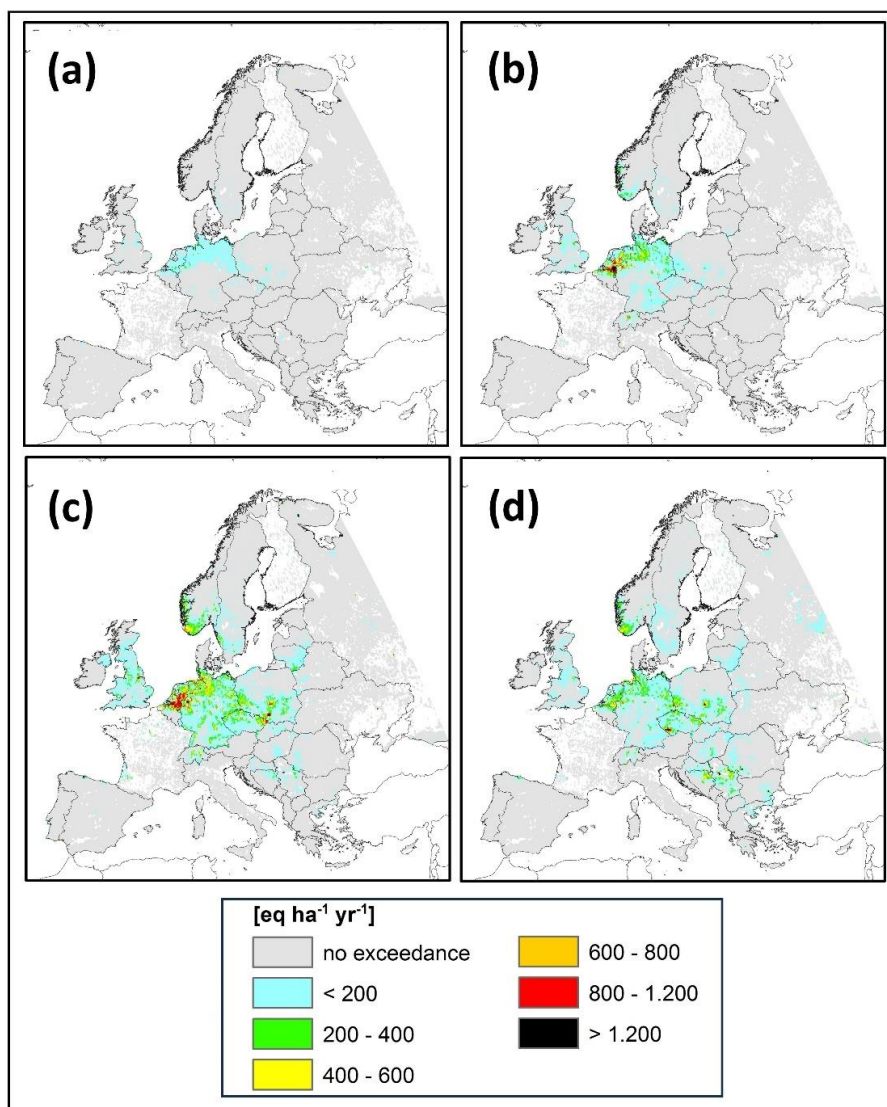
735 As for EU Acidity CLE’s, the Eutrophication CLE’s are very similar between the two model years
736 (compare Figures 4 and S2, and the values for each year in Figure 5). The spatial distribution of the
737 greatest levels of exceedance also varies more strongly between models. All members in the 3-member
738 reduced ensemble identify the Po river valley as reaching the greatest level of exceedance, but LOTOS-
739 EUROS (TNO) also shows high levels of exceedance in Benelux to northern Germany and in the



740 Barcelona area, while WRF-Chem (UPM) shows high levels of exceedance $> 800 \text{ eq ha}^{-1} \text{ yr}^{-1}$ in multiple
741 hotspots throughout the region.

742 The percentage of the area in exceedance for eutrophication is much higher than that of acidification
743 (reduced ensemble CLE 60.2% (47.3 to 73.3%) in 2009, and 62.2% 51.2 to 74.4%) in 2010). The
744 average accumulated exceedance was 156.9 (89.4 to 265.5) $\text{eq ha}^{-1} \text{ yr}^{-1}$ in 2009 and 161.4 (109.4 to
745 261.8) $\text{eq ha}^{-1} \text{ yr}^{-1}$ in 2010 (Figure 5, the range is from lowest and highest members in the 3-member
746 reduced ensemble).

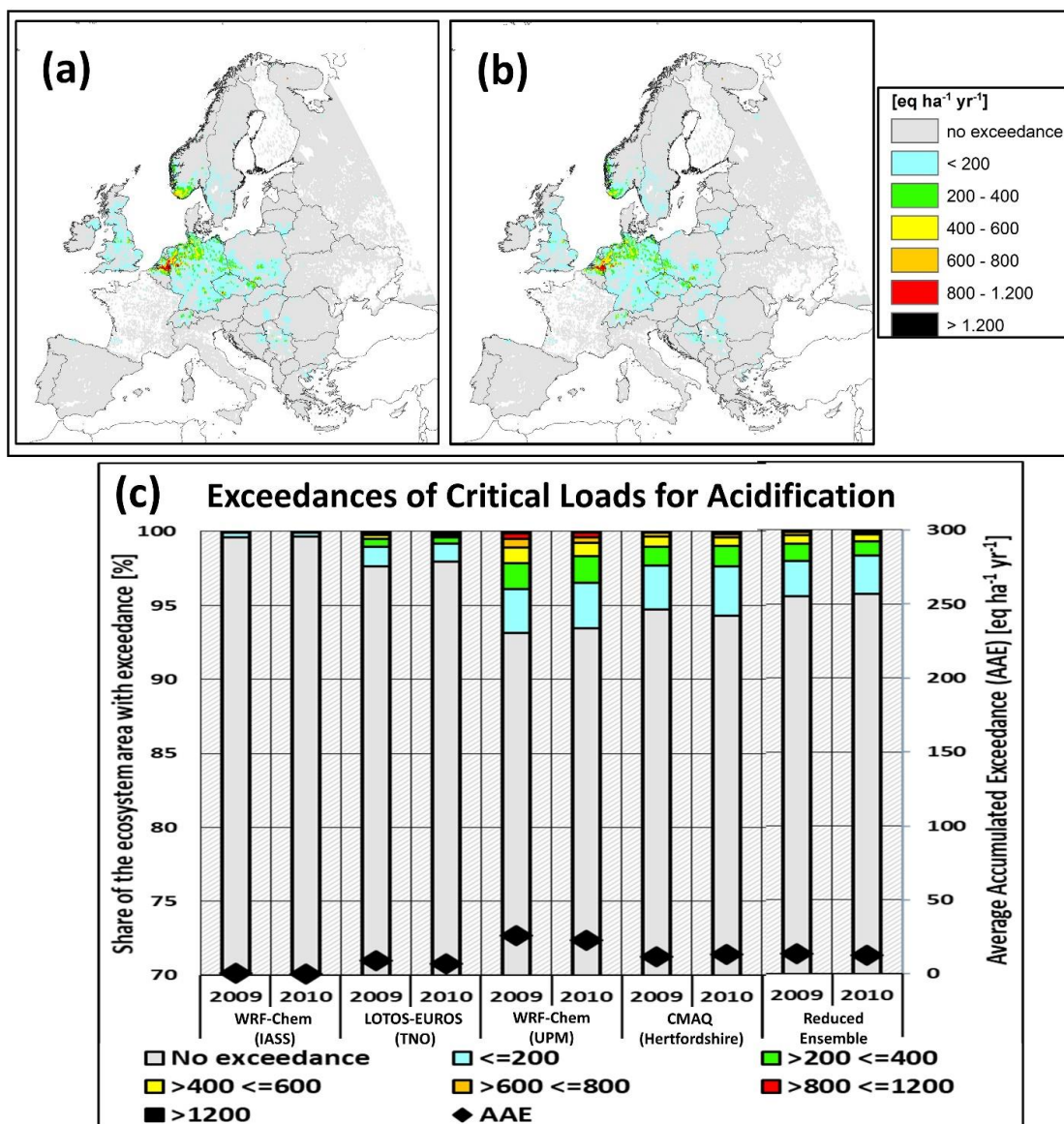
747 Figure 2. CLEs for Acidity, EU AQMEII4 common domain, 2010, $\text{eq ha}^{-1} \text{ yr}^{-1}$. (a) WRF-Chem (IASS), (b) LOTOS-
748 EUROS (TNO), (c) WRF-Chem (UPM), (d) CMAQ (Hertfordshire). Grey areas indicate regions for which critical
749 load data are available but are not in exceedance of critical loads. Coloured areas indicate exceedance regions.



750



751 Figure 3. Summary CLEs for Acidity, EU AQMEII4 common domain, eq ha⁻¹yr⁻¹. (a), (b) Spatial distribution of
 752 CLEs for the reduced ensemble for the years 2009 and 2010, respectively. (c) Percentage of ecosystems for which
 753 CL data are available that are in exceedance by model and year (left axis and colour bar) and average accumulated
 754 exceedance (eq ha⁻¹ yr⁻¹) (right axis and black diamond symbols).

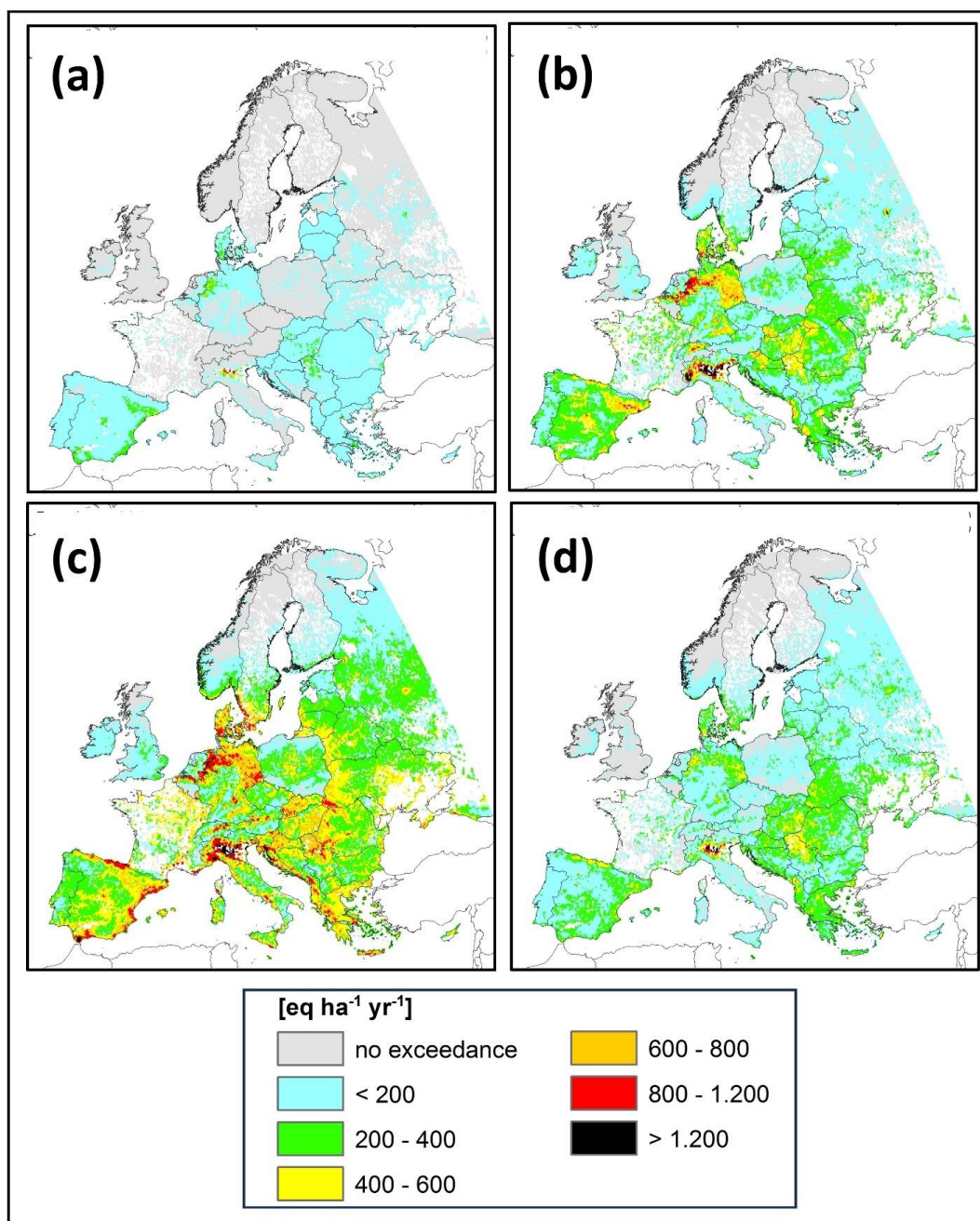


755

756



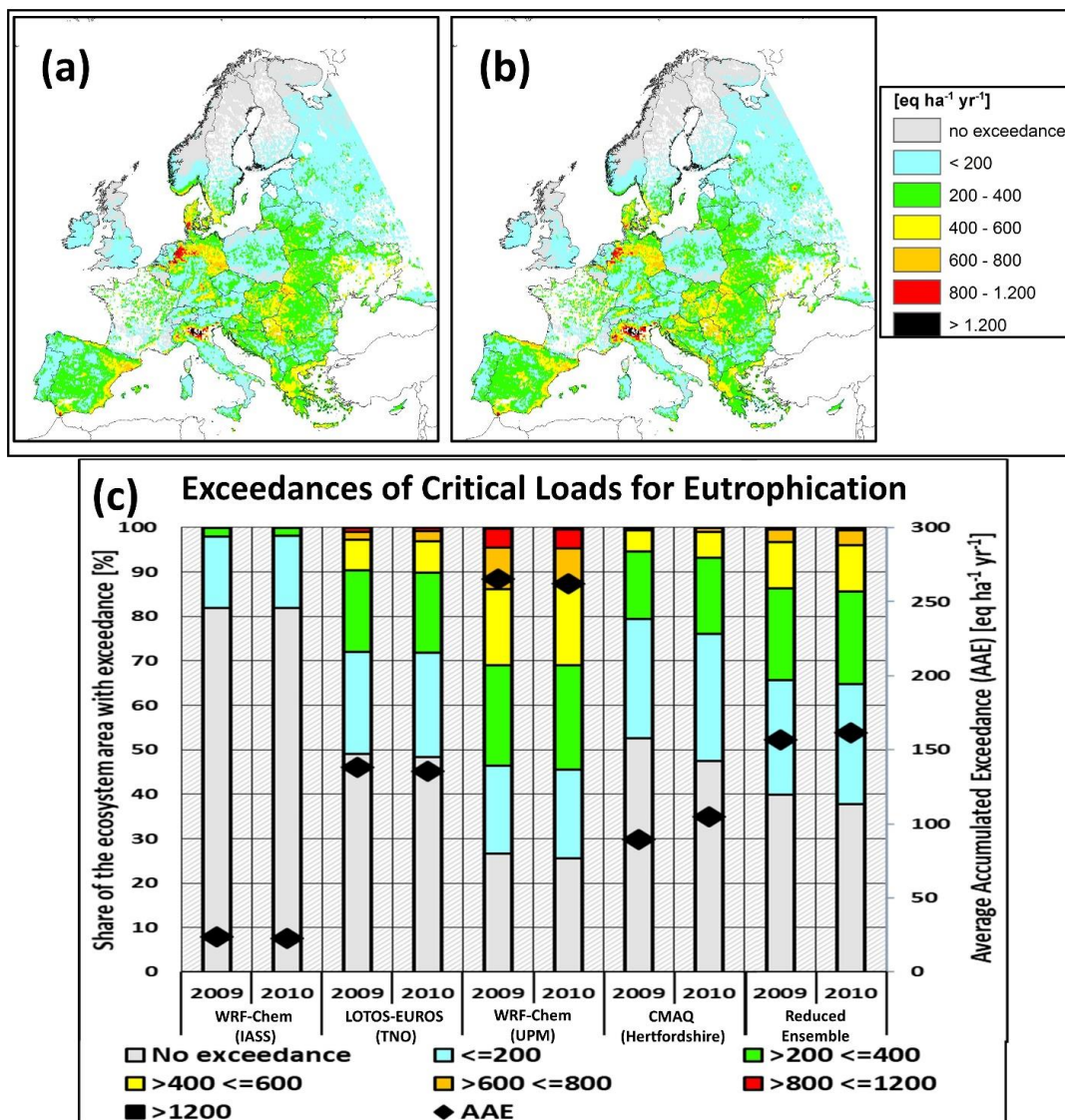
757 Figure 4. CLEs for Eutrophication, EU AQMEII4 common domain, 2010, eq ha⁻¹yr⁻¹. (a) WRF-Chem (IASS), (b)
758 LOTOS-EUROS (TNO), (c) WRF-Chem (UPM), (d) CMAQ (Hertfordshire). Grey areas indicate regions for which
759 critical load data are available but are not in exceedance of critical loads. Coloured areas indicate exceedance
760 regions.



761



762 Figure 5. Summary CLEs for Eutrophication, EU AQMEII4 common domain, eq ha⁻¹yr⁻¹. (a), (b) Spatial
 763 distribution of CLEs for the reduced ensemble for the years 2009 and 2010, respectively. (c) Percentage of
 764 ecosystems for which CL data are available that are in exceedance by model and year (left axis and colour bar) and
 765 average accumulated exceedance (eq ha⁻¹ yr⁻¹) (right axis and black diamond symbols).



766

767

768

769

770



771 *3.1.3 North America, Forest Ecosystems Simple Mass Balance Critical Load*

772 Critical load exceedances with respect to the North American (NA) forest soil acidity for the years 2016
773 and 2010 are shown in Figures 6 and S3, respectively, with the reduced ensemble maps for both years,
774 and the domain summaries shown in Figure 7.

775 Unlike the EU domain comparison, the NA CLEs depicted in Figure 6 show a large difference in the
776 extent of regions in exceedance for the different models. While all models with the exception of WRF-
777 Chem (IASS) identified the regions to the south and west of the Great Lakes, the U.S. east coast, and
778 Florida as being in exceedance, the magnitude of the exceedances varied greatly between the models,
779 with the GEM-MACH models (Figure 6(d-f)) showing large regions with exceedances above 800 eq ha⁻¹
780 yr⁻¹, followed by, in descending order, WRF-Chem (UPM), CMAQ-M3Dry, CMAQ-STAGE, WRF-Chem
781 (UCAR), and WRF-Chem (IASS).

782 The summary reduced ensemble CLE values (Figure 7) show the improvement in CLEs between the
783 years 2010 and 2016, which occurred in response to the legislated reduction in SO₂ emissions during this
784 time period. The summary chart (Figure 7 (c)) however shows that the magnitude of the response to the
785 SO₂ reduction was model dependent: the change between 2010 and 2016 was the greatest for GEM-
786 MACH (Base) in an absolute sense, and the greatest for WRF-Chem (UCAR) in a relative sense.
787 Similarly, the average accumulated exceedance (right-hand vertical axis and black diamonds, Figure 7(c))
788 showed decreases in exceedance between 2010 and 2016 for all models, but the extent of these decreases
789 differed, with WRF-Chem (UCAR) showing the smallest decrease in AAE from 2010 to 2016, followed
790 in increasing order of the magnitude of change by CMAQ-STAGE, CMAQ-M3Dry WRF-Chem (UPM),
791 GEM-MACH-Ops, GEM-MACH-Base, and GEM-MACH-Zhang.

792 The percentage of the NA forested area in exceedance for acidification for the reduced ensemble was
793 13.2% (2.8 to 22.2%) in 2010, and 6.1% (1.0 to 12.9%) in 2016. The ensemble thus shows a
794 considerable improvement in exceedances with respect to acidification between the two years.

795 *3.1.4 North America, Aquatic Ecosystems CL(A)*

796 Exceedances with respect to the North American aquatic ecosystem CL dataset for the years 2016 and
797 2010 are shown in Figures 8 and S4, respectively, with the reduced ensemble maps for both years and
798 domain summaries shown in Figure 9.

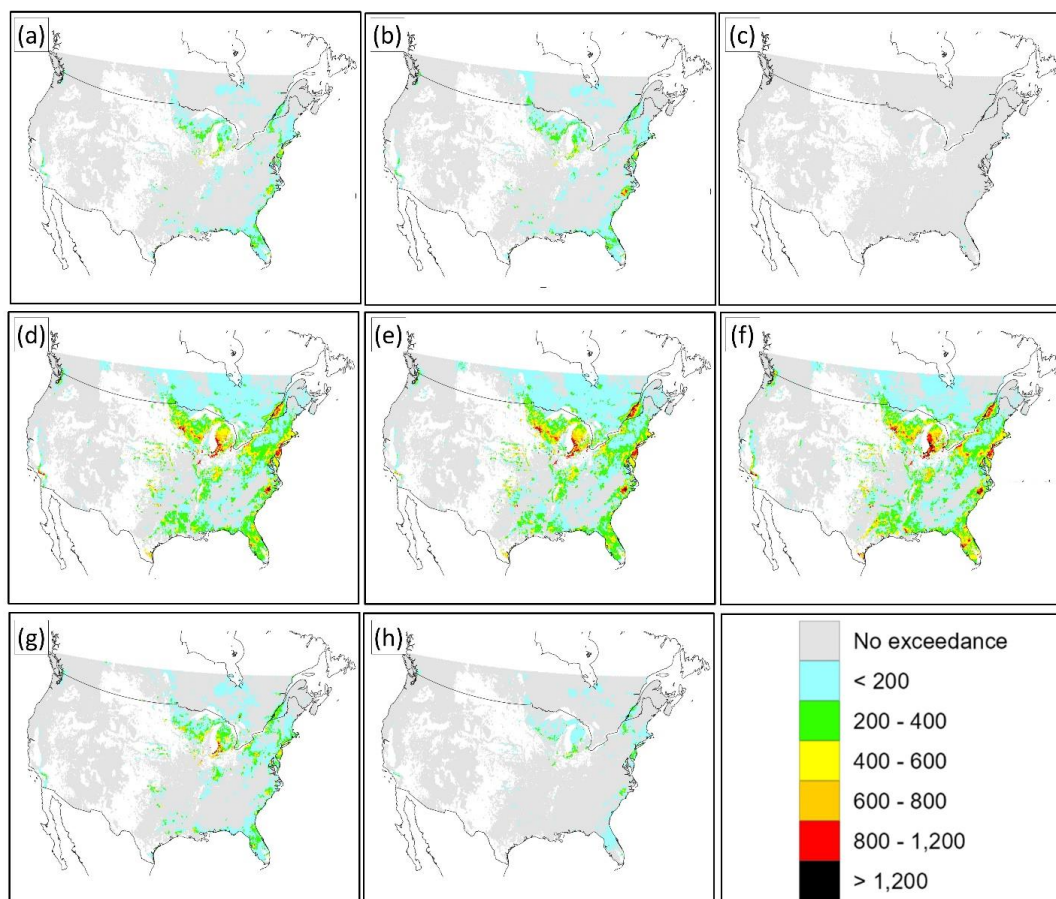
799 Comparison of Figures 6 and 8 shows a similarity in the CLE response of the individual models between
800 forest soil and aquatic ecosystems, with the GEM-MACH models predicting the highest number and
801 magnitude of exceedances, followed by WRF-Chem (UPM), WRF-Chem (UCAR) and the two CMAQ
802 implementations. Figure 9 (a,b) shows the expected decrease of the reduced ensemble's CLE between
803 2010 and 2016, as well as the higher levels of exceedance associated with the GEM-MACH and WRF-
804 CHEM (UPM) models, followed in descending order by the two CMAQ implementations and WRF-
805 CHEM (UCAR) (Figure 9 (c)).

806 The percentage of the NA aquatic ecosystems in exceedance for the reduced ensemble was 21.2% (12.8 to
807 28.9%) in 2010 and 11.4% (7.3 to 15.8%) in 2016. The reduced ensemble thus shows a considerable
808 improvement in exceedances with respect to exceedance of aquatic critical loads between the two years,
809 again by almost a factor of two.

810



811 Figure 6. CLEs for Forest Soils, NAAQMEI4 common domain, 2016, eq ha⁻¹yr⁻¹. (a) CMAQ-M3Dry,
812 (b) CMAQ-STAGE, (c) WRF-Chem (IASS), (d) GEM-MACH (Base), (e) GEM-MACH (Zhang), (f)
813 GEM-MACH (Ops), (g) WRF-Chem (UPM), (h) WRF-Chem (UCAR). Grey areas indicate regions for
814 which critical load data are available but are not in exceedance of critical loads. Coloured areas indicate
815 exceedance regions.

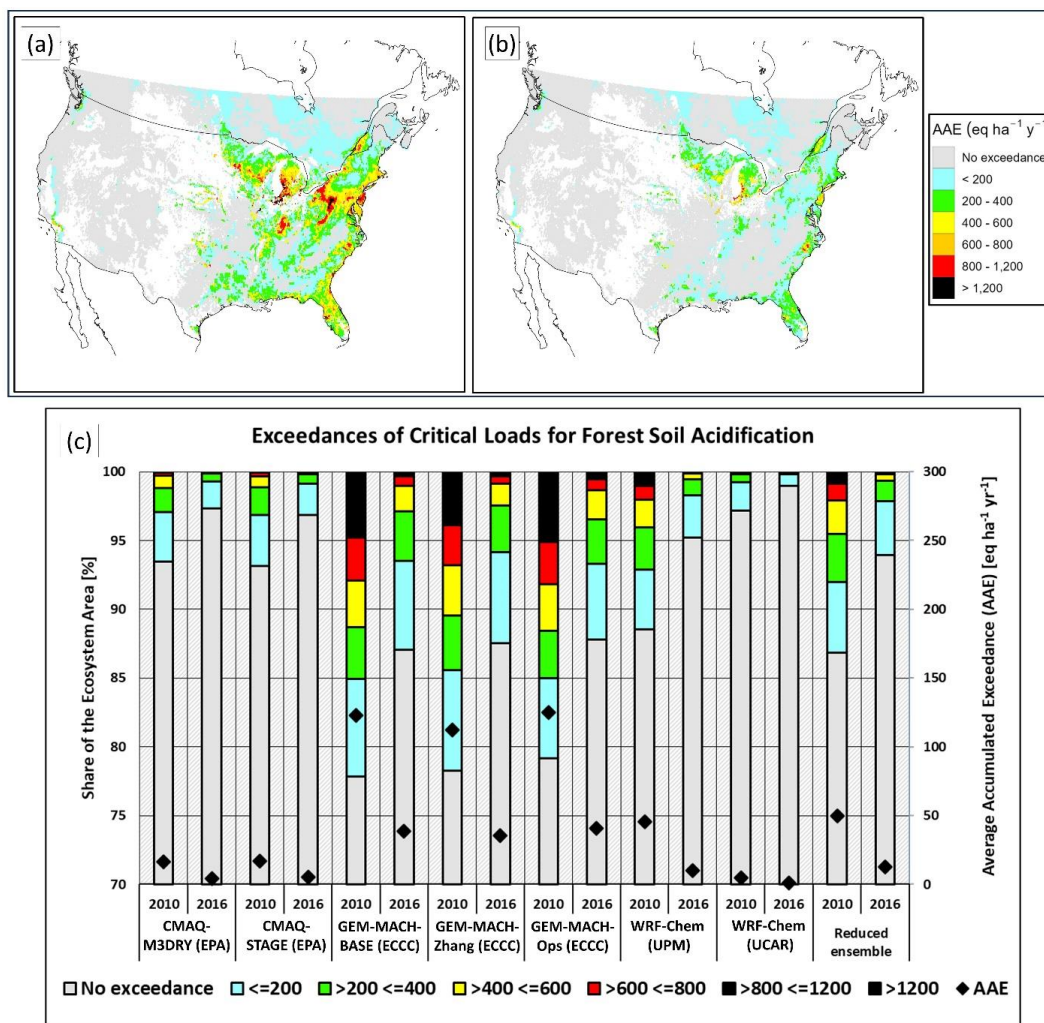


816

817



818 Figure 7. Summary CLEs for Forest Soils, NAAQMEII4 common domain, eq ha⁻¹ yr⁻¹. (a), (b) Spatial
 819 distribution of CLEs for the reduced ensemble for the years 2010 and 2016, respectively. (c) Percentage
 820 of ecosystems for which CL data are available that are in exceedance by model and year (left axis and
 821 colour bar) and average accumulated exceedance (eq ha⁻¹ yr⁻¹) (right axis and black diamond symbols).



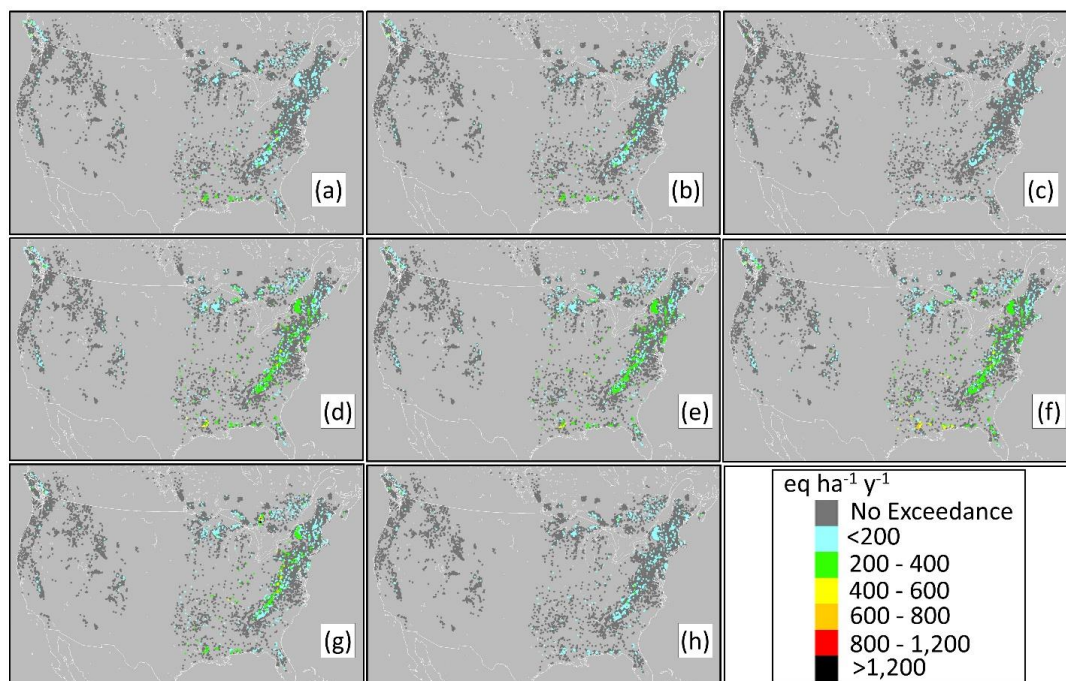
822

823

824



825 Figure 8. CLEs for Aquatic Ecosystems, NA AQMEII4 common domain, 2016, eq ha⁻¹ yr⁻¹. Panels
826 arranged by Model as in Figure 6; individual sites are shown as pixels. Dark grey pixels indicate regions
827 for which critical load data were available but were not in exceedance of critical loads. Coloured areas
828 indicate exceedance regions; overplotting in precedence by the extent of exceedance was carried out for
829 overlapping pixels. Areas of no CL data are shown in lighter grey.

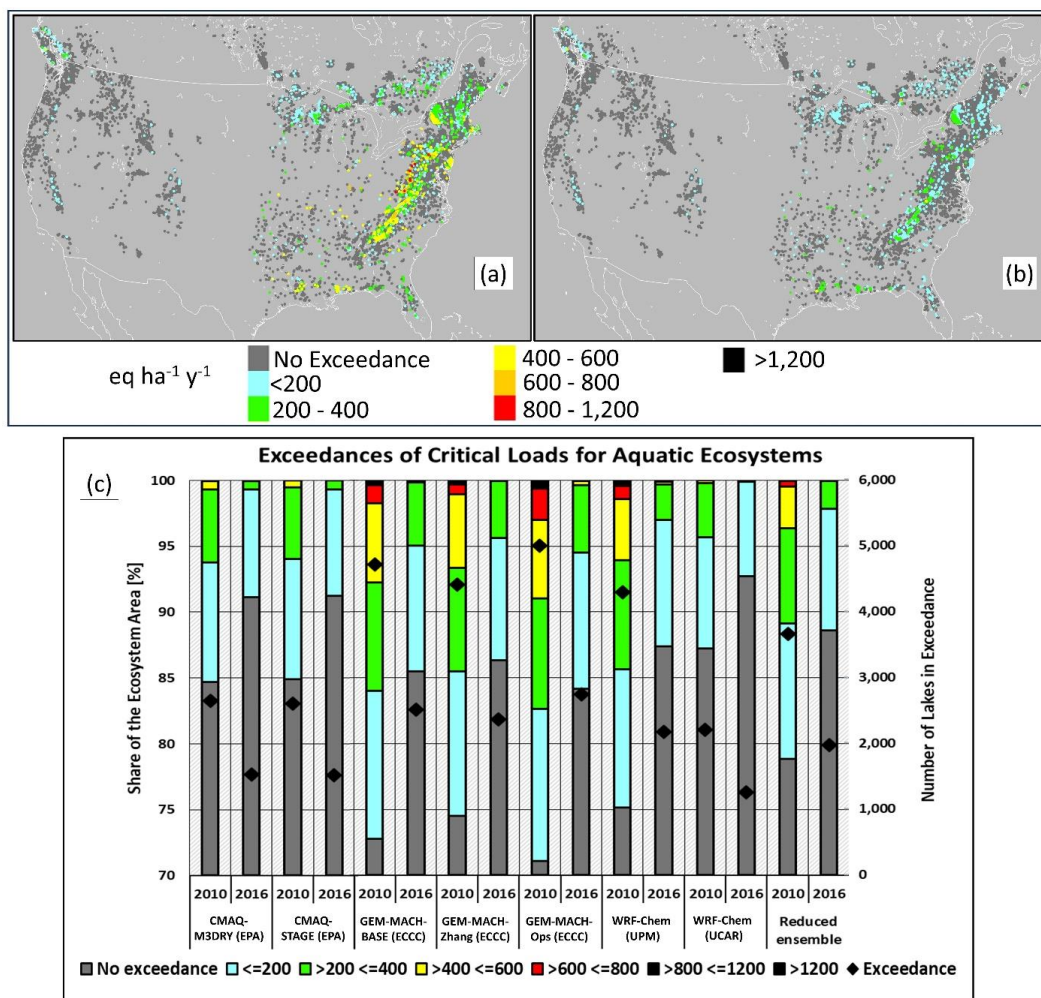


830

831



832 Figure 9. Summary CLEs for Aquatic Ecosystems, NAAQMEII4 common domain. (a), (b) Spatial
 833 distribution of CLEs for the reduced ensemble for the years 2010 and 2016, respectively. (c) Percentage
 834 of lakes for which CL data are available that are in exceedance by model and year (left axis and colour
 835 bar) and number of lakes in exceedance (right axis and black diamond symbols).



836

837

838



839 *3.1.5 U.S. N Deposition to Lichen*

840 Exceedances with respect to the USA CL of N for a 20% decline in sensitive epiphytic lichen species
841 richness (221 eq-N ha⁻¹ yr⁻¹) dataset for the years 2016 and 2010 are shown in Figures 10 and S5,
842 respectively, with the reduced ensemble maps for both years and domain summaries shown in Figure 11.

843 The overall pattern of exceedances and their magnitude across models (Figure 10) is similar to that of the
844 Forest Soil exceedances (Figure 6), with the largest magnitudes in the north-eastern continental USA and
845 in North Carolina, though the lichen exceedances are more continuous across the region than for forest
846 soil water acidity impacted ecosystems. GEM-MACH (Base), GEM-MACH (Zhang), and GEM-MACH
847 (Ops) have maximum exceedances usually between 800 and 1,200 eq ha⁻¹ yr⁻¹, and the exceedances
848 predicted by other models are less than 800 eq ha⁻¹ yr⁻¹ aside from a North Carolina exceedance hotspot
849 which is predicted by all models. The reduced ensemble overall magnitude of exceedances decreased
850 significantly between 2010 and 2016 (Figure 11(a,b), less black and red regions in the more recent year).
851 The reduced ensemble total area in exceedance has decreased slightly (Figure 11(c), “reduced ensemble”
852 columns). All models show a decreasing levels of exceedance between the two years, and slightly
853 decreasing total area of exceedance. The magnitude of exceedances differs significantly between the
854 models, with the highest magnitude exceedances predicted by the GEM-MACH group of models,
855 followed by WRF-Chem (UPM).

856 The percentage of the NA sensitive epiphytic lichen ecosystems in exceedance for the reduced ensemble
857 was 81.5% (69.3 to 95.0%) in 2010 and 75.8% (63.7 to 90.7%) in 2016.

858

859 *3.1.6 U.S. N Deposition to Herbaceous Plants*

860 Exceedances with respect to the USA CL of N for a decline in herbaceous species richness (436 to 1693
861 eq-N ha⁻¹ yr⁻¹) dataset for the years 2016 and 2010 are shown in Figures 12 and S6, respectively, with the
862 reduced ensemble maps for both years and domain summaries shown in Figure 13.

863 The spatial distribution of the regions of highest exceedance shares some common features with that of
864 sensitive epiphytic lichen (compare Figure 12 with Figure 10), such as maximum exceedances in NE
865 USA, North Carolina, and extending along a region north of Texas. However, both the magnitude and
866 extent of exceedance is much more varied for herbaceous species richness than for lichen species
867 richness, with the GEM-MACH suite of models (Figure 12 d-f and Figure 13c) predicting the highest
868 exceedance levels and up to 18.4% of the area in exceedance in 2016, the CMAQ implementations
869 varying between 0.6% and 0.8%, and WRF-Chem (UCAR) predicting 0.1%.

870 The percentage of the NA herbaceous plant ecosystems in exceedance for the reduced ensemble was
871 13.9% (0.4 to 39.5%) in 2010, and 3.9% (0.1 to 18.4%) in 2016, with the higher exceedance levels in the
872 range resulting from the GEM-MACH suite of models. Reduced ensemble herbaceous species richness
873 exceedances have decreased considerably between the two years in all models.

874 *3.1.7 Critical Load Exceedances, Key Results*

875 The percent exceedance for the reduced ensemble and ranges from the reduced ensembles for the
876 ecosystems examined here are summarized in Table 4. The values suggest acidification in EU will
877 happen over a smaller region than eutrophication at 2009/2010 emissions levels, with a slight decrease in
878 acidification and a slight increase in eutrophication between the two years. About 60% of EU ecosystems
879 would be subject to eutrophication at some point in the future at 2010/2009 emissions levels. One



880 striking difference between the different model estimates of CLE is in the magnitude of exceedances (as
 881 opposed to the total area in exceedance). WRF-Chem (UPM) for example in Figures 2 and 4 predicts
 882 more severe levels of exceedance across Europe than the other models. The North America results
 883 suggest that reductions in SO₂ and NO_x emissions between 2010 and 2016 resulted in a substantial
 884 reduction in the number of forest soil and aquatic ecosystem acidification exceedances (by nearly a factor
 885 of two). The impacts of nitrogen deposition on herbaceous species also improved (by nearly a factor of
 886 three), while impacts of nitrogen deposition on sensitive lichen had more modest improvement (from 81.5
 887 to 75.8% in exceedance). The magnitude and spatial extent of these eutrophication exceedances were
 888 highly dependent on the model, and on the variations in the representation of sub-processes within each
 889 model, used for predictions. Understanding the large range of model predictions is one of the main aims
 890 of the current work. The next section discusses the underlying causes driving the model-to-model
 891 differences, using the AQMEII4 deposition diagnostics.

892 Table 4. Summary of reduced ensemble percent exceedance mean values and their range in EU and NA
 893 domains.

EU Ecosystem	Year 2009 Percent Exceedance (lower to upper bound)	Year 2010 Percent Exceedance (lower to upper bound)
Acidification	4.48 (2.37 to 6.85)	4.32 (2.06 to 6.52)
Eutrophication	60.2 (47.3 to 73.3)	62.2 (51.2 to 74.4)
NA Ecosystem	Year 2010 Percent Exceedance (lower to upper bound)	Year 2016 Percent Exceedance (lower to upper bound)
Forest Soils Acidification	13.2 (2.8 to 22.2)	6.1 (1.0 to 12.9)
Lake Ecosystems	21.2 (12.8 to 28.9)	11.4 (7.3 to 15.8)
USA N Deposition Lichen	81.5 (69.3 to 95.0)	75.8 (63.7 to 90.7)
USA N Deposition Herbaceous	13.9 (0.4 to 39.5)	3.9 (0.1 to 18.4)

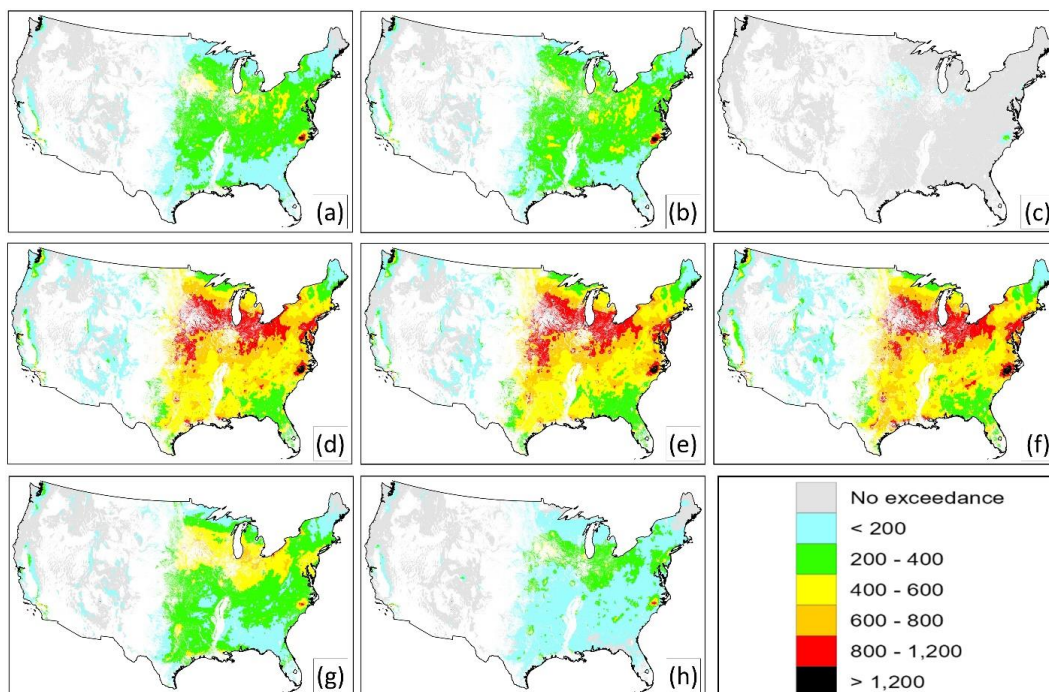
894

895

896



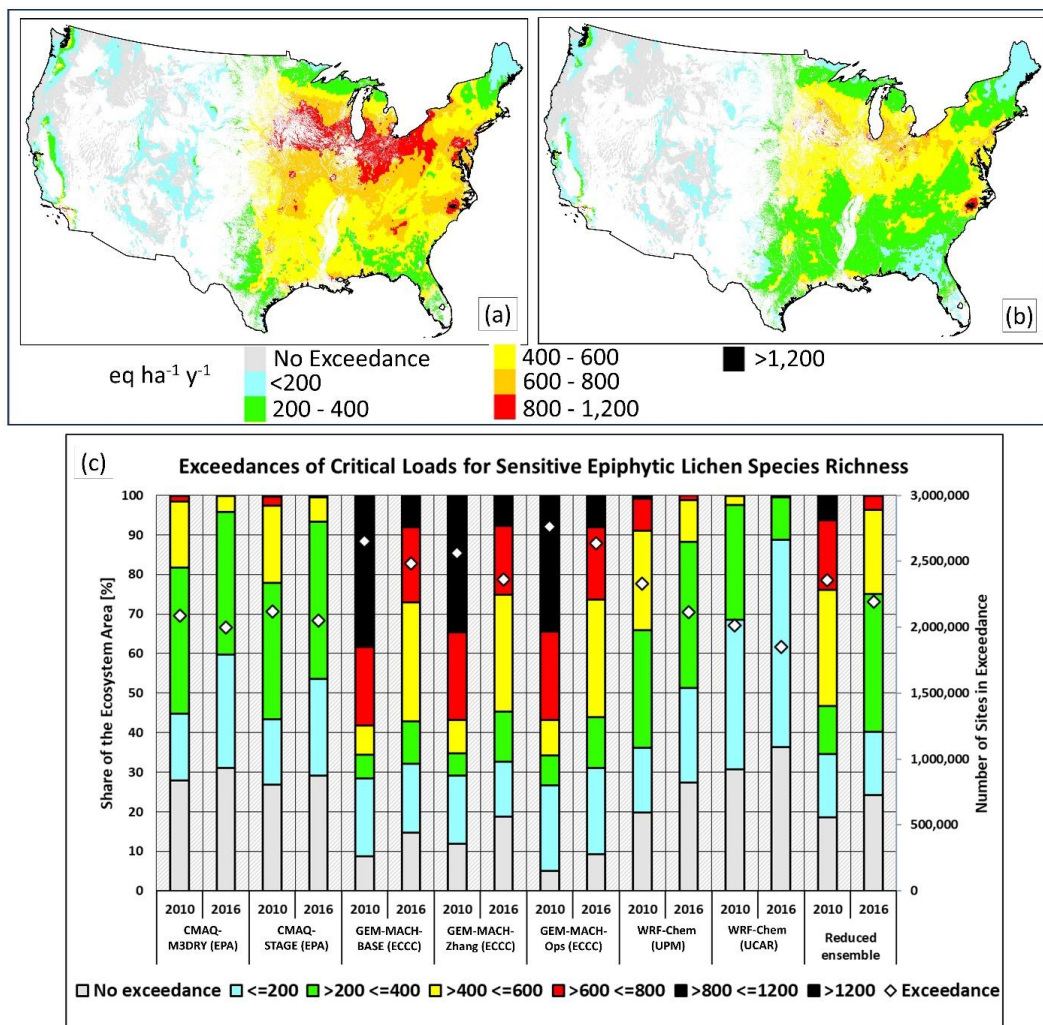
897 Figure 10. CLEs for Sensitive Epiphytic Lichen Species, NAAQMEII4 common domain, 2016, eq ha⁻¹
898 yr⁻¹. Panels arranged by model as in Figure 6. Light grey areas indicate regions for which critical load
899 data were available but were not in exceedance of critical loads. Coloured areas indicate exceedance
900 regions.



901



902 Figure 11. Summary CLEs, Sensitive Epiphytic Lichen Species, NAAQMEII4 common domain, eq ha⁻¹
 903 yr⁻¹. (a), (b) Spatial distribution of CLEs for the reduced ensemble for the years 2010 and 2016,
 904 respectively. (c) Percentage of sensitive epiphytic lichen ecosystems for which CL data are available that
 905 are also are in exceedance, by model and year (left axis and colour bar) and number of sites in exceedance
 906 (right axis and white diamond symbols).

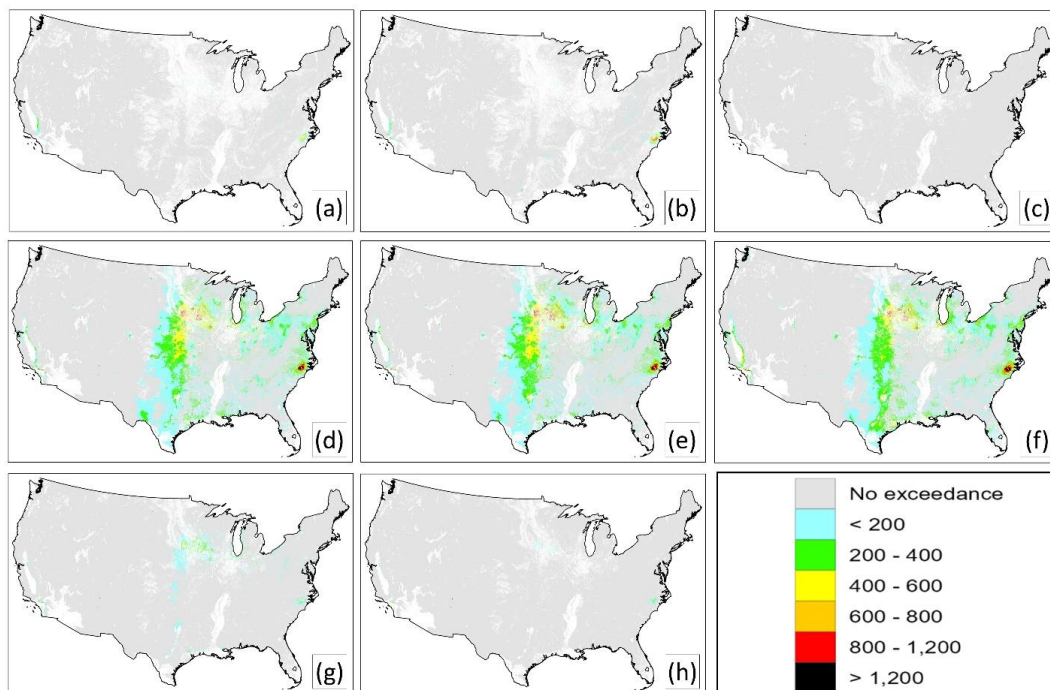


907

908



909 Figure 12. CLEs for a decline in Herbaceous Species Community Richness, NA common domain, 2016,
910 $\text{eq ha}^{-1}\text{yr}^{-1}$. Panels arranged by model as in Figure 6. Light grey areas indicate regions for which critical
911 load data were available but were not in exceedance of critical loads. Coloured areas indicate exceedance
912 regions.

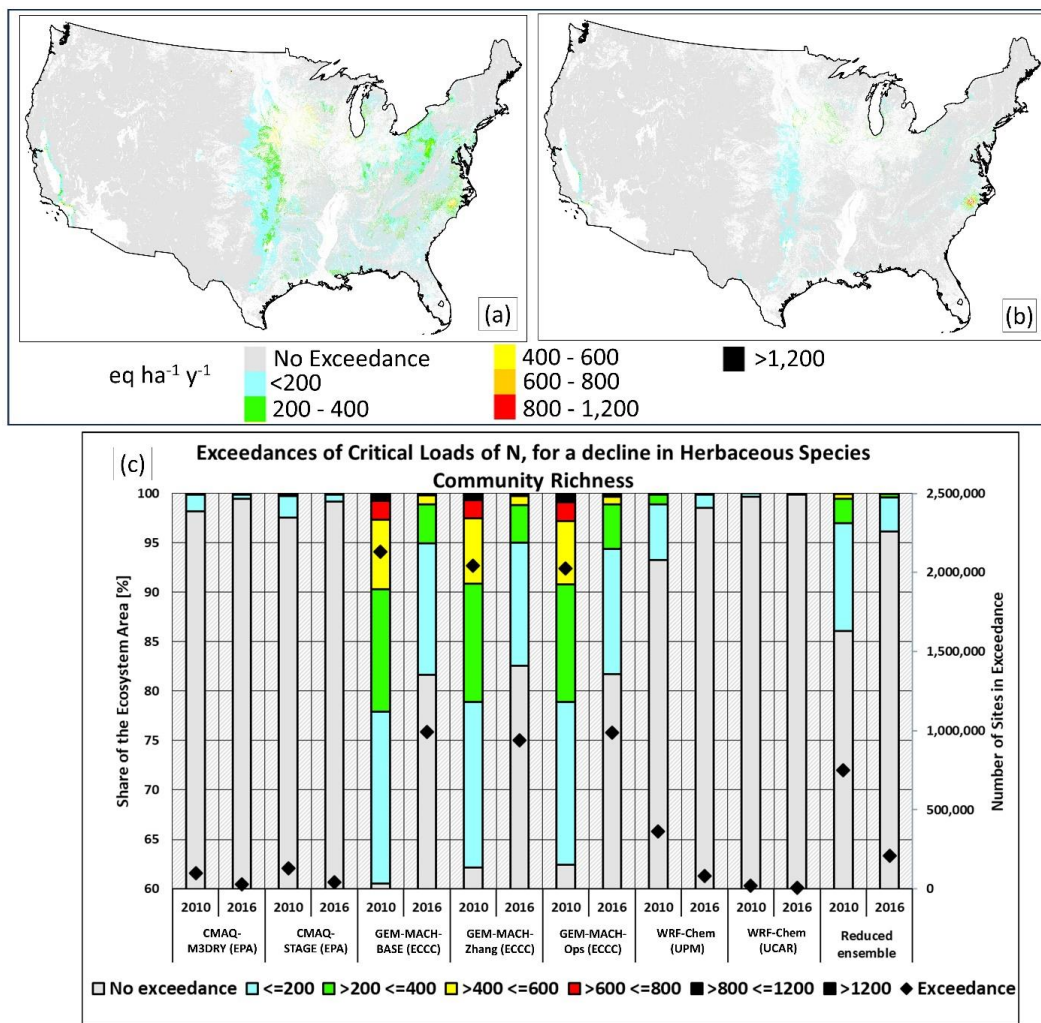


913

914



915 Figure 13. Summary CLEs for a decline in Herbaceous Species Community Richness, AQMEII4 NA
 916 common domain, eq ha⁻¹yr⁻¹. (a), (b) Spatial distribution of CLEs for the reduced ensemble for the years
 917 2010 and 2016, respectively. (c) Percentage of herbaceous species communities for which CL data are
 918 available that are also are in exceedance, by model and year (left axis and colour bar) and number of sites
 919 in exceedance (right axis and white diamond symbols).



920

921



922 3.2 Analysis of Model Deposition Predictions

923 3.2.1 Causes of S Deposition Variability in North America Domain Simulations

924 The AQMEII4 common grid average, and percent contribution of each depositing species towards total S
 925 deposition in 2016, are given in Table 5. The averages and standard deviation for the reduced ensemble
 926 show that wet deposition of the sum of the sulphate and bisulphite ions (SO_4^{2-} and HSO_3^{-}) contributes
 927 more to total S deposition than particulate sulphate dry deposition, which is in turn contributes more than
 928 SO_2 (g) dry deposition. However, the model-to-model variability is also large, particularly for the
 929 contribution of particulate sulphate, which varies by nearly two orders of magnitude between GEM-
 930 MACH (Base, Zhang Ops) and WRF-Chem (UPM). The contributions to the average reduced ensemble
 931 total S deposition are 62.0 ± 19.3 , 44.8 ± 39.0 , and 28.8 ± 9.9 $\text{eq ha}^{-1} \text{yr}^{-1}$ for wet, particle dry and gas dry
 932 deposition respectively (\pm ranges in Table 5 are the standard deviation of the component). The greatest
 933 cause of model *variability* in absolute total deposition is associated with the contribution of particulate
 934 sulphate dry deposition, followed by sulphur wet deposition and then gaseous SO_2 dry deposition.

935 Table 5. Average S deposition contributions in common AQMEII4 NA grid area ($\text{eq ha}^{-1} \text{yr}^{-1}$) and percent
 936 contribution to average total S deposition, 2016. n/d = no data submitted or insufficient data to calculate percentage.

Model Number	Average Deposition ($\text{eq ha}^{-1} \text{yr}^{-1}$)				Percent of total S deposition		
	$\text{SO}_4^{2-} + \text{HSO}_3^{-}$ Wet Deposition	Particle Sulphate Dry Deposition	$\text{SO}_2(\text{g})$ Dry Deposition	Total S Deposition	$\text{SO}_4^{2-} + \text{HSO}_3^{-}$ Wet Deposition	Particle Sulphate Dry Deposition	$\text{SO}_2(\text{g})$ Dry Deposition
CMAQ-M3Dry	79.0	19.0	24.9	122.9	64.3	15.4	20.2
CMAQ-STAGE	79.2	21.0	23.3	123.4	64.2	17.0	18.8
WRF-Chem (IASS)	0.9	nd	26.7	n/d	n/d	n/d	n/d
GEM-MACH (Base)	52.4	90.7	23.0	166.1	31.5	54.6	13.9
GEM-MACH (Zhang)	51.4	88.8	25.1	165.3	31.1	53.7	15.2
GEM-MACH (Ops)	81.3	88.2	23.9	193.4	42.0	45.6	12.4
WRF-Chem (UPM)	66.3	2.8	52.8	121.9	54.4	2.3	43.3
WRF-Chem (UCAR)	24.4	3.0	28.7	56.1	43.5	5.3	51.2
Reduced ensemble average	62.0	44.8	28.8	135.6	45.7	33.0	21.2
Reduced ensemble standard deviation	19.3	39.0	9.9	41.3	13.0	21.2	14.5

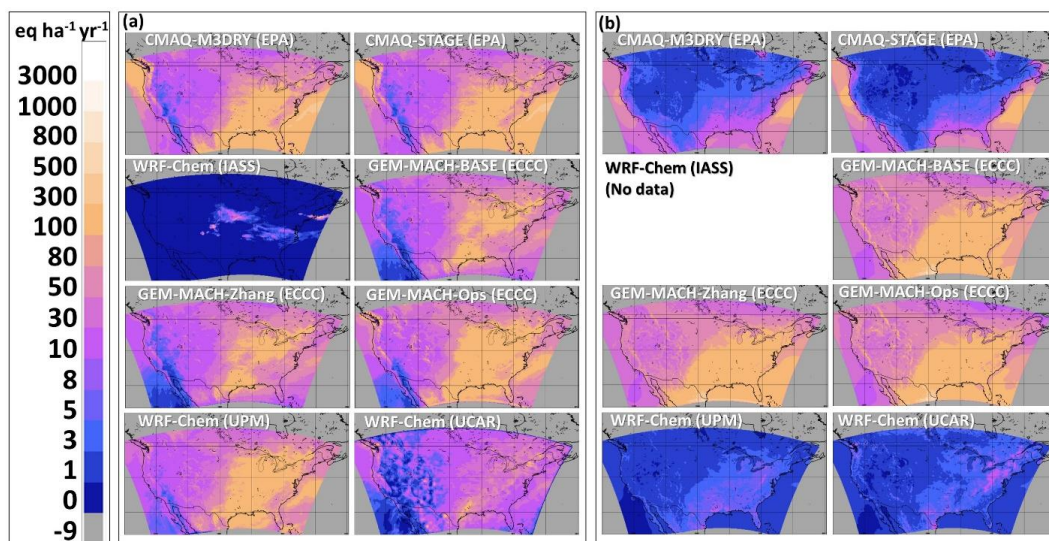
937



938 The spatial distributions of the two largest components of the total S deposition variability (wet S and dry
 939 particle S) are shown in Figure 14. The WRF-Chem (IASS) values did not represent the expected sources
 940 of S deposition over the continent and some deposition fields such as the total particulate sulphate dry
 941 deposition were not submitted. The wet S deposition maps are qualitatively similar between the other
 942 models (note that the colour scale is logarithmic), with WRF-Chem (UCAR) having the lowest values
 943 (Figure 14(a)). As shown in Table 5, the greatest degree of variability between the different modelling
 944 platforms is in the particle deposition fluxes (Figure 14(b)). This variability extends over orders of
 945 magnitude. WRF-Chem (UPM) and WRF-Chem (UCAR) predict the lowest deposition fluxes of dry
 946 particulate sulphate over both land and ocean. CMAQ-STAGE and CMAQ-M3Dry predict higher values
 947 over parts of the ocean, but relatively low values over land. GEM-MACH (Base), GEM-MACH (Zhang)
 948 and GEM-MACH (Ops) have the highest particulate sulphate dry deposition fluxes, roughly equivalent to
 949 the wet deposition fluxes.

950 We next evaluate each of the models' predictions against North American network observations for
 951 concentrations of SO₂ and particulate sulphate, and wet sulphur deposition for the year 2016. The
 952 monitoring network databases employed included the U.S. Environmental Protection Agency's Air
 953 Quality System (AQS; <https://www.epa.gov/aqs>, last access: 7 July 2024), the National Atmospheric
 954 Deposition Program's National Trend Network (NADP NTN;
 955 <https://nadp.slh.wisc.edu/networks/national-trends-network/>, last access 7 July 2024), the Canadian
 956 National Air Pollution Surveillance (NAPS) program ([https://www.canada.ca/en/environment-climate-change-
 957 change/services/air-pollution-monitoring-networks-data/national-air-pollution-program.html](https://www.canada.ca/en/environment-climate-change/services/air-pollution-monitoring-networks-data/national-air-pollution-program.html), last access:
 958 7 July 2024), and the Canadian National atmospheric chemistry database (
 959 [https://www.canada.ca/en/environment-climate-change/services/air-pollution-monitoring-networks-
 960 data/national-atmospheric-chemistry-database.html](https://www.canada.ca/en/environment-climate-change/services/air-pollution-monitoring-networks-data/national-atmospheric-chemistry-database.html), last access 7 July 2024).

961 Figure 14. 2016 total annual deposition flux (eq ha⁻¹ yr⁻¹) of (a) wet S, and (b) dry particulate sulphate.



962

963

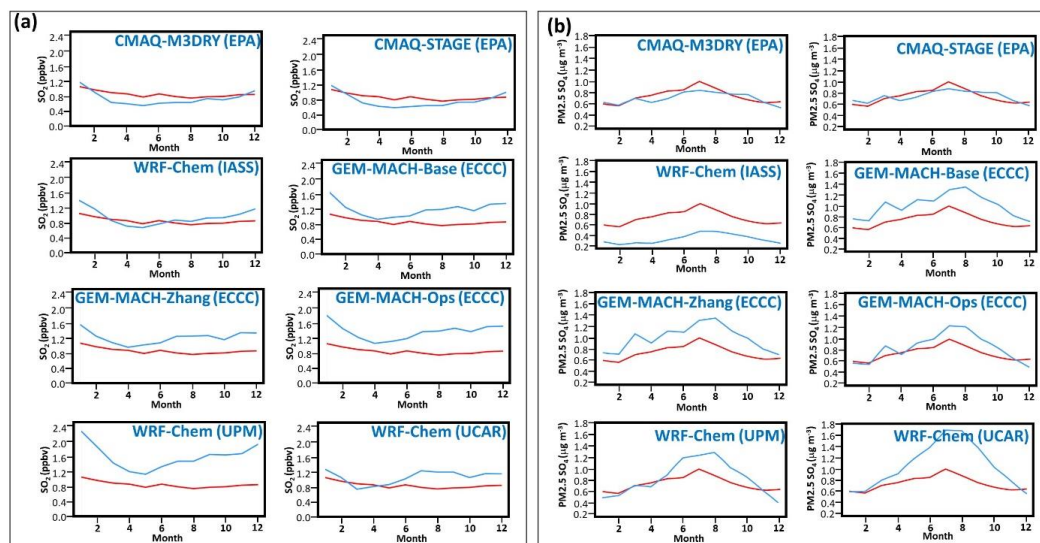


964 The NA models' monthly average values of hourly near-surface SO₂ (g) concentrations and daily
 965 particulate sulphate concentrations are compared to observations in Figure 15. The monthly averages of
 966 daily (CAPMoN) and weekly (NADP) wet S deposition are shown in Figure 16. Model-observation
 967 evaluation statistics are compared in Table 6. Station locations for the observations are shown in SI
 968 Figures S7, S8, and S9.

969 Table 6 shows that CMAQ-M3Dry and CMAQ-STAGE had the best values for most metrics, for the
 970 concentrations of SO₂ and PM_{2.5} sulphate, and daily wet sulphur deposition. The CMAQ-M3Dry,
 971 CMAQ-STAGE and WRF-Chem (IASS) had predominantly negative biases, and all other models had
 972 positive biases. The same tendency can be seen in Figure 15(a), where CMAQ-M3Dry and CMAQ-
 973 STAGE negative biases can be seen to occur in the warmer months, WRF-Chem (IASS) negative biases
 974 in the spring. Despite these differences, the net contribution of SO₂ dry deposition flux towards total
 975 sulphur deposition on an *annual* basis is relatively similar across the models (Table 5), with the standard
 976 deviation being relatively small, mostly driven by the SO₂ deposition flux for WRF-Chem (UPM) being
 977 higher than for the other models.

978 Particle sulphate (Figure 15(b), and Table 6) values were also closest to monthly observed values for
 979 CMAQ-M3Dry and CMAQ-STAGE, while being biased negative for WRF-Chem (IASS) and biased
 980 positive for the remaining models. The evaluation of total S wet deposition (Figure 16(a), Table 6)
 981 showed that all models with the exception of GEM-MACH (Ops) had negative biases relative to the
 982 Canadian daily wet S deposition observations. Weekly wet S deposition biases are also negative for most
 983 models (Table 6, Figure 16(b)), with only GEM-MACH-Ops having a positive bias in the ensemble.

984 Figure 15. Comparison of model (blue line) and observed (red line) monthly average surface
 985 concentrations of (a) hourly SO₂ (ppbv) and (b) daily PM_{2.5} sulphate (ug m⁻³), for the year 2016 (AQS,
 986 NAPS data).

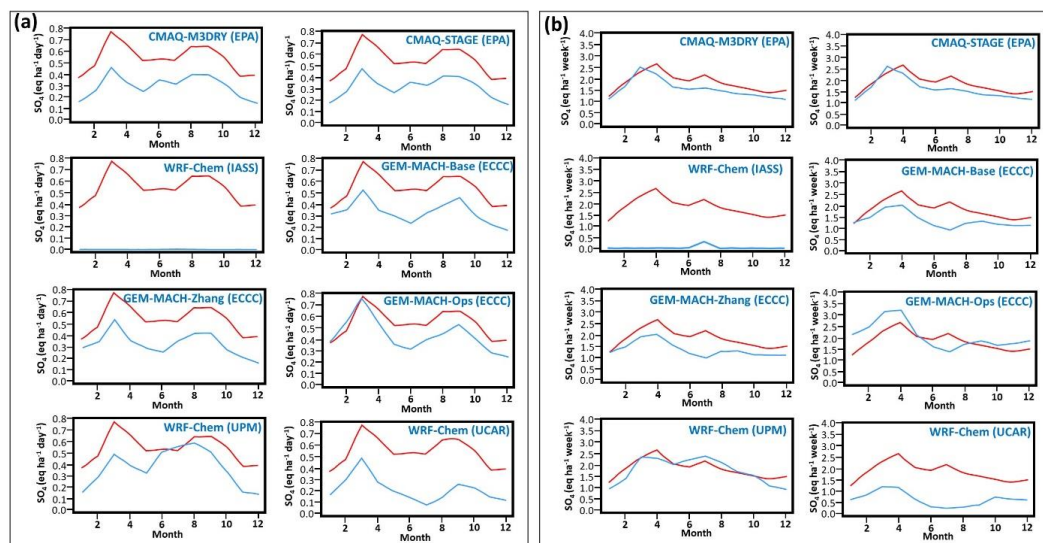


987

988



989 Figure 16. Comparison of model (blue line) and observed (red line) monthly average values of wet
 990 sulphur deposition for (a) daily CAPMoN data ($\text{eq ha}^{-1} \text{day}^{-1}$), (b) weekly NADP data ($\text{eq ha}^{-1} \text{week}^{-1}$), for
 991 the year 2016.



992

993 Factors aside from emissions which affect the SO_2 concentrations within the models are the loss processes
 994 of gas oxidation, uptake into hydrometeor water (and subsequent in-cloud oxidation), and dry deposition.
 995 Both the gas oxidation and hydrometeor uptake pathways may lead to particulate sulphate formation
 996 (through nucleation/condensation of sulphuric acid into particles and through evaporation of
 997 hydrometeors). An underestimate of chemical conversion of SO_2 within hydrometeors may thus be
 998 expected to result in underestimates of particulate sulphate and in sulphate ion wet deposition. However,
 999 Table 16 shows relatively little bias for $\text{PM}_{2.5}$ sulphate relative to observations for CMAQ-M3Dry and
 1000 CMAQ-STAGE, and positive biases for the GEM-MACH models and WRF-Chem (UPM); these positive
 1001 biases in predicted particulate sulphate would argue against an insufficient conversion of SO_2 to
 1002 particulate sulphate in the latter group of models. Rather, the general tendency of negative biases in wet
 1003 sulphur deposition may indicate insufficient hydrometeor scavenging and subsequent aqueous-phase
 1004 oxidation of aerosols across all models. We also note that the mean bias of SO_2 concentrations for GEM-
 1005 MACH (Ops) is more positive than those of GEM-MACH (Base) and GEM-MACH (Zhang), while the
 1006 particulate sulphate bias was lower, and the wet sulphate deposition bias was higher. GEM-MACH (Ops)
 1007 makes use of an operational weather forecast for cloud fields, while GEM-MACH(Base) and GEM-
 1008 MACH(Zhang) make use of an explicit cloud microphysics scheme, which allows weather/air quality
 1009 feedbacks to be simulated, but tends to underestimate the cloud amounts when used at lower resolution
 1010 such as the 10km grid cell size used in the simulations for these three models in this study. The
 1011 differences between {GEM-MACH (Base), GEM-MACH (Zhang)} and GEM-MACH (Ops) may thus
 1012 reflect weaker scavenging of aerosols into clouds in the Base and Zhang implementations.

1013



1014 Table 6. Model Performance Metrics for SO₂, PM_{2.5} SO₄, Wet deposition of S, AQMEII4 North
 1015 American domain, 2016. Bold-face letters show the highest scoring model.

Hourly SO ₂ (units ppbv where applicable)								
Performance Measure	CMAQ-M3Dry	CMAQ-STAGE	WRF-Chem (IASS)	GEM-MACH (Base)	GEM-MACH (Zhang)	GEM-MACH (Ops)	WRF-Chem (UPM)	WRF-Chem (UCAR)
FAC2	0.27	0.28	0.26	0.28	0.28	0.28	0.26	0.29
MB	-0.18	-0.17	-0.03	0.11	0.14	0.24	0.61	0.17
MGE	0.91	0.91	1.02	1.08	1.09	1.17	1.43	1.09
NMGE	1.02	1.02	1.15	1.21	1.22	1.32	1.60	1.22
RMSE	3.14	3.14	3.29	3.33	3.34	3.51	3.75	3.21
R	0.15	0.15	0.12	0.14	0.14	0.13	0.13	0.13
COE	0.04	0.03	-0.08	-0.14	-0.16	-0.24	-0.51	-0.15
IOA	0.52	0.52	0.46	0.43	0.42	0.38	0.25	0.43
PM _{2.5} SO ₄ (units µg m ⁻³ , where applicable)								
FAC2	0.77	0.76	0.33	0.65	0.66	0.63	0.67	0.59
MB	-0.04	0.00	-0.41	0.28	0.26	0.10	0.10	0.32
MGE	0.31	0.32	0.45	0.50	0.50	0.46	0.43	0.55
NMGE	0.43	0.43	0.60	0.68	0.67	0.62	0.58	0.75
RMSE	0.89	0.89	1.00	1.10	1.09	1.06	1.00	1.12
R	0.45	0.46	0.40	0.40	0.40	0.38	0.39	0.40
COE	0.37	0.36	0.10	-0.02	0.00	0.07	0.13	-0.12
IOA	0.68	0.68	0.55	0.49	0.50	0.54	0.57	0.44
Daily Total Wet S Deposition (units eq ha ⁻¹ d ⁻¹ , where applicable)								
FAC2	0.35	0.36	0.00	0.40	0.40	0.41	0.39	0.19
MB	-0.19	-0.17	-0.57	-0.07	-0.08	0.09	-0.06	-0.31
MGE	0.37	0.37	0.57	0.42	0.42	0.48	0.45	0.46
NMGE	0.65	0.65	1.00	0.74	0.74	0.85	0.79	0.81
RMSE	0.71	0.71	1.02	0.81	0.81	0.88	0.90	0.89
R	0.61	0.61	0.06	0.52	0.52	0.54	0.47	0.44
COE	0.31	0.31	-0.06	0.21	0.22	0.10	0.16	0.14
IOA	0.65	0.65	0.47	0.60	0.61	0.55	0.58	0.57
Weekly Total Wet S Deposition (units eq ha ⁻¹ week ⁻¹ , where applicable)								
FAC2	0.46	0.47	0.00	0.41	0.41	0.41	0.45	0.21
MB	-0.21	-0.17	-1.78	-0.41	-0.42	0.30	-0.03	-1.18
MGE	1.12	1.12	1.81	1.18	1.18	1.40	1.28	1.38
NMGE	0.62	0.62	1.00	0.65	0.66	0.78	0.71	0.76
RMSE	2.30	2.30	3.26	2.30	2.30	2.54	2.48	2.64
R	0.63	0.63	0.03	0.55	0.55	0.57	0.53	0.46
COE	0.34	0.34	-0.07	0.30	0.30	0.17	0.24	0.18
IOA	0.67	0.67	0.46	0.65	0.65	0.58	0.62	0.59

1016

1017 GEM-MACH (Base), GEM-MACH (Zhang) and WRF-Chem (UCAR) have the most positive biases for
 1018 particulate sulphate. As noted above, GEM-MACH (Base) and GEM-MACH (Zhang) share a common
 1019 framework, and unlike other models in the ensemble, they also share an implementation of the updated
 1020 particle deposition parameters of Emerson *et al.* (2020). The Emerson *et al.* (2020) makes use of
 1021 extensive measurement data, and compared to earlier parameterizations such as Zhang *et al.* (2001),
 1022 results in decreased dry deposition velocities for sub-micrometer particles and increased dry deposition
 1023 velocities for particles larger than 0.2 to 0.8 µm, depending on land use type. The increased PM_{2.5} SO₄
 1024 values in GEM-MACH (Base) and GEM-MACH (Zhang) in Figure 15(b) may thus reflect decreases in
 1025 the deposition removal flux in the sub-micrometer portion of the bins in these 12-bin sectional model



1026 framework. WRF-Chem (UPM) and WRF-Chem (UCAR) are also both sectional models making use of a
1027 common modelling framework, with WRF-Chem (UPM) being a slightly earlier release than WRF-Chem
1028 (UCAR). Neither model made use of the Emerson *et al.* (2020) update at the time the AQMEII4
1029 simulations took place. However, this option was later examined for the WRF-Chem (UCAR)
1030 configuration by Ryu and Min (2022), who found that the Emerson *et al.* (2020) dry deposition
1031 parameterization, applied subsequent to the runs carried out here, resulted in an increase in the positive
1032 PM_{2.5} bias from +4.5 to +6.7 $\mu\text{g m}^{-3}$ and a shift towards less negative biases in PM₁₀, from -19.7 to -1.77
1033 $\mu\text{g m}^{-3}$, similar to the biases in particulate sulphate and ammonium observed in Figure 15(b) between
1034 {GEM-MACH (Base), GEM-MACH(Zhang)} and GEM-MACH (Ops). Ryu and Min (2022) further
1035 found that the additional update of replacing the default Slinn (1984) aerosol cloud scavenging
1036 parameterization by the Wang (2014) parameterization offset the increase in PM_{2.5} SO₄ biases associated
1037 with the new particle dry deposition scheme, illustrating the extent to which combinations of
1038 parameterizations are sometimes needed to improve model performance. More recent versions of GEM-
1039 MACH also make use of multiphase hydrometeor partitioning, with and without the Wang (2014) semi-
1040 empirical scavenging scheme, with a significant increase in the uptake of particulate sulphate depending
1041 on precipitation rate, and improvements in the wet sulphate performance relative to previous model
1042 versions (Ghahreman *et al.*, 2024). Implementation of both updated particle dry deposition velocities and
1043 wet scavenging methodology have thus resulted in reduced biases for these fields, for several of the
1044 models examined here, in work subsequent to the simulations for AQMEII4.

1045 With regards to wet sulphur deposition, Figure 16(a) and Table 6 shows a tendency of most models
1046 towards negative biases for total *daily* wet S deposition. However, this negative bias is much less
1047 pronounced or even positive in comparison to the *weekly* wet S deposition data. Other metrics of model
1048 performance differed sharply between the two wet deposition observation datasets for some metrics, with
1049 the weekly wet SO₄²⁻ deposition data comparison having higher MGE, NMGE, and RMSE values than the
1050 daily wet SO₄²⁻ deposition data comparison. The overall tendency of the performance was similar for
1051 both datasets, with the CMAQ models having the best scores for metrics other than mean bias. We note
1052 that the daily and weekly NA wet deposition values correspond to monitoring networks in two different
1053 locations (see Figure S17(a)). The daily values are from the Canadian CAPMoN network (stations in the
1054 common AQMEII4 domain are located mostly in south-eastern Canada), while the weekly data from the
1055 US NADP network are distributed throughout the USA. The differences in model performance may thus
1056 reflect regional differences in predicted meteorological and/or emissions fields.

1057 One possible cause for the negative biases in wet deposition common to most models could be
1058 underestimates in the amount of model-predicted precipitation, which in turn would reduce the wet flux.
1059 The net precipitation totals converted to liquid water for the eight NA models and observations are shown
1060 in Figure SI10, for both daily (CAPMoN) and weekly(NADP) monthly averages. While the monthly
1061 averages of daily precipitation (Figure SI10(b)) suggest a tendency towards negative biases in the summer
1062 months for some models, the time series of the precipitation biases does not follow that of the wet
1063 sulphate deposition biases (for example, the difference relative to wet sulphate observations in Figure
1064 06(a) remains relatively constant for CMAQ-M3Dry and CMAQ-STAGE, while the predicted
1065 precipitation difference relative to observations for the same models in Figure SI10(a) shows more
1066 negative biases in the summer than wintertime. Model total precipitation biases thus do not appear to be a
1067 major contributing factor to the sulphur flux biases found in this work T.

1068 We also note the potential for the lower magnitude biases in the daily wet wet SO₄²⁻ evaluation,
1069 compared to the weekly evaluation, to be the result of the region represented by the two monitoring



1070 networks. Figure SI7 shows that the daily data are derived from a smaller geographic area than the
1071 weekly data, hence regional performance differences may be affecting the two evaluation results.

1072 *Summary, North American S Deposition variability*

1073 Sulphur deposition results from a complex balance between SO₂ oxidation, particulate sulphate formation,
1074 scavenging and release of particles within clouds, in addition to the processes governing deposition of
1075 each of the components. The largest contributing pathways to North American sulphur deposition, in
1076 descending order of importance, were wet deposition (SO₄²⁻ + HSO₃⁻), particulate sulphate dry deposition,
1077 and dry SO₂(g) deposition in the reduced ensemble of model runs. The largest contributors to model-to-
1078 model variability in sulphur deposition, in descending order of importance, were particulate sulphate dry
1079 deposition, wet deposition (SO₄²⁻ + HSO₃⁻), and dry SO₂(g) deposition.

1080 CMAQ-M3Dry, CMAQ-STAGE, and GEM-MACH (Ops) had both the highest levels of wet deposition
1081 and also the best scores relative to wet deposition observations. Models with higher PM_{2.5} sulphate
1082 positive biases relative to observations also had stronger negative biases for wet sulphate deposition,
1083 indicating that the magnitude of particle scavenging into hydrometeors may play a role in both biases in
1084 the models. Comparisons between {GEM-MACH (Base), GEM-MACH (Zhang)} and {GEM-MACH
1085 (Ops)} provide some evidence for this effect. WRF-Chem (UPM) and WRF-Chem (UCAR) have very
1086 low particulate sulphate deposition fluxes relative to the other models, and substantial positive biases in
1087 PM_{2.5} sulphate and negative biases in wet sulphate deposition, relative to observations, likely related to
1088 insufficient wet scavenging of sulphate particles into hydrometeors (Ryu and Min, 2022)

1089 *3.2.2 Causes of N Deposition Variability in North America Domain Simulations*

1090 The common grid spatial average and percent contribution of each of the species contributing to total
1091 annual N deposition for 2016 are given in Table 7. The columns in the Table are arranged in descending
1092 order from left to right of contribution to the reduced ensemble total nitrogen deposition for each
1093 contributing chemical (“Red. Ens. Avg” row). The impact of variability on the model deposition from
1094 each component for each model is once again shown as the standard deviation across the models used for
1095 the reduced ensemble (“Red. Ens. Std. Dev” row). From the standard deviation row, it can be seen that
1096 the variation (standard deviation) between models for the contributions towards total N deposition are
1097 driven, in descending order, by particle ammonium (DAM column, where the standard deviation for
1098 particle ammonium deposition is larger than the reduced ensemble mean value), followed by wet
1099 ammonium ion (WNH₄), wet nitrate ion (WNO₃), dry HNO₃ (DHNO₃), dry particle nitrate (DNI), dry
1100 NO₂ (DNO₂), dry ammonia gas (DNH₃), with the remaining species contributing a small percentage of
1101 the total variability. Both the particle ammonium and wet ammonium variability between the models is
1102 largely driven by the GEM-MACH group of models, which have average dry particle ammonium and wet
1103 ammonium fluxes which are respectively 17.4x and 1.76x higher than the other models

1104 We next evaluate the models’ nitrogen performance using the available concentration and wet deposition
1105 flux data to determine the impact of the parameterization differences on model performance, and hence
1106 identify which components in which models might be improved.

1107

1108



1109 Table 7. Contributions of N species towards total deposition ($\text{eq ha}^{-1} \text{yr}^{-1}$) and percent of total N deposited, over the
 1110 common AQMEII4 NA grid, arranged in descending order of importance to the reduced ensemble average. WNH4:
 1111 wet deposition of $\text{NH}_4^+(\text{aq})$. DHNO3: dry deposition of $\text{HNO}_3(\text{g})$. WNO3: wet deposition of $\text{NO}_3^-(\text{aq})$. DAM: dry
 1112 deposition of particulate ammonium. DNH3: dry deposition of $\text{NH}_3(\text{g})$. DNI: dry deposition of particulate nitrate.
 1113 DNO2: dry deposition of $\text{NO}_2(\text{g})$. DPAN: dry deposition of peroxyacetyl nitrate gas. DRN3: dry deposition of
 1114 gaseous organic nitrate gases. DN2O5: dry deposition of $\text{N}_2\text{O}_5(\text{g})$. DHNO4: dry deposition of pemitric acid gas.
 1115 DNO: dry deposition of $\text{NO}(\text{g})$. WRF-Chem (IASS) did not report dry particle fluxes. The GEM-MACH
 1116 models and WRF-CHEM(UPM) do not include dry deposition of $\text{N}_2\text{O}_5(\text{g})$, and the GEM-MACH models
 1117 do not dry deposit $\text{HNO}_4(\text{g})$.

Average ($\text{eq ha}^{-1} \text{yr}^{-1}$)										
Species	Model									
	CMAQ-M3Dry	CMAQ-STAGE	WRF-Chem (IASS)	GEM-MACH (Base)	GEM-MACH (Zhang)	GEM-MACH (Ops)	WRF-Chem (UPM)	WRF-CHEM (UCAR)	Red. Ens Avg	Red. Ens. Std Dev
WNH4	51	60.4	0.2	129	129	114.2	64.3	29.4	82.5	37.7
DHNO3	52.5	51.9	0	66.9	56.2	62.4	75.1	46.8	58.8	9.1
WNO3	65.6	66.9	0.2	45	51.3	71.9	73.1	33.6	58.2	14
DAM	8.5	8.4	nd	98.5	100.7	82.6	2.7	2	43.3	44.2
DNH3	33.2	29.5	36.3	26.9	26.6	40	40.3	47.2	34.8	7.3
DNI	18.3	18.9	nd	26.8	32.7	19	7.6	7.1	18.6	8.6
DNO2	7.9	7.3	7.7	23.8	21.9	26.7	10.9	10.8	15.6	7.6
DPAN	4.9	4.7	2	7.7	7.4	10	2.7	2	5.6	2.7
DRN3	6.6	4.9	0.4	1.8	2.4	3.1	0.7	3.1	3.2	1.8
DN2O5	1.2	1.1	2.2	nd	nd	nd	nd	nd	1.2	0.1
DHNO4	0.4	0.1	0	nd	nd	nd	0.8	0.4	0.3	0.1
DNO	0.5	0.5	0	0.1	1.2	0.2	0	0	0.4	0.4
Total N	250.7	254.7	49	426.5	429.4	430	278.2	182.4	321.7	96.5
Percent Contribution										
Species	Model									
	CMAQ-M3Dry	CMAQ-STAGE	WRF-Chem (IASS)	GEM-MACH (Base)	GEM-MACH (Zhang)	GEM-MACH (Ops)	WRF-Chem (UPM)	WRF-CHEM (UCAR)	Red. Ens Avg	Red. Ens. Std Dev
WNH4	20.4	23.7	0.4	30.2	30	26.5	23.1	16.1	25.6	4.7
DHNO3	21	20.4	0	15.7	13.1	14.5	27	25.7	18.3	5
WNO3	26.2	26.3	0.3	10.6	11.9	16.7	26.3	18.4	18.1	6.4
DAM	3.4	3.3	nd	23.1	23.5	19.2	1	1.1	13.5	9.9
DNH3	13.2	11.6	74.2	6.3	6.2	9.3	14.5	25.9	10.8	7.6
DNI	7.3	7.4	nd	6.3	7.6	4.4	2.7	3.9	5.8	1.8
DNO2	3.2	2.9	15.8	5.6	5.1	6.2	3.9	5.9	4.9	1.3
DPAN	1.9	1.9	4.1	1.8	1.7	2.3	1	1.1	1.7	0.5
DRN3	2.6	1.9	0.7	0.4	0.6	0.7	0.2	1.7	1	0.8
DN2O5	0.5	0.4	4.4	nd	nd	nd	nd	nd	0.4	0
DHNO4	0.2	0	0	nd	nd	nd	0.3	0.2	0.1	0.1
DNO	0.2	0.2	0.1	0	0.3	0	0	0	0.1	0.1
WNH4	20.4	23.7	0.4	30.2	30	26.5	23.1	16.1	25.6	4.7

1118



1119 *Dry deposition of particle ammonium*

1120 The largest source of variability between North America models' total N predictions resides in the dry
1121 particle ammonium deposition fluxes, with Table 7 showing that the standard deviation of this deposition
1122 flux across models was essentially as large as the reduced ensemble average. Particle dry ammonium
1123 deposition contributes a disproportionately high contribution to total N *variability* across the North
1124 American ensemble, despite the magnitude of the ensemble average particle ammonium dry deposition
1125 flux being less than the deposition of wet ammonium ion, dry nitric acid gas, or wet nitrate ion,

1126 Figure 17 compares the monthly average PM_{2.5} ammonium concentrations with observations (station
1127 locations appear in Figure S7(b)), and Table 8 provides detailed statistics. From the latter, CMAQ-
1128 M3Dry and CMAQ-STAGE have the best overall performance for particulate ammonium, and GEM-
1129 MACH (Base), GEM-MACH (Zhang) and GEM-MACH (Ops) have the worst performance by the
1130 statistical measures used here. This latter group of models also have the largest magnitude of positive
1131 biases relative to observed PM_{2.5} ammonium concentrations, while the CMAQ implementations have the
1132 negative biases, and the remaining models have smaller magnitude positive biases. Figure 17 shows that
1133 CMAQ-M3Dry, CMAQ-STAGE, WRF-Chem (IASS) and to a lesser extent WRF-Chem (UPM) have a
1134 greater seasonal variability in model particle ammonium (blue line) than observed (red line), with the
1135 difference between summer and winter (months 1 and 12 versus months 5 through 9) being higher in the
1136 models than in observations.

1137 The GEM-MACH contributions to model N variability in critical load exceedances are thus linked to poor
1138 model performance for PM_{2.5} ammonium. This poor performance is likely due to two factors, which can
1139 be deduced from comparing the process representations implemented in the models (section 2.2).

1140 The first factor, which differentiates GEM-MACH (Base), GEM-MACH (Zhang) and GEM-MACH
1141 (Ops) from the other ensemble members relates to how inorganic aerosol thermodynamic partitioning
1142 chemistry has been implemented: while all this process representation in the models of the ensemble is
1143 derived from the ISORROPIA module (Nenes *et al.*, 1998; Fountoukis *et al.*, 2007), the GEM-MACH
1144 implementations in AQMEII-4 employ a partial speciation of SO₄²⁻, NH₄⁺ and NO₃⁻ (Makar *et al.*, 2003),
1145 and do not include the reactions involving particulate base cations (Ca²⁺, Mg²⁺, Na⁺, K⁺). The other
1146 models in the ensemble do include these additional reactions. In the absence of base cation chemistry, the
1147 formation of particle ammonium will be controlled by the availability of ammonia gas in excess of that
1148 required to charge balance particulate sulphate, as well as by the availability of nitric acid gas. In the
1149 presence of base cations, nitric acid gas will preferentially associate with base cations rather than
1150 ammonia, leaving less HNO₃ available for particle ammonium nitrate formation. Several observational
1151 studies have shown that when base cations are present, their peak mass occurs in the coarse particle size
1152 mode (> 2.5 μm diameter), where they will have higher deposition velocities (e.g. inland, agricultural dust
1153 sources, Makar *et al.*, 1998; ocean sources of sea-salt, Anlauf *et al.*, 2006). Base cation inorganic
1154 heterogeneous chemistry thus provides a competing pathway for uptake of nitrate into particles, and when
1155 present, will also reduce the amount of NH₃ that may be taken up by particles, especially in the fine mode.
1156 The positive bias of PM_{2.5} ammonium in Figure 17 for GEM-MACH relative to the other models likely
1157 represents the impact of simplified inorganic aerosol chemistry.

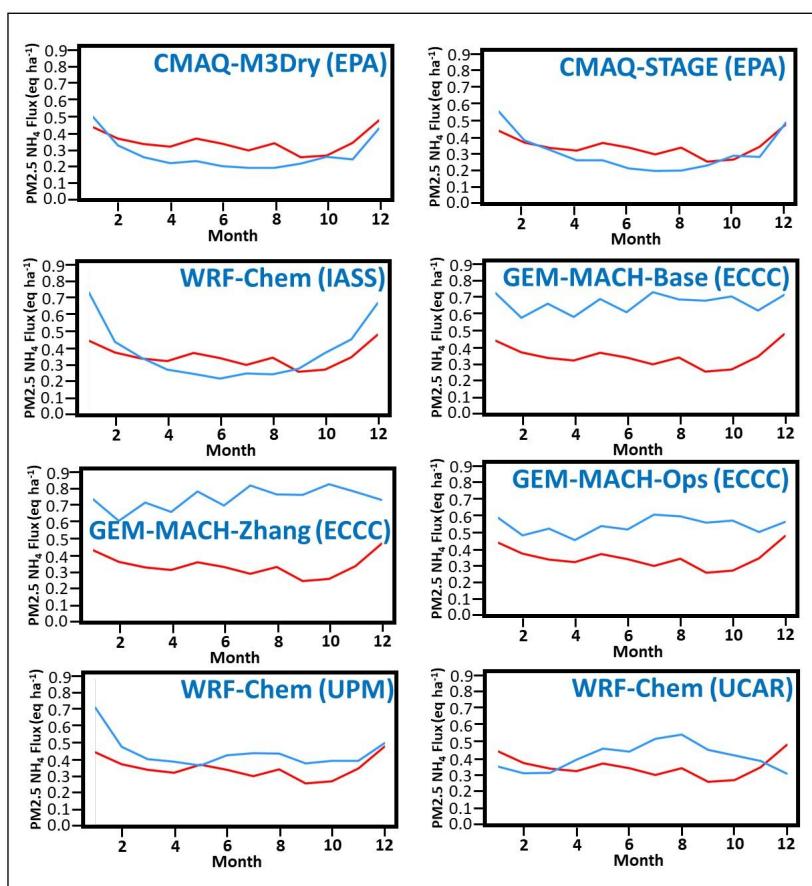
1158 The second factor influencing the GEM-MACH models positive particulate ammonium biases may be
1159 reflected in the biases for GEM-MACH (Base) and GEM-MACH (Zhang), which are 50% to a factor of
1160 two, respectively, higher than that of GEM-MACH (Ops): that is, an additional source of bias resides in
1161 the former two model implementations that is not present in the latter implementation. The likely source
1162 of this additional bias is their use of Emerson *et al.* (2020) particle deposition velocities in these



1163 implementations, in the absence of enhanced wet scavenging of aerosols, as discussed above for PM_{2.5}
 1164 sulphate, and described in Ryu and Min (2022) and Ghahreman *et al.* (2024). Ryu and Min (2022)
 1165 showed that the use of the updated particle deposition velocity as per Emerson *et al.* (2020), when
 1166 implemented in the absence of concurrent multiphase wet scavenging updates led to positive biases in
 1167 PM_{2.5} concentrations in the WRF-Chem model.

1168 We note that the manner in which inorganic heterogeneous chemistry is simulated also differs between the
 1169 models. CMAQ-M3Dry and CMAQ-STAGE calculate local equilibrium concentrations at different
 1170 modes of the size distribution, and WRF-Chem (UPM) and WRF-Chem (UCAR) also calculate the
 1171 equilibrium with respect to specific size bins, while GEM-MACH (Base), GEM-MACH (Zhang) and
 1172 GEM-MACH (Ops) carry out a single bulk calculation across all size bins. The use of a bulk calculation
 1173 is a third simplification for the latter group of models, and may also affect the particulate ammonium
 1174 performance of these models.

1175 Figure 17. PM_{2.5} Ammonium compared to observations, North American Model Ensemble, 2016. Red line:
 1176 monthly observed average. Blue line: monthly model average.



1177

1178



1179 Table 8. Model Performance Metrics for PM_{2.5} ammonium, wet deposition of ammonium ion, wet
 1180 deposition of nitrate ion, AQMEII4 North American domain, 2016. Bold-face letters show the highest
 1181 scoring model.

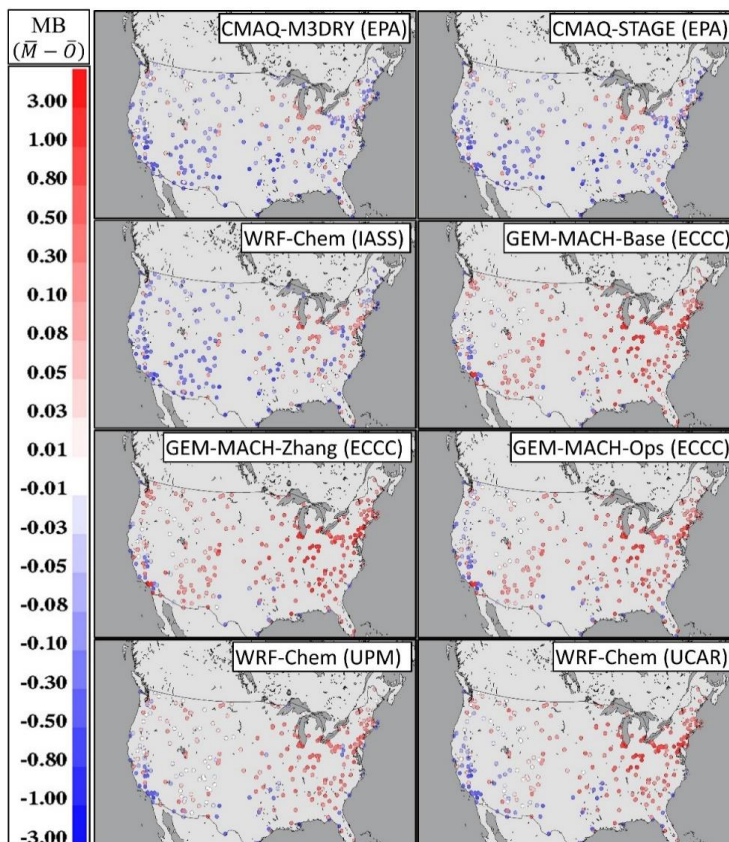
PM _{2.5} NH ₄ (units µg m ⁻³ , where applicable)								
Performance Measure	CMAQ-M3Dry	CMAQ-STAGE	WRF-Chem (IASS)	GEM-MACH (Base)	GEM-MACH (Zhang)	GEM-MACH (Ops)	WRF-Chem (UPM)	WRF-Chem (UCAR)
FAC2	0.48	0.49	0.31	0.45	0.42	0.46	0.51	0.46
MB	-0.07	-0.04	0.03	0.32	0.41	0.20	0.10	0.06
MGE	0.23	0.24	0.33	0.45	0.52	0.38	0.31	0.31
NMGE	0.68	0.70	0.96	1.31	1.53	1.10	0.91	0.91
RMSE	0.59	0.60	0.75	0.81	0.93	0.75	0.69	0.69
R	0.37	0.37	0.30	0.33	0.32	0.32	0.30	0.23
COE	0.19	0.17	-0.13	-0.55	-0.80	-0.30	-0.08	-0.08
IOA	0.60	0.58	0.43	0.23	0.10	0.35	0.46	0.46
Daily Total Wet NH ₄ Deposition (units eq ha ⁻¹ d ⁻¹ , where applicable)								
FAC2	0.26	0.29	0.00	0.39	0.38	0.43	0.28	0.14
MB	-0.49	-0.44	-0.94	-0.01	0.00	-0.10	-0.39	-0.59
MGE	0.67	0.65	0.94	0.76	0.78	0.68	0.71	0.80
NMGE	0.72	0.69	1.00	0.81	0.83	0.73	0.76	0.86
RMSE	1.46	1.43	1.90	1.66	1.71	1.45	1.54	1.73
R	0.55	0.57	0.26	0.52	0.51	0.59	0.49	0.37
COE	0.32	0.34	0.05	0.23	0.21	0.31	0.28	0.19
IOA	0.66	0.67	0.53	0.61	0.61	0.65	0.64	0.59
Weekly Total Wet NH ₄ Deposition (units eq ha ⁻¹ week ⁻¹ , where applicable)								
FAC2	0.28	0.33	0.00	0.41	0.42	0.44	0.31	0.14
MB	-1.51	-1.29	-2.97	0.39	0.38	0.08	-1.19	-2.18
MGE	2.13	2.03	2.97	2.46	2.44	2.18	2.12	2.43
NMGE	0.72	0.68	1.00	0.82	0.82	0.73	0.71	0.82
RMSE	4.29	4.13	5.49	5.06	5.02	4.42	4.25	4.78
R	0.50	0.53	0.29	0.51	0.51	0.54	0.50	0.40
COE	0.25	0.28	-0.05	0.13	0.14	0.23	0.25	0.14
IOA	0.62	0.64	0.47	0.57	0.57	0.62	0.63	0.57
Daily Total Wet NO ₃ Deposition (units eq ha ⁻¹ d ⁻¹ , where applicable)								
FAC2	0.39	0.39	0.00	0.38	0.39	0.49	0.43	0.28
MB	-0.18	-0.16	-0.68	-0.26	-0.19	-0.07	-0.05	-0.34
MGE	0.44	0.44	0.68	0.45	0.46	0.44	0.48	0.52
NMGE	0.65	0.65	1.00	0.66	0.68	0.64	0.71	0.76
RMSE	0.80	0.80	1.16	0.84	0.85	0.83	0.89	0.97
R	0.61	0.62	0.22	0.56	0.56	0.59	0.55	0.44
COE	0.28	0.28	-0.11	0.27	0.25	0.29	0.22	0.15
IOA	0.64	0.64	0.45	0.63	0.63	0.64	0.61	0.58
Weekly Total Wet NO ₃ Deposition (units eq ha ⁻¹ week ⁻¹ , where applicable)								
FAC2	0.50	0.50	0.00	0.42	0.45	0.49	0.43	0.33
MB	-0.10	-0.06	-1.86	-0.64	-0.41	0.06	0.10	-0.87
MGE	1.09	1.09	1.86	1.12	1.12	1.17	1.34	1.26
NMGE	0.58	0.59	1.00	0.60	0.60	0.63	0.72	0.68
RMSE	1.86	1.88	2.93	1.96	1.95	1.93	2.23	2.19
R	0.65	0.65	0.35	0.58	0.58	0.60	0.53	0.48
COE	0.32	0.32	-0.16	0.30	0.30	0.27	0.16	0.21
IOA	0.66	0.66	0.42	0.65	0.65	0.64	0.58	0.61

1182



1183 The spatial distribution of PM_{2.5} ammonia biases was examined in Figure 18, for the month of July, 2016
 1184 (July was chosen due to the expectation that bidirectional fluxes would have a higher impact in the
 1185 summer months). The region with the highest positive biases (dark red circles, Figure 18) are in the same
 1186 station locations for all models, in the agricultural region to south of the Great Lakes. Positive PM_{2.5}
 1187 ammonium MB also occur near urban regions in western USA (Seattle/Tacoma, Yakima, Portland,
 1188 Sacramento, San Jose, Boise, Butte, Helena, Denver, Boulder, and Albuquerque) and at one eastern site
 1189 Miami. A re-examination of ammonia gas deposition and emissions parameters and primary particle
 1190 ammonium emissions inventories are recommended for these locations, given that they are likely having a
 1191 large impact on model performance statistics. The CMAQ models and WRF-Chem (IASS) have negative to
 1192 minimal biases along the coastlines and SW USA (regions of sea-spray NaCl and wind-blown base
 1193 cation containing dust, respectively), while WRF-Chem (UPM) and WRF-Chem (UCAR) have small
 1194 negative to positive biases in these regions, and the GEM-MACH models are uniformly biased positive in
 1195 these regions. This provides support to the possibility that the GEM-MACH positive bias in particulate
 1196 ammonium concentrations is due to missing particulate base cation chemistry; the regions where
 1197 particulate base cations would be expected to contribute significantly to total particulate mass are also the
 1198 regions where the GEM-MACH models have positive biases, and the biases in the other model biases are
 1199 not as significant.

1200 Figure 18. Mean Biases, PM_{2.5} NH₄, July, 2016, by station ($\mu\text{g m}^{-3}$). Negative values given in blue, positive biases
 1201 given in red. Note that colour scale is logarithmic.



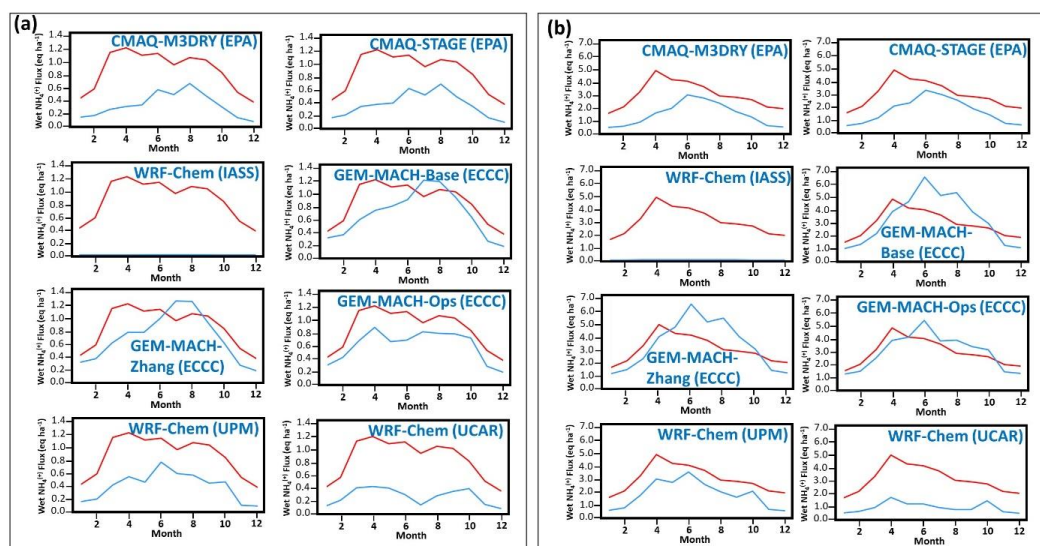
1202



1203 *Wet deposition of ammonium and nitrate ions.*

1204 Wet deposition of ammonium ion is the largest contributor to the North America reduced ensemble N_{dep} ,
 1205 and the second largest contributor to model-to-model variability in N deposition (Table 7). Wet
 1206 deposition of nitrate ion is the third largest contributor to both the NA ensemble total N deposition and
 1207 model-to-model variability in N deposition. Time series of the monthly averages of observed and
 1208 modelled daily (CAPMoN) and weekly (NADP) wet NH_4^+ deposition fluxes are shown in Figure 19. The
 1209 monthly mean of modelled daily values (Figure 19(a)) are generally biased negative, with the exceptions
 1210 of the months of July and August for GEM-MACH (Base) and GEM-MACH (Zhang). The observed
 1211 maximum in NH_4^+ wet deposition occurs in April (Figure 19(a), red line, month 4) – this seasonal
 1212 variation is captured only by GEM-MACH (Ops) and WRF-Chem (UCAR), with the other models
 1213 predicting peak deposition in between June through August. The monthly average of the weekly wet
 1214 NH_4^+ deposition fluxes (Figure 19(b)) shows a similar pattern, with the observed values (red lines, Figure
 1215 19(b)) peaking in April, and all of the models except for WRF-Chem (UCAR) peaking in June. As was
 1216 the case for wet sulphate deposition, the observed seasonal variation is apparently not connected with
 1217 biases in precipitation predictions (see Figure S10(a,b), supplemental information), with the possible
 1218 exception of WRF-Chem (UCAR), for which total precipitation is biased substantially negative
 1219 throughout the year.

1220 Figure 19. Time series of monthly average observed (red line) and modelled (blue line) wet ammonium deposition
 1221 fluxes, for (a) Daily CAPMoN data ($eq\ ha^{-1}\ day^{-1}$), and (b) Weekly NADP data ($eq\ ha^{-1}\ week^{-1}$).



1222

1223 As noted above, the models taking part in this ensemble did not make use of multiphase hydrometeor
 1224 scavenging in precipitation. The maximum wet NH_4^+ deposition negative bias in April featuring for
 1225 several models may reflect the absence of this level of detail in hydrometeor scavenging, with the absence
 1226 of snow scavenging potentially impacting early spring deposition. We note that the weekly and daily
 1227 monitoring networks cover different geographical regions, hence the differences in model performance
 1228 relative to the two observation datasets (compare the CAPMoN and NADP station locations in yellow and
 1229 green circles respectively, Figure S7(a).



1230 The mean biases in average daily and weekly wet NH_4^+ deposition for the month of April are shown in
1231 Figure 20. WRF-Chem (IASS), CMAQ-M3Dry, and CMAQ-STAGE have predominantly negative biases
1232 throughout the region, WRF-Chem (UCAR) and WRF-Chem (UPM) have a few stations with more
1233 positive biases, and the GEM-MACH models have both positive and negative biases throughout the
1234 domain. Insight into the differences in model performance can be gained through reviewing the manner
1235 in which each model parameterizes aerosol activation and scavenging:

- 1236 (1) GEM-MACH (Base), GEM-MACH (Zhang), GEM-MACH (Ops), WRF-Chem (UPM), and
1237 WRF-Chem (UCAR) make use of the aerosol activation scheme of Abdul-Razzak and Ghan
1238 (2000), and the Slinn (1984) approach to aerosol scavenging.
- 1239 (2) In GEM-MACH (Ops), the aerosol activation and scavenging schemes are decoupled from
1240 meteorological feedbacks, while GEM-MACH (Base), GEM-MACH (Zhang), WRF-Chem
1241 (UPM) and WRF-Chem (UCAR) are “aerosol-aware”/full feedback models incorporating
1242 parameterizations for the aerosol direct and indirect effects. The latter will result in cloud
1243 formation from model-produced aerosols acting as cloud-condensation nuclei; clouds are more
1244 likely to form where aerosol concentrations are high (and thus more likely to scavenge aerosols
1245 below the clouds as well), compared to offline models. Very high aerosol concentrations may
1246 also reduce cloud droplet size and cloud to precipitation conversion, potentially making clouds
1247 more persistent, while reducing precipitation.
- 1248 (3) WRF-Chem (IASS) also makes use of aerosol direct and indirect effect feedbacks, but employs
1249 the approach of Chapman *et al.* (2009) for aerosol scavenging.
- 1250 (4) CMAQ-M3Dry and CMAQ-STAGE are off-line models (no feedbacks between aerosols, cloud
1251 formation and radiative transfer takes place), where interstitial and nucleation aerosol scavenging
1252 by cloud droplets is modelled following Binkowski and Roselle (2003), and the wet deposition
1253 rate is a simple parameterization dependent on the cloud total liquid water content, cloud
1254 thickness, and cloud precipitation rate (Fahey *et al.*, 2017).

1255 The Slinn (1984) aerosol scavenging approach makes use of different observation-based aerosol
1256 collection efficiency formulae for rain and snow, respectively, where temperature dependence in the
1257 collection efficiency such as a 0 C may be used to distinguish between liquid and solid hydrometeor
1258 collection efficiencies. Subsequent to the AQMEII-4 simulations carried out here, parameterizations that
1259 utilize multiphase precipitation data with multiple hydrometeor classes, such as that of Wang *et al.*
1260 (2014), have been tested within the modelling framework of GEM-MACH (Ghahreman *et al.*, 2024).
1261 Similarly, Ryu and Min (2022) describes the impact of multiphase hydrometeor scavenging as
1262 implemented in the WRF-Chem modelling framework. These tests resulted in significant improvements
1263 in particulate concentrations and wet deposition compared to previous implementations employing the
1264 approach of Slinn (1984). The approach for scavenging in Binkowski and Roselle (2003) assumes
1265 scavenging only occurs to cloud droplets; snow scavenging is not considered. However, snow scavenging
1266 at higher precipitation rates is known to be one to two orders of magnitude more efficient than scavenging
1267 by rain. Hence the use of the (Slinn (1984) parameterization instead of multiphase hydrometeor
1268 scavenging and the; Wang, (2014) parameterization in GEM-MACH, and the omission of multiphase
1269 hydrometeor scavenging in CMAQ, may account for the springtime bias in all models noted here.

1270 The causes for the differences in wet deposition of NH_4 between WRF-Chem (IASS), WRF-Chem (UPM)
1271 and WRF-Chem (UCAR) may result from the use of the Chapman *et al.* (2009) wet scavenging approach
1272 in the first model, and the implementation of Abdul-Razzak and Ghan (2000), and the Slinn (1984)
1273 approaches in the latter two models. All three models make use of the Morrison Two-Moment cloud
1274 microphysics scheme and (Morrison *et al.*, 2009), though WRF-Chem (IASS and WRF-Chem (UPM)



1275 differ from WRF-Chem (UCAR) in the parameterization of convective clouds (See Table 2). Differences
1276 in aerosol scavenging implementations may account for some of the differences in wet ammonium
1277 deposition between these models, as may the manner in which convective clouds identify cloud
1278 condensation nuclei from aerosol size distribution and speciation within their convective
1279 parameterizations.

1280 Wet nitrate ion deposition is the third largest source of N deposition in the North American ensemble as
1281 well as the third largest source of model-to-model variability (Table 7). CMAQ-M3Dry, CMAQ-STAGE
1282 and GEM-MACH (Ops) have the best performance scores for wet nitrate deposition (Table 8). GEM-
1283 MACH (Base) and GEM-MACH (Zhang) have larger magnitude and more negative biases than GEM-
1284 MACH (Ops), despite all three models making use of the same modelling framework. The only
1285 difference between GEM-MACH (Base) and GEM-MACH (Zhang) is the gas-phase dry deposition
1286 algorithm employed (see Table 3). The increase in wet deposition negative bias magnitude going from
1287 GEM-MACH (Zhang) to GEM-MACH (Base) in Table 8 (from -0.19 to -0.26 eq ha⁻¹ d⁻¹ for daily
1288 CAPMoN data, and from -0.41 to -0.64 for weekly NADP data) is therefore attributable to gas-phase
1289 deposition differences. This is also reflected in the HNO₃ dry deposition flux for the two models in Table
1290 7, with the deposition flux for GEM-MACH (Base) at 66.9 eq ha⁻¹ yr⁻¹ being 19% higher than the GEM-
1291 MACH (Zhang) value of 56.2 eq ha⁻¹ yr⁻¹.

1292 The remainder of the difference in wet nitrate deposition bias between (GEM-MACH (Base, Zhang) and
1293 GEM-MACH (Ops) must be due to other factors in the model configuration as described in Table 3.
1294 Based on the PM_{2.5} sulphate and PM_{2.5} nitrate evaluations (Table 6, Table 8), as well as the work of
1295 Ghahreman *et al.* (2024) and Ryu and Min (2022), we believe that the cause of the additional wet nitrate
1296 negative bias resides in the use of the new particle deposition velocity algorithm in the absence of a
1297 simultaneous update in the wet deposition algorithm to make use of multiphase hydrometeor scavenging
1298 of aerosols. For example, the particulate matter scavenging coefficients for snow are one to two orders of
1299 magnitude more efficient than for rain – including snow scavenging (which may occur at higher
1300 elevations even in the summer) will lead to greater uptake of particles (Ghahreman *et al.*, 2024). The
1301 Emerson *et al.* 2020 parameterization will lead to less particle deposition in sub-micrometer particle sizes
1302 (and hence would otherwise increase PM_{2.5} concentrations – the increased scavenging associated with
1303 multiphase hydrometeors will offset this effect.

1304 *Dry Deposition of HNO₃*

1305 Dry deposition of HNO₃ is the 2nd largest source of N_{dep} in the reduced ensemble, and the 4th largest
1306 source of model-to-model variability.

1307 The spatial variation of the annual sum of the effective deposition fluxes for HNO₃ dry deposition are
1308 shown in Figure S11, Figure S12, Figure S13 and Figure S14, representing the mass of HNO₃ transferred
1309 to the surface via the cuticle, soil, stomatal and lower canopy pathways respectively, and are summarized
1310 as common grid totals in Figure 21. Effective fluxes build on the concept of effective conductance: the
1311 product of the hourly deposition flux with the ratio of specific pathway conductance to total deposition
1312 velocity, for each of the four pathways (Galmarini *et al.*, 2021). The Figures thus depict the contributions
1313 of each pathway towards the HNO₃ dry deposition mass flux for each model¹. Effective fluxes
1314 incorporate changes in the flux resulting from changes in chemical concentration associated with factors
1315 in addition to deposition. However, comparison of the effective flux values of Figure 21 to effective

¹ Note that the CMAQ-M3dry and CMAQ-STAGE models incorporate the lower canopy pathway into the soil pathway; the lower canopy effects are not *absent* in these models, but form part of the soil pathway, and hence are reported here as part of the soil pathway.



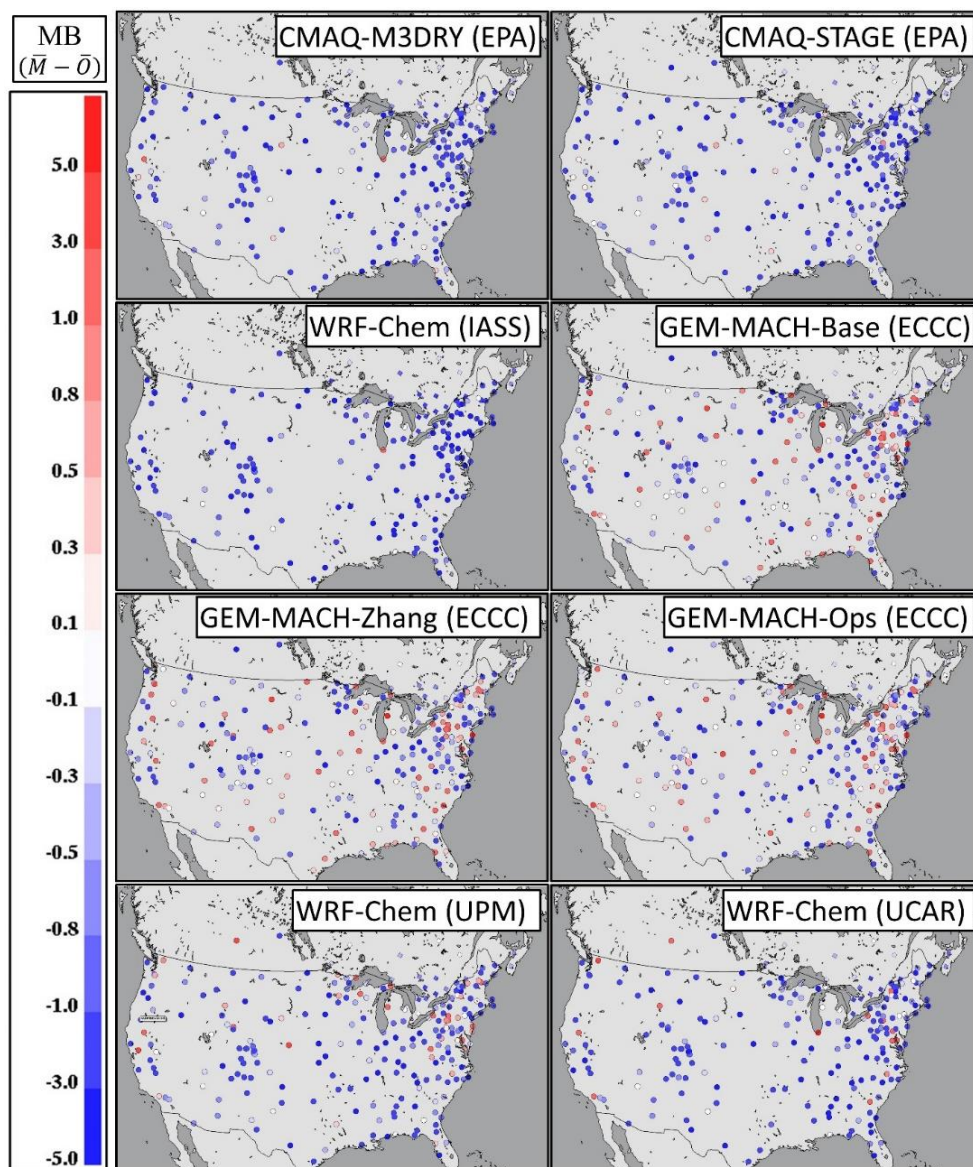
1316 conductances (not shown) has a similar pattern, implying that the deposition velocity is the dominating
1317 factor in the HNO₃ deposition flux. The HNO₃ mass flux is dominated by the cuticle pathway (Figures
1318 S11, 21), followed by the soil pathway (Figures S12, 21). All models show a similar pattern in HNO₃
1319 annual cuticle flux (largest fluxes in the south-eastern USA, lowest fluxes over the western mountain
1320 ranges and the Canadian boreal forest), though the magnitudes of the fluxes vary, with WRF-Chem
1321 (UPM) having the highest flux, GEM-MACH (Zhang) showing much lower fluxes for specific land use
1322 types over the western mountains compared to the other models.

1323 The HNO₃ dry deposition velocity parameterizations in the GEM-MACH models depends in part on
1324 deposition pathway parameterizations employing functions of the ozone and sulphur dioxide pathway
1325 values (Makar *et al.*, 2018; Zhang *et al.*, 2003). Other recent AQMEII4 work for ozone dry deposition
1326 using an observation-driven single-point modeling framework (Clifton *et al.*, 2023) found that the ozone
1327 deposition velocity for GEM-MACH (Base) has positive biases in the summer months (average across 8
1328 sites +73%), negative in the winter months (8 site average of -33%), while GEM-MACH (Zhang) has
1329 smaller summer biases (+3%) and high winter biases (+50%). This is consistent with the increase in dry
1330 HNO₃ deposition flux going from GEM-MACH (Zhang) to GEM-MACH (Base) though HNO also
1331 deposits via dissociation (sulphur dioxide pathway); not all of the observed effects can be attributed to the
1332 use of O₃ as a proxy in part of the deposition algorithm.. A portion of the increase in the negative bias in
1333 wet nitrate deposition going from GEM-MACH (Zhang) to GEM-MACH (Base) is thus the result of
1334 higher HNO₃ dry deposition removal of the available nitrate which would otherwise be taken up into
1335 clouds.

1336



1337 Figure 20. Model mean biases in wet ammonium deposition for the month of April, 2016, North America (eq ha^{-1}
1338 yr^{-1}). Daily station values of the mean bias (CAPMoN network) shown as diamond symbols, weekly station values
1339 (NADP network) as circles. Positive biases shown in red, negative biases shown in blue; note that colour scale
1340 intervals are logarithmic.

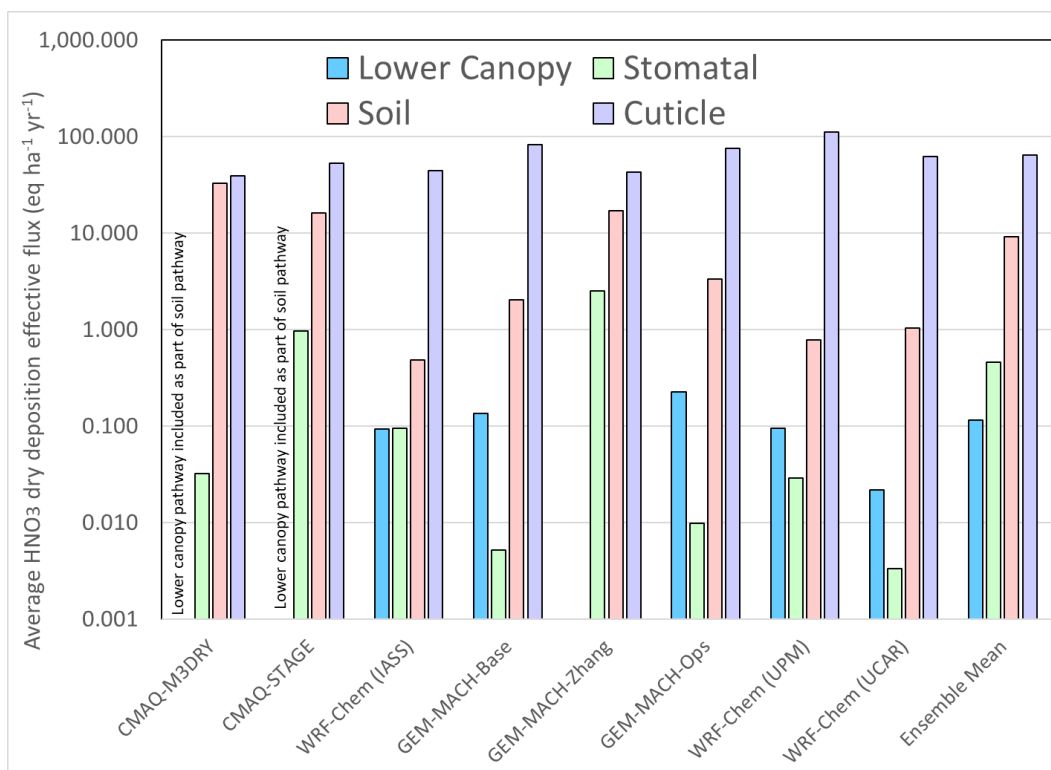


1341

1342



1343 Figure 21. Averages of flux pathway contributions to HNO₃ dry deposition, AQMEII4 common NA grid,
1344 2016 (eq ha⁻¹ yr⁻¹).



1345

1346 *NH₃ and the role of bidirectional flux algorithms*

1347 NH₃ deposition fluxes were the fifth largest driver of ensemble nitrogen deposition, and the 7th largest
1348 driver of N_{dep} variability in North America. Two different observation datasets for the year 2016 were
1349 used to evaluate model NH₃ concentration performance, Cross-track Infrared Sounding (CrIS) satellite
1350 retrievals of NH₃ (see SI for retrieval procedure and references) and AMoN (Chen *et al.*, 2014; AMoN,
1351 2024) surface monitoring network observations (see SI Figure S8(b) for AMoN measurement locations).
1352 The two datasets evaluate model NH₃ performance in different ways. The CrIS observations (and model
1353 values extracted for evaluation) correspond to the specific time-of-day of the satellite overpass, for the
1354 polar orbiting platform upon which the CrIS instrument is based. The evaluation against CrIS data is thus
1355 a measure of the model performance at early afternoon local time. The AMoN observations in contrast
1356 are two-week integrated average concentrations; the AMoN comparison evaluates average model
1357 performance on this integrated time scale, and hence includes into that average diurnal variations in NH₃
1358 concentrations not available in the CrIS observations.

1359 The evaluation of the models' NH₃ against CrIS observations at overpass time is shown in Table 9 and
1360 Figure 22. The general trend for the models is one of negative biases in NH₃ concentrations. CMAQ-
1361 M3Dry and CMAQ-STAGE, have the largest negative NH₃ biases, lowest FAC2, highest MGE, lowest R,
1362 lowest COE and lowest IOA scores in Table 9. This suggests that the magnitude of the fluxes and/or the
1363 balance between positive (downward; deposition) and negative (upward; emission) fluxes for CMAQ-



1364 M3Dry and CMAQ-STAGE are the cause of the model’s relatively poor performance for NH₃. GEM-
 1365 MACH (Base) and GEM-MACH (Zhang) have the smallest (and positive) biases compared to the other
 1366 models, and these two models as well as WRF-Chem (UPM) and WRF-Chem (UCAR) have the best
 1367 overall scores for NH₃ against satellite data.

1368 The satellite data comparison of Figure 22 also shows some significant differences between observed
 1369 ammonia and all models’ predicted ammonia, particularly over water bodies (oceans, Great Lakes), with
 1370 observed NH₃ in the range 1-3 ppbv in the Atlantic and near Baja California, while the models all show
 1371 NH₃ over the oceans always below 0.3 to 0.5 ppbv, and decreasing with increasing distance from the
 1372 shoreline. All models reach 0.0 – 0.01 ppbv at the greatest distances from the shoreline, while the satellite
 1373 observations are above 0.5 ppbv (lower detection limit ~0.3 ppbv) throughout the common AQMEII4
 1374 domain.

1375 NH₃ emissions from natural sources has been a source of ongoing interest in the global modelling
 1376 community due to its properties as a greenhouse gas. Paulot *et al.* (2015) reviewed estimates of global
 1377 oceanic NH₃ emissions, with a range of 7 – 23 Tg N yr⁻¹ and their own estimate being lower at 2.5 Tg N
 1378 yr⁻¹. Their estimated maps of NH₃ emissions showed relatively lower values on the western shoreline of
 1379 North America (Pacific coast) than on eastern shoreline (Atlantic coast), and high emissions in three out
 1380 of the four oceanic NH₃ flux models tested, in the Gulf of Mexico and along the Gulf stream between
 1381 North America and Europe (their Figure 4). Subsequent simulations of oceanic outgassing (Paulot *et al.*,
 1382 2020) showed oceanic outgassing in the Gulf of Mexico in excess of 0.03 g N m⁻² yr⁻¹ (17.6 eq ha⁻¹ yr⁻¹),
 1383 and between 0.01 and 0.02 g N m⁻² yr⁻¹ (5.9 to 11.8 eq ha⁻¹ yr⁻¹) in the Gulf Stream. The oceanic
 1384 emissions model of Paulot *et al.* (2020) would be relatively straightforward to implement in a regional
 1385 modelling context; our work suggests that a considerable deficit in oceanic NH₃ may be occurring in the
 1386 current regional air-quality models.

1387 The evaluation of the models’ NH₃ against biweekly surface observations at the AMoN sites is shown in
 1388 Table 10, where biweekly values have been used to create annual averages from both model and observed
 1389 values at observation sites. GEM-MACH (Base) and GEM-MACH (Zhang) once again have the lowest
 1390 magnitude (and positive) biases relative to observations, CMAQ-M3Dry and CMAQ-STAGE have the
 1391 most negative biases, though CMAQ-STAGE has the best correlation coefficient score, and WRF-Chem
 1392 (UPM) has the best scores overall aside from mean bias and correlation coefficient.

1393 Table 9. Evaluation of model predictions of NH₃ against retrieved CrIS NH₃ concentrations at overpass time,
 1394 AQMEII4 common NA grid, 2016. Units ppbv where required.

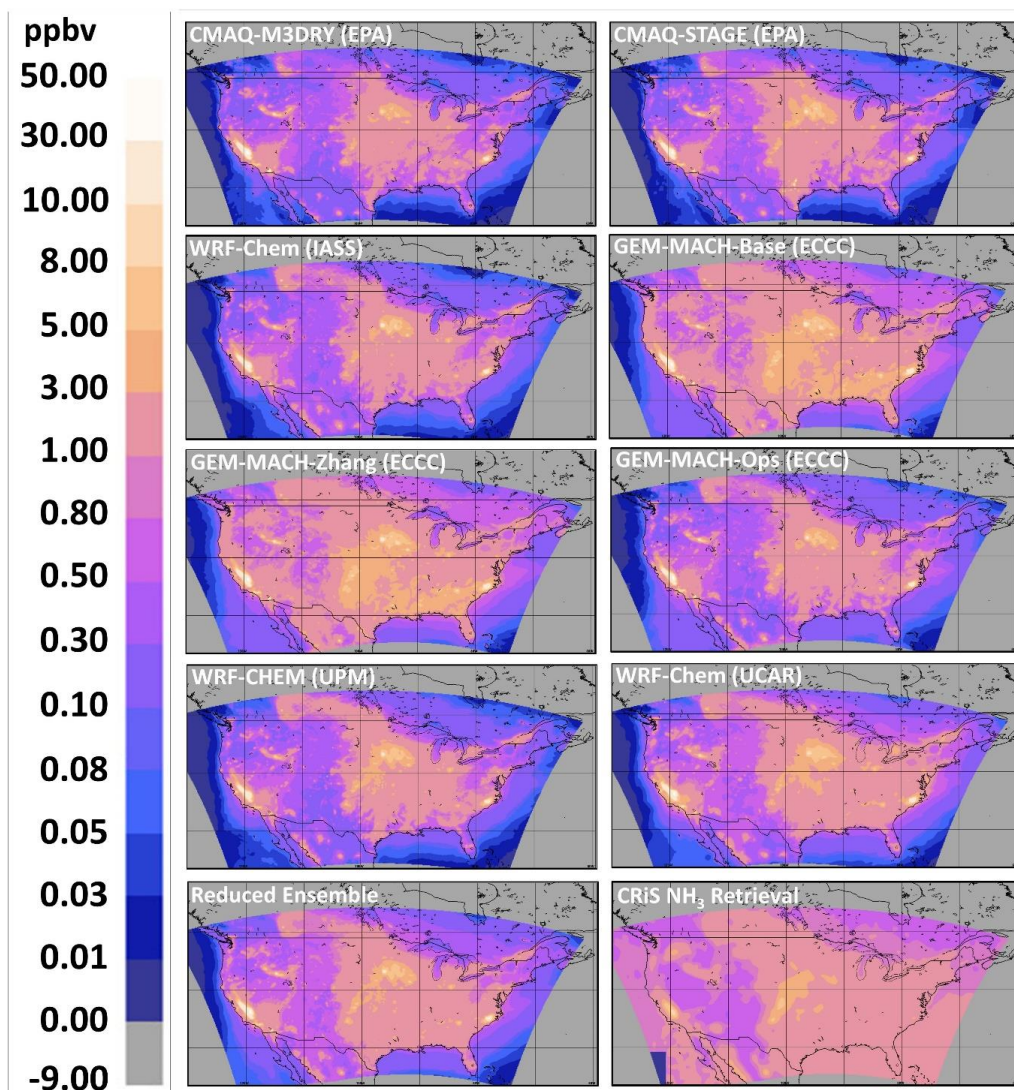
Evaluation Metric	CMAQ-M3Dry	CMAQ-STAGE	GEM-MACH (Base)	GEM-MACH (Zhang)	GEM-MACH (Ops)	WRF-Chem (UPM)	WRF-Chem (UCAR)
FAC2	0.28	0.38	0.68	0.68	0.40	0.38	0.58
MB	-0.68	-0.57	0.09	0.09	-0.54	-0.54	-0.27
MGE	0.83	0.76	0.63	0.63	0.72	0.72	0.61
NMGE	0.64	0.58	0.48	0.48	0.55	0.56	0.47
RMSE	1.16	1.03	1.07	1.06	1.00	0.94	1.00
R	0.66	0.72	0.77	0.78	0.70	0.76	0.74
COE	-0.63	-0.50	-0.24	-0.24	-0.41	-0.43	-0.21
IOA	0.18	0.25	0.38	0.38	0.29	0.29	0.40

1395

1396



1397 Figure 22. Comparison of annual average surface NH_3 concentrations at CrIS overpass times, participating models,
1398 reduced ensemble, and corresponding CrIS observed average NH_3 at overpass time.



1399

1400



1401 Table 10. Evaluation of model predictions of NH₃ against annual average AMoN biweekly NH₃ concentrations
 1402 model-observation pairs, 2016. Units ppbv where required.

Evaluation Metric	CMAQ-M3Dry	CMAQ-STAGE	GEM-MACH (Base)	GEM-MACH (Zhang)	GEM-MACH (Ops)	WRF-Chem (UPM)	WRF-Chem (UCAR)
FAC2	0.66	0.62	0.67	0.67	0.72	0.76	0.66
MB	-0.82	-0.88	0.09	0.02	-0.80	-0.61	0.27
MGE	1.24	1.12	1.21	1.18	1.12	1.08	1.28
NMGE	0.60	0.54	0.59	0.57	0.54	0.52	0.62
RMSE	2.71	2.53	2.72	2.72	2.65	2.57	2.95
R	0.37	0.45	0.39	0.39	0.39	0.40	0.38
COE	0.21	0.29	0.23	0.25	0.29	0.32	0.19
IOA	0.61	0.65	0.61	0.62	0.64	0.66	0.59

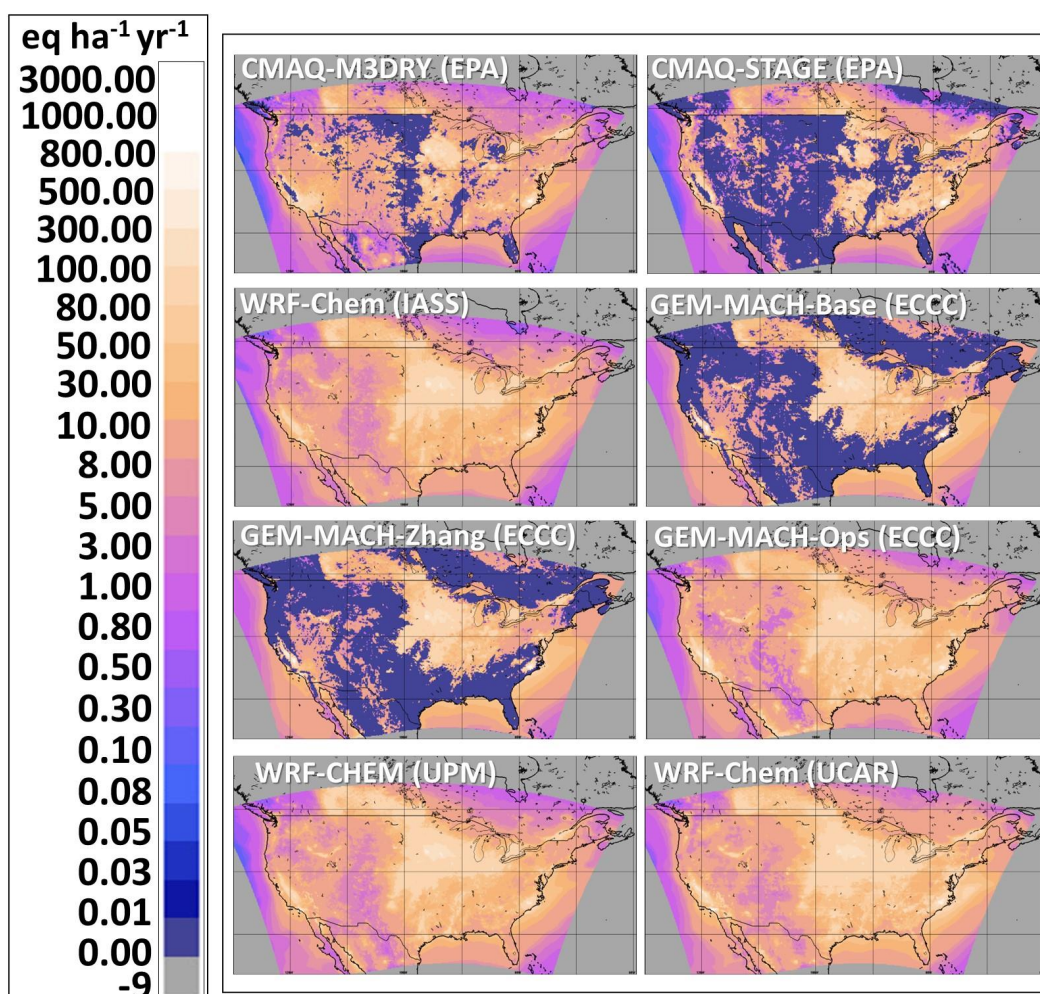
1403

1404 Figure 23 shows the contributions to total N deposition flux from dry deposition of NH₃(g), and the
 1405 difference in overall deposition patterns between the models employing bidirectional NH₃ flux
 1406 parameterizations (CMAQ-M3Dry, CMAQ-STAGE, GEM-MACH (Base), and GEM-MACH (Zhang))
 1407 and the models which do not employ such a parameterization (WRF-Chem (IASS), GEM-MACH (Ops),
 1408 WRF-Chem (UPM), WRF-Chem (UCAR)). The models utilizing bidirectional fluxes have large regions
 1409 where the net downward flux is given as zero in the panels of Figure 23 (dark blue regions, CMAQ-
 1410 M3Dry, CMAQ-STAGE, GEM-MACH-Base, GEM-MACH Zhang models) – these are locations where
 1411 the annual total NH₃ flux is *upward*; net *emissions* of NH₃ when summed over the course of the year. The
 1412 size of these regions differs between CMAQ-M3Dry and CMAQ-STAGE, indicating differences in the
 1413 bidirectional flux parameterizations between these models. GEM-MACH (Base) and GEM-MACH
 1414 (Zhang) also use a bidirectional flux parameterization, which differs from those of CMAQ-M3Dry and
 1415 CMAQ-STAGE, and consequently have relatively similar patterns of net NH₃ dry deposition versus
 1416 emissions. Differences in land-use data as well as country-specific differences in the level of details
 1417 utilized in the bidirectional flux schemes also are resulting in differences between the two modelling
 1418 platforms (e.g. the north-western USA/south-western Canada border shows up as a sharp contrast in the
 1419 CMAQ models NH₃ fluxes that utilize information from EPIC over the US and less detailed information
 1420 outside the US while this differences is much less pronounced in the GEM-MACH models).

1421



1422 Figure 23. 2016 N dry deposition fluxes (eq ha⁻¹ yr⁻¹) for NH₃(g) (eq ha⁻¹ yr⁻¹)



1423

1424

1425 The AQMEII4 diagnostics for NH₃ deposition provide further insight into the causes of the differences
 1426 between the models employing NH₃ bidirectional fluxes. The most generic formula for NH₃ bidirectional
 1427 fluxes is:

1428
$$F_T = \frac{c_a - c_c}{r_{sum}} \quad (13)$$

1429 Where F_T is the net flux c_a is the atmospheric concentration of ammonia gas, and r_{sum} is a sum of
 1430 resistances associated with turbulent eddies and molecular diffusion of gaseous NH₃ across the reference
 1431 height of air and the vegetation canopy. c_c is the canopy compensation point concentrations of
 1432 ammonia gas at the top of the canopy, and may be expressed as a function of the atmospheric
 1433 concentration as well as compensation point concentrations near stomata and the ground (c_s , c_g), and of
 1434 the aerodynamic resistance of ammonia gas (r_a). As can be seen from equation (13), if the atmospheric



1435 concentration is greater than the compensation point concentration, the flux will be positive (downward).
1436 If the atmospheric concentration is less than the compensation point concentration, the flux will be
1437 negative (upward). Galmarini *et al.* (2021, Appendix C) gives the detailed formulae for the terms in
1438 equation (13), for the bidirectional flux models participating in AQMEII4. A comparison of r_a , r_{sum} , c_a , c_c ,
1439 c_g , and c_s may thus provide insight into the differences in the between the predicted NH_3 dry deposition
1440 fluxes for the models employing bidirectional flux parameterizations for the AQMEII4 North American
1441 ensemble. These terms were reported by AQMEII4 participants as the diurnal median (50th percentile) at
1442 each UT hour within each month. The median values for 16UT (noon EDT) for July 2016 are shown in
1443 Figure 24. It is important to note that the median values for a given UT hour may correspond to different
1444 days within a given month. For example, the median values of r_{sum} and r_a at 16 UT in July may not occur
1445 on the same day, and hence the median value of r_{sum} will not necessarily be greater than the median
1446 value of r_a , as might be expected from the equations governing the resistances as given in Appendix C of
1447 Galmarini *et al.* (2021). Also, not all models were able to report all variables (as noted above, for
1448 CMAQ-M3Dry, the net and ground compensation point concentrations were calculated off-line of the model
1449 simulation, and could not be included as AQMEII4 diagnostic parameters). However, substantial
1450 differences between the panels of Figure 24 provide a useful indication of relative importance of different
1451 pathways in the participating models.

1452 From Figure 24, we note:

- 1453 (1) The 2016 July, 16 UT median aerodynamic resistance r_a is similar for all four models (Figure
1454 24(a)) – consequently, differences in r_a are unlikely to be the cause of the model flux differences.
- 1455 (2) The 2016 July, 16 UT median r_{sum} values (Figure 24(b)) for CMAQ-M3Dry is considerably
1456 smaller than for other models – at least some relatively high fluxes for CMAQ-M3Dry are due to
1457 these smaller r_{sum} values (which, appearing in the denominator for equation (13), will increase the
1458 magnitude of the fluxes). *et al.*
- 1459 (3) The 2016 July, 16 UT median r_{sum} values for CMAQ-STAGE over land are equal to those for r_a
1460 for this model. This is expected ($r_{sum} = r_a$ for this model, Galmarini *et al.*, 2021); other terms
1461 influence the magnitude and direction of the fluxes.
- 1462 (4) The 2016 July, 16 UT median values of the air concentrations of NH_3 , c_a (Figure 24(c)) are lower
1463 for CMAQ-M3Dry and CMAQ-STAGE than for GEM-MACH (Base) and GEM-MACH
1464 (Zhang), as might be expected from the above-mentioned bias calculations relative to CrIS and
1465 AMoN data.
- 1466 (5) The 2016 July, 16 UT median net compensation point concentration c_c (Figure 24(d)) for CMAQ-
1467 STAGE is an order of magnitude smaller than for GEM-MACH (Base) and GEM-MACH
1468 (Zhang). From equation (13), this likely drives much of the large NH_3 flux for this model and its
1469 negative bias values; smaller c_c values will result in larger positive (downward) net fluxes F_T .
- 1470 (6) Some of the locations where CMAQ-STAGE's 2016 July, 16 UT median ground compensation
1471 point concentration (c_g) has maximized are where GEM-MACH (Base) and GEM-MACH
1472 (Zhang) have zero to near-zero ground compensation point values (Figure 24(e) – e.g. Rocky
1473 mountains, north-central USA agricultural region – dark blue areas in the GEM-MACH results
1474 compared to much lighter values in the CMAQ-STAGE results). The larger CMAQ-STAGE c_g
1475 values (local values were up to $1\text{E}4$ ppbv for this model), if dominant, would be expected to
1476 result in larger c_c values in equation (13) (see Galmarini *et al.* 2021) and hence a tendency
1477 towards smaller downward fluxes. This is not the case from the above analysis (DNH₃ values in
1478 Table 7 for CMAQ-STAGE are greater than those of the GEM-MACH models, and CMAQ-
1479 STAGE NH₃ concentrations have more negative biases than the two GEM-MACH models),

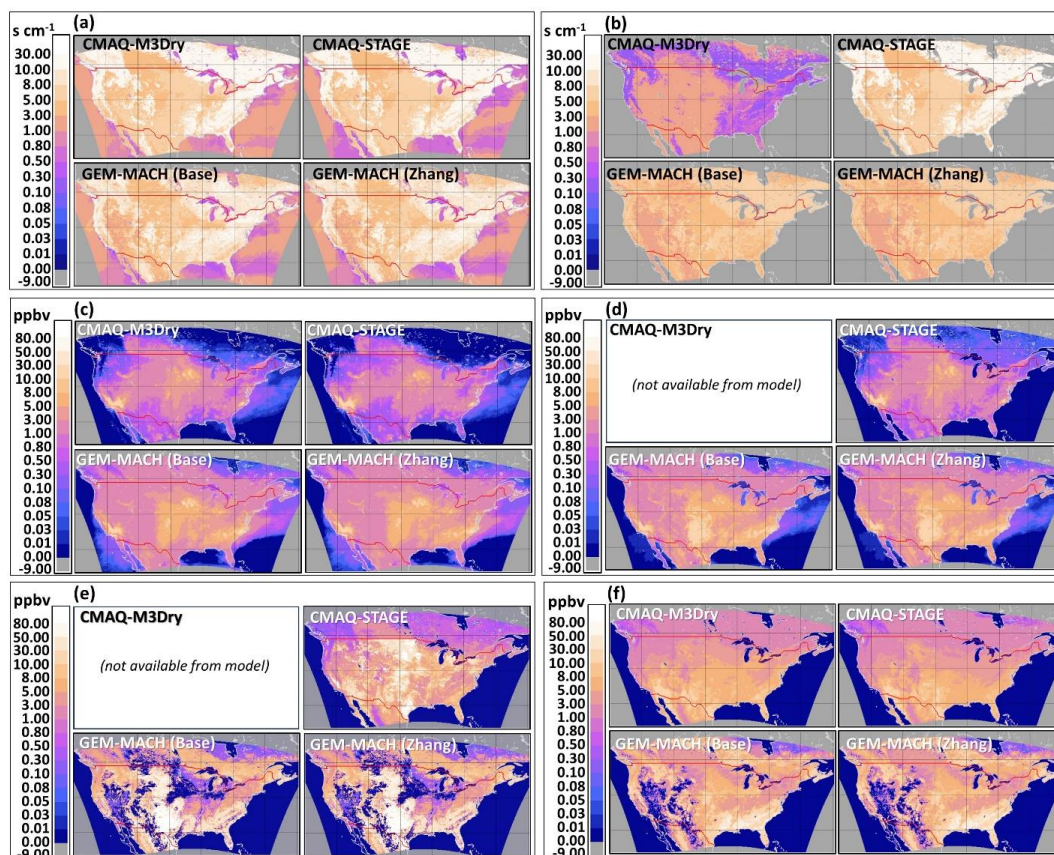


1480 suggesting that the ground pathway is not the main term affecting the differences in model NH_3
 1481 dry deposition fluxes.

1482 (7) For much of the AQMEII4 common domain (aside from SW USA), CMAQ-M3Dry and CMAQ-
 1483 STAGE have lower 2016 July, 16 UT median stomatal compensation point concentrations than
 1484 either GEM-MACH (Base) or GEM-MACH (Zhang) (Figure 24(f)). This in turn implies that the
 1485 difference in model dry deposition fluxes is via the stomatal pathway.

1486 The main factors resulting in higher magnitude downward fluxes in CMAQ-M3Dry and CMAQ-STAGE
 1487 relative to GEM-MACH (Base) and GEM-MACH (Zhang) are thus lower net compensation point
 1488 concentrations (CMAQ-STAGE), lower stomatal compensation point concentrations (CMAQ-M3Dry,
 1489 CMAQ-STAGE), and lower r_{sum} values (CMAQ-M3Dry).

1490 Figure 24. 2016 Spatial distribution of 2016 July, 16 UT median n values for key bidirectional flux diagnostic
 1491 variables. (a) Aerodynamic resistance (s cm^{-1}), r_a . (b) Sum resistance (s cm^{-1}), r_{sum} . (c) Air Concentration of NH_3
 1492 (ppbv), c_a . (d) Net compensation point concentration (ppbv), c_c . (e) Ground compensation point concentration
 1493 (ppbv), c_g . (f) Stomatal compensation point concentration (ppbv), c_s .



1494

1495 All four bidirectional flux models calculate fluxes on specific land use types within each grid cell and use
 1496 some form of land use fraction weighting to generate the values of the key parameters in the bidirectional
 1497 flux equations. The native land-use types used by each modelling platform were converted to a common



1498 set of 16 AQMEII4 land use types (see Galmarini *et al.*, 2021). We investigated the CMAQ and GEM-
1499 MACH spatial and temporal patterns of ammonia bidirectional fluxes in the context of the AQMEII4
1500 land-use types, along with the relationship to the highest regions of nitrogen CLE. This is shown in
1501 Figures 25 and 26, where Figure 25 panels (a and b) are the sum of AQMEII4 land use types 11 and 12
1502 (i.e. the sum of “planted/cultivated” and “grassland” land use types) used in CMAQ and GEM-MACH
1503 respectively. Figure 25 panels (c and d) are the sum of AQMEII4 land use fractions for land use types 6,7,8
1504 and 13 (evergreen broadleaf forest, deciduous broadleaf forest, mixed forest, and savanna, respectively),
1505 for CMAQ and GEM-MACH respectively. We note that these forested areas are the ecosystems of
1506 interest for many of the CLE values calculated earlier in this work. The land use summations of Figure
1507 25 are also worth noting in the context of the typical timing of the direction of NH_3 fluxes during the
1508 course of a day. Figure 26 shows an example of this diurnal behaviour of the NH_3 bidirectional fluxes
1509 for the CMAQ and GEM-MACH models, at (a) 15:00 CDT and (b) 7:00 CDT. Mid-afternoon fluxes
1510 (Figure 26(a)) tended to be largely negative (upward; emissions; blue colours). However, the spatial
1511 location of the fluxes differs between the models even within a given model framework. CMAQ-M3Dry
1512 predicts afternoon emissions (blue colours) largely restricted to the combined grassland and agricultural
1513 land use types, with deposition (red colours) to the forested areas in south-east Canada and south-east
1514 USA. CMAQ-STAGE predicts mid-afternoon emissions throughout western North America, though a
1515 similar pattern of deposition as CMAQ-M3Dry in south-east Canada and south-east USA. The GEM-
1516 MACH bidirectional fluxes in afternoon are mostly negative (emissions; blue). All three models show
1517 midafternoon NH_3 deposition in the north-central USA, corresponding to a known region of high NH_3
1518 concentrations (Figure 22, CrIS NH_3 retrieval maximum). In contrast, early morning fluxes (Figure
1519 26(b)) predicted by both CMAQ implementations are largely positive (downward; deposition; red
1520 colours), across all land use types., while GEM-MACH predicts deposition in agricultural areas, and
1521 emissions further downwind in south-east Canada and south-east USA.

1522 The generic diurnal sign changes in the direction of the ammonia flux across all four models is easily
1523 explained with reference to equation (13): in mid-afternoon (Figure 26(a)), both the height of the
1524 planetary boundary layer and the magnitude of thermal coefficients of diffusivity are relatively high,
1525 reducing the ambient air concentration of ammonia gas (c_a in eqn 13), resulting in negative fluxes
1526 (emissions; blue colours). In the early morning (Figure 26(b)), both the boundary layer height and the
1527 magnitude of thermal coefficients of diffusivity are lower, hence increasing the ambient air concentrations
1528 of ammonia gas, resulting in more positive fluxes and prevalent deposition. However, the different
1529 bidirectional flux models show differences in diurnal behaviour by land use type. CMAQ-M3Dry and
1530 CMAQ-STAGE show a diurnal pattern of afternoon emissions from agricultural and grassland areas, and
1531 deposition in forested regions downwind, and early morning deposition irrespective of land-use type.
1532 GEM-MACH shows stronger afternoon emissions regardless of land-use type, and morning lower
1533 magnitude emissions in forested areas and deposition only in agricultural areas and the western USA.

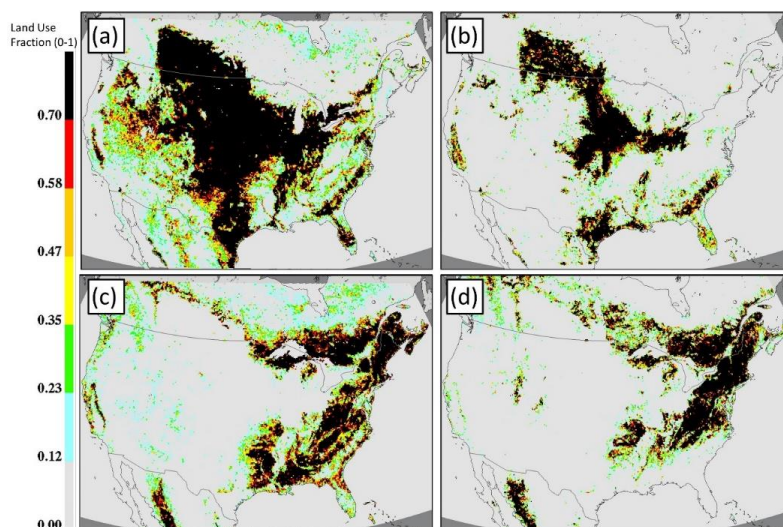
1534 We note that Table 9 measures model performance specifically at satellite overpass time in the afternoon –
1535 i.e. at close to the time shown in Figure 26(a), and that the performance of CMAQ-M3Dry and CMAQ-
1536 STAGE is lower than the other models at this time, while the differences between the models aside from
1537 magnitude of the bias is less pronounced in the integrated surface observations of Table 9. This analysis
1538 thus suggests that the CMAQ negative biases may be reduced in magnitude by re-examining the factors
1539 contributing to compensation point concentrations in forested areas in the day; c_c values (eqn. 13) are
1540 probably too low in these regions at these times, leading to excessive positive (downward) fluxes. That
1541 is, the analysis suggests that the CMAQ negative NH_3 biases may be the result of excessive deposition
1542 and/or insufficient emissions, in forested areas, in both the daytime and early morning, with the effect
1543 most noticeable in the afternoon. The bulk of the differences likely resides in the stomatal deposition



1544 pathway. Conversely, we note that the GEM-MACH bidirectional flux algorithm is overestimating
1545 midafternoon ammonia in the SE USA relative to satellite observations (Figure 22), indicating that
1546 compensation point concentrations may be overestimated in this region.

1547 While NH_3 fluxes are only the 5th largest source of N deposition in the North American reduced ensemble,
1548 we also note that the manner in which NH_3 bidirectional fluxes are treated in the context of critical load
1549 exceedance calculations may be open to interpretation. Exceedances with respect to critical loads are
1550 calculated with respect to annual *total* deposition of N and S, but what constitutes total N deposition in
1551 the context of bidirectional fluxes is less clear. Here, we have taken the approach of assuming that
1552 negative fluxes (emissions) of NH_3 during the course of a year constitute a loss of N from the ecosystem,
1553 but that NH_3 contained within the ecosystem cannot be converted to other forms of N. Consequently, the
1554 approach taken here was to sum the hourly NH_3 fluxes (positive downward and negative upward) for the
1555 year simulated, with only those grid cells with net positive summations (i.e. net annual deposition fluxes)
1556 adding towards total N deposition. However, other interpretations are possible. For example, only the
1557 positive contributions on an hourly basis could be accumulated, and any losses of N from the same
1558 ecosystems associated with NH_3 emissions could be ignored/excluded from the N balance of the
1559 ecosystem. A third interpretation would be to assume that deposited NH_3 within the ecosystem may be
1560 converted to other forms of N, and hence the net NH_3 flux (which may be positive or negative in different
1561 parts of the region simulated) is added to N_{dep} , with N_{dep} being set to zero only when the NH_3 emissions
1562 flux exceeds the deposition flux of all other forms of N. Here, we have taken the first of these
1563 approaches. We note that the second approach would lead to higher estimates of total N_{dep} than generated
1564 here, while the third approach would result in lower estimates of total N_{dep} . Although NH_3 is the 5th
1565 largest contributor to total N_{dep} across North America, these differences in approach may affect critical
1566 load exceedance estimates in regions of high NH_3 fluxes.

1567 Figure 25. Comparison of AQMEII4 land use type fractions with locations of highest CLE for forest ecosystems,
1568 CMAQ versus GEM-MACH. Upper row: grid cell fractional area composed of sum of AQMEII4 land use types
1569 11+12 (planted/cultivated and grassland), for: (a) CMAQ-M3Dry and CMAQ-STAGE, (b) GEM-MACH (Base) and
1570 GEM-MACH (Zhang). Lower row: grid cell fractional area composed of sum of AQMEII4 land use types
1571 6+7+8+13 (evergreen broadleaf forest, deciduous broadleaf forest, mixed forest, and savanna), for (c) CMAQ-
1572 M3Dry and CMAQ-STAGE, (d) GEM-MACH (Base) and GEM-MACH (Zhang).

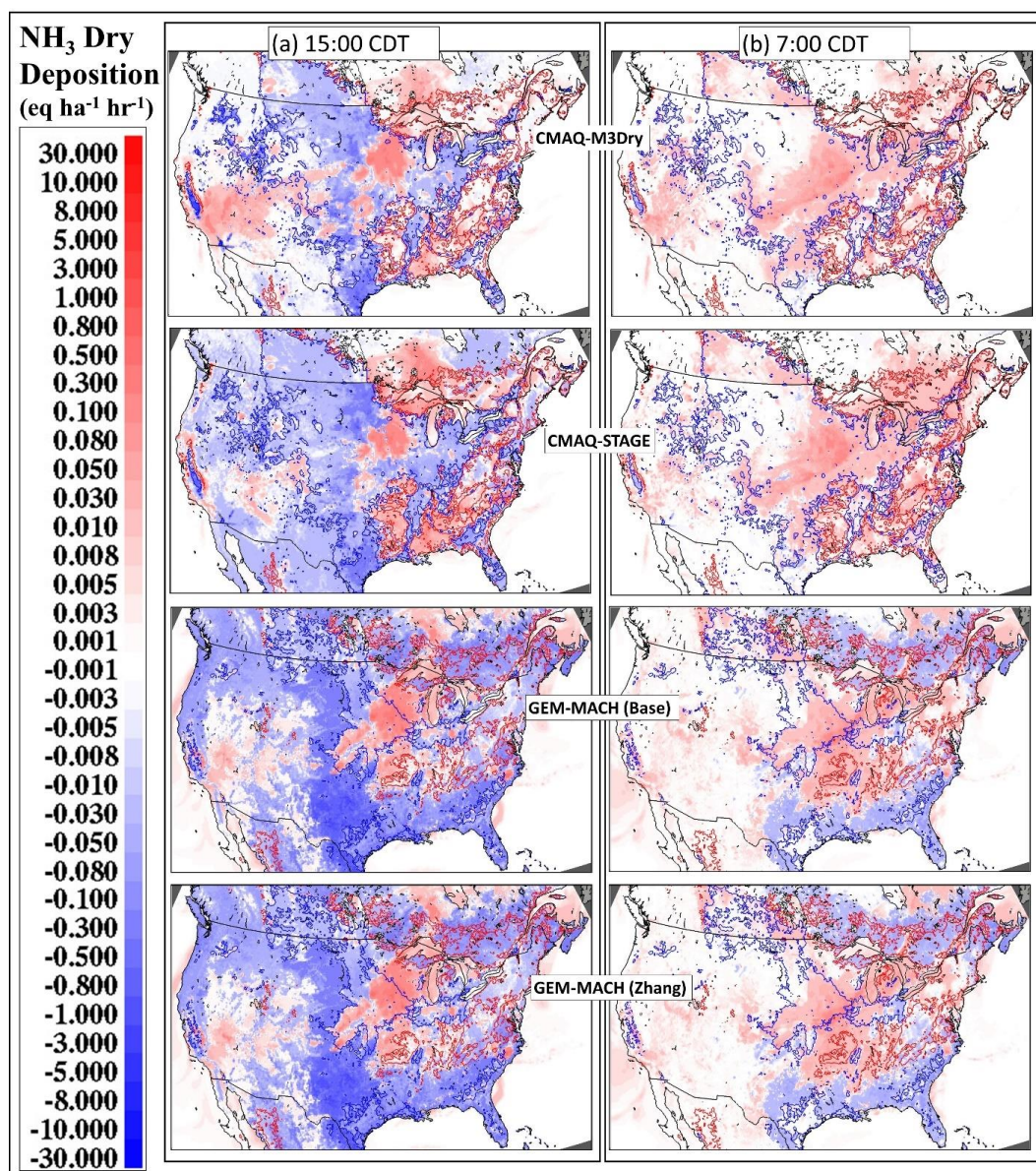


1573

1574



1575 Figure 26. $\text{NH}_3(\text{g})$ flux ($\text{eq ha}^{-1} \text{hr}^{-1}$) at (a) 15:00 CDT August 4, 2016 and (b) 7:00 CDT August 5, 2016. Blue lines
 1576 in the CMAQ and GEM-MACH models (horizontal row) panels encloses areas which are predominantly
 1577 agricultural and grassland, red line encloses areas which are predominantly evergreen broadleaf forest, deciduous
 1578 broadleaf forest, mixed forest and savanna, in each model's respective land use databases (se Figure 25). Blue
 1579 shaded regions indicate negative (upward; emissions) NH_3 fluxes, red shaded regions indicate positive (downward;
 1580 deposition) NH_3 fluxes.



1581

1582



1583 *3.2.3 Causes of S Deposition Variability in European Domain Simulations*

1584 The relative contributions of the different sources of S deposition in the AQMEII4 EU common domain
1585 for the year 2010 are shown in Table 11 and Figure 27.

1586 The European ensemble contributions to total S deposition contrasted with those in North America; both
1587 the contribution to total S deposition and the magnitude of variability between the models follow the
1588 same descending order of importance: SO₂ dry deposition followed by wet (SO₄²⁻ + HSO₃⁻) deposition,
1589 followed by particulate sulphate dry deposition (see Table 11). The relatively higher importance of SO₂
1590 dry deposition towards total sulphur deposition, compared to North America, may reflect a denser spatial
1591 distribution of SO₂ emissions in the EU domain compared to the North American domain, as well as
1592 higher EU emissions in 2010 compared to the NA 2016 year focused on here for model variability
1593 analysis. Another potential cause of differences between the two domains may reflect differences in the
1594 quality of the emissions data (and emissions reporting requirements) between the two jurisdictions. SO₂
1595 emissions are largely from industrial stacks in both locations. In North America, regulations require that
1596 facility operators for large stack sources report their emissions and stack parameters making use of
1597 Continuous Emissions Monitoring, on an hourly basis (USA) or as annual reports (Canada). Plume rise
1598 algorithms may then be used to distribute the emissions in the vertical within air-quality models. In the
1599 EU, stack sources are reported as annual totals without stack parameters which could be used for more
1600 accurate plume rise estimates (e.g. volume flow rates, effluent temperatures); the lack of this more
1601 detailed data necessitates approximations (either making use of “typical” plume rise rates or treating stack
1602 sources as surface emissions without plume rise). The larger variation in SO₂ performance in the
1603 simulations may thus reflect differences in the level of detail available within SO₂ emissions inventories
1604 in the two regions.

1605 European observation data for model evaluation were taken from the European Monitoring and
1606 Evaluation Programme (EMEP; <https://www.emep.int/>, last accessed July 11, 2024), and the European
1607 Air Quality Database (AIRBASE; [https://data.europa.eu/data/datasets/data_airbase-the-european-air-](https://data.europa.eu/data/datasets/data_airbase-the-european-air-quality-database-1?locale=en)
1608 [quality-database-1?locale=en](https://data.europa.eu/data/datasets/data_airbase-the-european-air-quality-database-1?locale=en), last accessed July 11, 2024).

1609 Table 11. Average S deposition contributions in common AQMEII4 EU grid area (eq ha⁻¹ yr⁻¹) and percent
1610 contribution to average total S deposition, 2010.

Model Number	Average Deposition (eq ha ⁻¹ yr ⁻¹)				Percent of total S deposition		
	SO ₂ (g) Dry Deposition	SO ₄ ⁽²⁻⁾ + HSO ₃ ⁽⁻⁾ Wet Deposition	Particle Sulphate Dry Deposition	Total S Deposition	SO ₂ (g) Dry Deposition	SO ₄ ⁽²⁻⁾ + HSO ₃ ⁽⁻⁾ Wet Deposition	Particle Sulphate Dry Deposition
WRF-Chem (IASS)	92.1	42.1	n.r.	134.2	68.6	31.4	n/d
LOTOS-EUROS (TNO)	38.3	37.9	5.4	81.5	47.0	46.4	6.6
WRF-Chem (UPM)	105.6	63.2	3.2	172.0	61.4	36.7	1.9
CMAQ (Hertfordshire)	125.7	75.9	20.1	221.6	56.7	34.3	9.0
Reduced ensemble average	89.9	59.0	9.5	158.4	56.7	37.2	6.0
Reduced ensemble standard deviation	37.3	15.8	7.5	58.0	23.6	10.0	4.7

1611



1612 *Dry deposition of SO₂*

1613 The model SO₂ performance relative to observations at stations closer to urban centers (AIRBASE
1614 network), and more broadly distributed over the EU region (EMEP network), as well as comparisons
1615 to wet (SO₄²⁻ + HSO₃⁻) deposition (EMEP wet deposition network), are shown in Table 12. Observation
1616 station locations are shown in Figure S9. WRF-Chem (IASS) had the best SO₂ performance relative to
1617 both networks for most statistics, with the exceptions of a slightly smaller FAC2 score compared to other
1618 models for both AIRBASE and EMEP, and the largest negative bias for SO₂ relative to AIRBASE
1619 observations. The proximity of AIRBASE station locations to SO₂ sources can also be seen in Figure 28,
1620 where the AIRBASE monthly concentration y-axis (Figure 29(a)) is almost twice that of the EMEP
1621 monthly concentration y-axis (Figure 28(b)). Observed SO₂ close to sources (Figure 28(a), red lines)
1622 shows a strong seasonal variability, with concentrations in the winter being a factor of two higher than
1623 HNO₃ summer than summer, likely showing the effect of increased winter stability on plume rise. This
1624 tendency is greatly reduced at regional stations (Figure 28(b), red lines). LOTOS-EUROS (TNO)
1625 matches the near-source SO₂ time series the most closely, while CMAQ (Hertfordshire) overestimates the
1626 impact of seasonal variability (Figure 28(a)). At regional stations, LOTOS-EUROS (TNO) and CMAQ
1627 (Hertfordshire) overestimate seasonal variation, while WRF-Chem (IASS) most closely matches
1628 observations. At least some of the variation in simulated SO₂ performance relative to observations and
1629 hence in SO₂ deposition fluxes and critical load exceedance estimates is due to some models
1630 overestimating the seasonal variation in SO₂ at regional locations further from cities. This may reflect
1631 differences in atmospheric stability, the seasonal response of the deposition algorithms, or the manner in
1632 which plume rise is simulated between the models.

1633 WRF-Chem (IASS) has the best overall performance for SO₂; while this model's mean bias is the most
1634 negative for observation sites close to the sources (AIRBASE comparison), the remaining statistics are
1635 the best of the ensemble, and the model bias performance is also better than the other models as the
1636 distance from the sources increases (EMEP comparison). The large negative biases in WRF-Chem
1637 (IASS) model values may indicate an overestimate of SO₂ deposition, though other model processes may
1638 also play a role.

1639 *Wet Deposition of Sulphur*

1640 As was the case for most models on the North American domain, all EU domain models underestimated
1641 wet deposition relative to observations (note negative biases in Table 12 and monthly time series
1642 comparison versus observations in Figure 28(c)). CMAQ (Hertfordshire) outperforms the other models
1643 relative to observations, though we note that the wet sulphur deposition bias for this model is nevertheless
1644 -0.39 eq ha⁻¹ yr⁻¹, with a correlation coefficient of 0.15. In contrast to the North American wet sulphur
1645 deposition comparison time series (Figure 16, Table 6), the European wet deposition observations do not
1646 show a spring-time peak in values, rather a seasonality centered around the month of June, with higher
1647 values extending from March to September.

1648



1649 Table 12. Model performance statistics for EU domain SO₂ concentrations and total wet S deposition, μg
1650 m⁻³ and eq ha⁻¹ yr⁻¹, respectively.

	SO ₂ (Airbase)				SO ₂ (EMEP)			
	WRF-Chem (IASS)	LOTOS-EUROS (TNO)	WRF-Chem (UPM)	CMAQ (Hertfordshire)	WRF-Chem (IASS)	LOTOS-EUROS (TNO)	WRF-Chem (UPM)	CMAQ (Hertfordshire)
FAC2	0.35	0.36	0.38	0.35	0.35	0.36	0.34	0.29
MB	-1.42	0.04	0.06	1.89	0.32	0.48	0.58	1.76
MGE	4.60	5.32	5.29	6.35	1.48	1.66	1.63	2.57
NMGE	0.85	0.98	0.97	1.17	1.07	1.20	1.18	1.87
RMSE	14.47	15.64	15.27	17.60	2.92	3.58	2.98	5.80
R	0.28	0.26	0.24	0.26	0.38	0.33	0.34	0.35
COE	0.12	-0.01	-0.01	-0.21	-0.08	-0.21	-0.19	-0.88
IOA	0.56	0.49	0.50	0.40	0.46	0.40	0.40	0.06
Total Wet S deposition								
	WRF-Chem (IASS)	LOTOS-EUROS (TNO)	WRF-Chem (UPM)	CMAQ (Hertfordshire)				
FAC2	0.00	0.19	0.28	0.31				
MB	-1.51	-1.22	-1.08	-0.39				
MGE	1.53	1.34	1.29	1.42				
NMGE	1.00	0.87	0.84	0.92				
RMSE	6.61	6.50	6.48	6.46				
R	0.02	0.11	0.11	0.15				
COE	0.04	0.16	0.19	0.11				
IOA	0.52	0.58	0.60	0.56				

1651

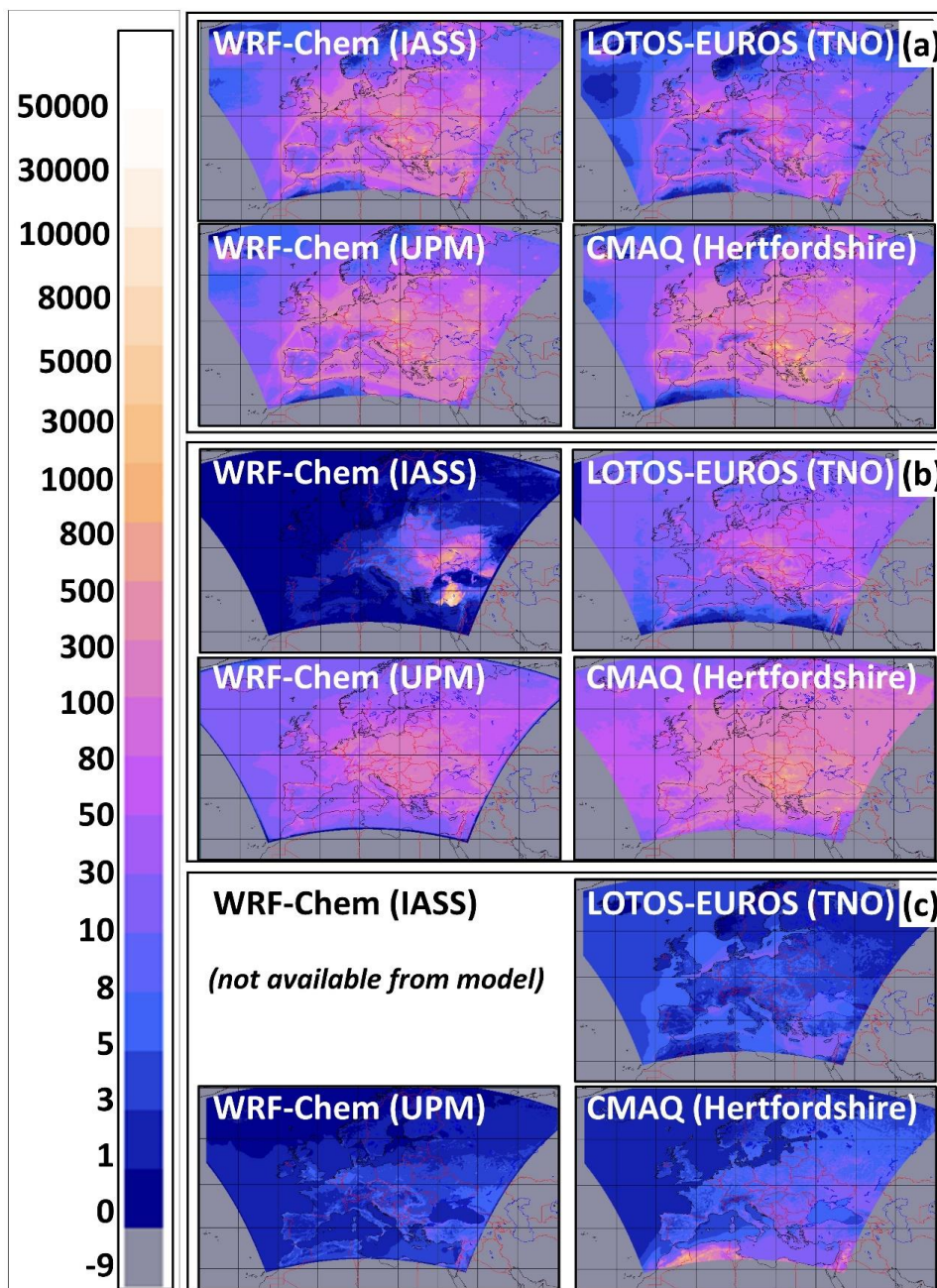
1652 None of the EU models made use of updated particle dry deposition velocities available in more recent
1653 literature; as a result, the relative contribution of particle dry deposition towards EU model-to-model
1654 variability is small. Speciated PM observations were not available for comparison to model predictions in
1655 the EU region.

1656 The spatial distribution of the relative contributions of the three forms of sulphur deposition for the year
1657 2010 is shown in Figure 27. CMAQ (Hertfordshire), with the highest SO₂ deposition flux (Figure 27(a),
1658 see also Table 11, Table 12) also has the most positive SO₂ concentration mean bias. With increasing
1659 distance from the sources, the SO₂ loss or conversion processes of all four models are likely
1660 underestimated (EMEP SO₂ biases are positive for all models, Table 12). In contrast, all models have
1661 significant negative biases in wet sulphur deposition (Table 12), hence at least one reason for this
1662 underestimate may be insufficient conversion of SO₂ to ionic sulphate and bisulphite in simulated cloud
1663 water, through uptake of SO₂ and scavenging of particulate sulphate. The wet deposition of sulphur in
1664 WRF-Chem (IASS) in particular seems anomalously low (Figure 27(c), Figure 28 (b)), with much of
1665 Europe having little to no wet sulphate deposition in this model.



1666

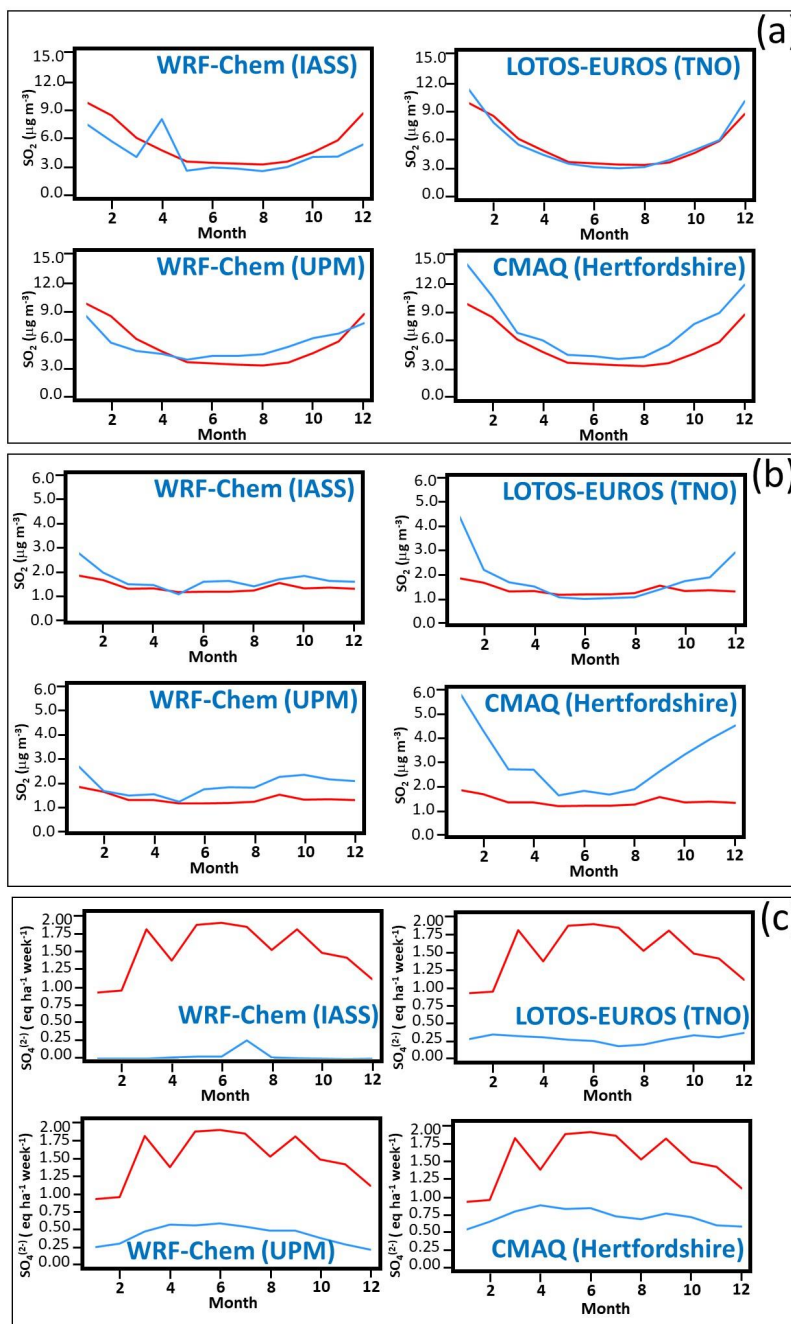
1667 Figure 27. Spatial distribution and magnitude of contributions to annual S deposition, AQMEII4 common EU
1668 domain, 2010 (eq ha⁻¹ yr⁻¹). (a) SO₂(g) dry deposition. (b) Total wet S deposition. (c) Particle sulphate dry
1669 deposition.



1670



1671 Figure 28. Comparison of observed and modelled S, AQMEII4 EU common domain, 2010. (a) AIRBASE SO₂ (ug
 1672 m⁻³). (b) EMEP SO₂ (ug m⁻³). (c) Wet flux of total S deposition (eq ha⁻¹ week⁻¹). Red: observations. Blue: model.



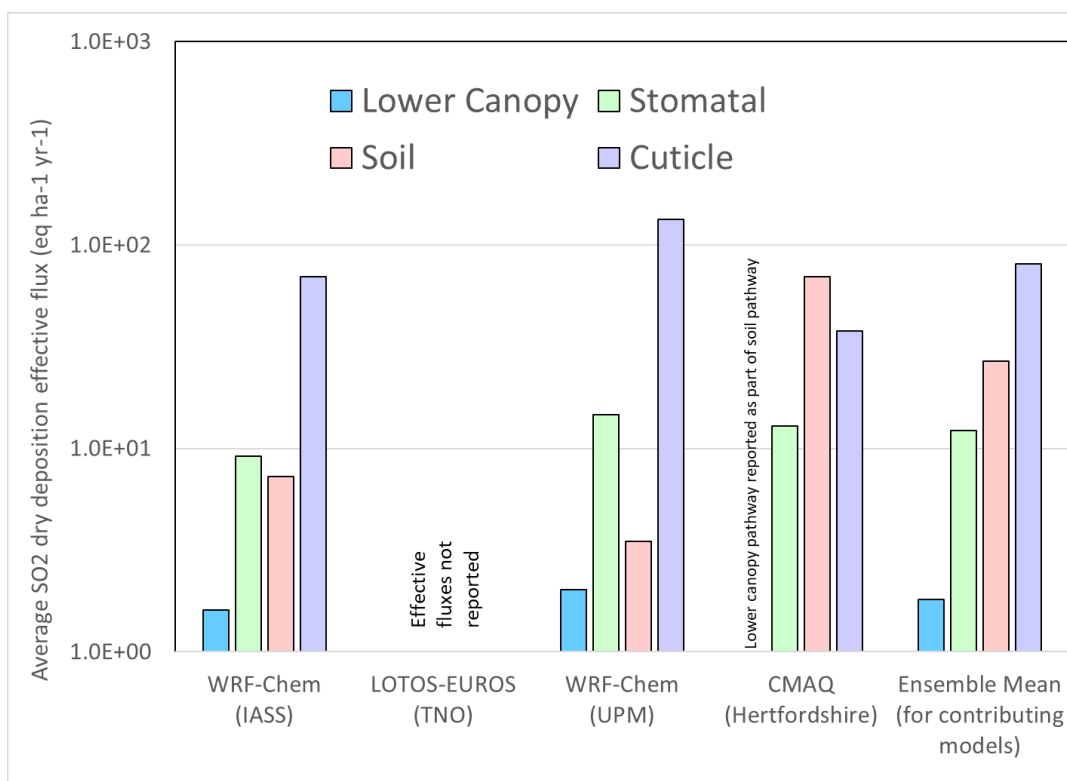
1673

1674



1675 A comparison of the relative differences in the deposition pathway strength for the models may help shed
 1676 light on the causes of SO₂ deposition flux variability between the models. However, no effective fluxes
 1677 were reported by LOTOS-EUROS (TNO). Figures S15 and S16 show the spatial distribution of the
 1678 summed annual effective fluxes for the reporting models, with the results in the common AQMEII4 EU
 1679 domain summarized in Figure 29.

1680 Figure 29. Averages of effective flux pathway contributions to SO₂ dry deposition, AQMEII4 common EU grid,
 1681 2010 (eq ha⁻¹ yr⁻¹).



1682

1683 Despite having the highest average SO₂ deposition flux (Table 11), CMAQ (Hertfordshire) also has the
 1684 highest positive biases for SO₂ ambient concentrations (Table 12). From Figures S15, S16 and 29, the
 1685 CMAQ (Hertfordshire) positive biases may be the result of spatial variations in deposition, specifically, to
 1686 low contributions to the cuticle effective fluxes in Northern Europe for this model (Figure S15(a)).
 1687 Despite these relatively low values, the SO₂ net dry deposition flux for this model (Table 11) is higher
 1688 than that of the other models, implying that the low northern EU fluxes are being offset by higher values
 1689 elsewhere (eg. via the soil flux, compare soil and cuticle values in Figure 29). We note that the effective
 1690 flux analysis is restricted to grid cells that do not have water as a dominant land use type (a maximum of
 1691 1% water land fraction was used as an exclusion criterion); for grid cells held in common (mostly land),
 1692 the CMAQ (Hertfordshire) the cuticle effective flux pathway specifically is lower than that of the other
 1693 models, while the differences are less noticeable for the other terms, as reflected by the summary values
 1694 in Figure 29. Other than Northern Europe, CMAQ (Hertfordshire) has higher soil fluxes than WRF-
 1695 Chem (IASS). Similar to AQMEII4 analyses for ozone (Hogrefe *et al.*, 2024, under preparation), the



1696 relative importance of the different pathways towards total deposition varies between the models. For
1697 example, WRF-Chem (IASS), with the best overall performance for SO₂ concentrations aside from bias
1698 and factor of 2, has flux contributions in descending order of importance: cuticle, stomatal, soil and lower
1699 canopy. For CMAQ (Hertfordshire), with relatively poor performance and high positive biases (Table 12),
1700 the flux contributions in descending order of importance are soil, cuticle, and stomatal (with lower canopy
1701 being incorporated as part of soil flux, for this model), and the cuticle pathway contributes less to
1702 deposition in northern Europe than the other models.

1703 *3.2.4 Causes of N Deposition Variability in European Domain Simulations*

1704 The common AQMEII4 EU domain relative contributions for each model's deposited species towards
1705 total nitrogen deposition and its variability are shown in Table 13. The contributions towards total N
1706 deposition for the reduced ensemble, in descending order of importance, were wet NO₃⁻, dry HNO₃, wet
1707 NH₄⁺, dry NH₃, dry particulate nitrate, dry NO₂, and dry particle ammonium, with relatively small
1708 contributions from the other depositing N species. The spatial distributions of the four largest
1709 contributions to total N deposition are shown in Figure 30. The largest contributions to model-to-model
1710 variability, in descending order, were wet NO₃⁻, dry HNO₃, dry NH₃, wet NH₄⁺, and dry NO₂, with smaller
1711 contributions towards variability from the other species.

1712 Wet deposition fluxes of NO₃⁻ and NH₄⁺ and the ground-level concentration of NO₂ are evaluated in Table
1713 14; monthly average time series comparisons wet deposition to the observations are provided in Figure
1714 31. From Figure 30, WRF-Chem (IASS) predicted much lower magnitude wet NO₃⁻ and wet NH₄⁺
1715 deposition fluxes than the other three models, and from Table 14, these result in larger negative biases and
1716 poor overall performance relative to observations for WRF-Chem (IASS) in comparison to the other
1717 models. LOTOS-EUROS (TNO) had the best overall performance for NH₄⁺ and NO₃⁻ wet deposition
1718 fluxes. However, similar to the case for wet S deposition, all models have significant negative biases for
1719 both nitrogen ion wet fluxes, as can be seen from Table 14 and Figure 31. LOTOS-EUROS (TNO) has
1720 the best performance for statistics relating to the spatial and temporal distribution of wet deposition, while
1721 WRF-Chem (UPM) has the lowest bias for wet NO₃⁻ deposition. A common feature of the AQMEII4
1722 ensemble of models for both EU and NA domains are these negative biases for wet deposition of both
1723 sulphate and nitrogen species. Also, we note that the observed wet NH₄⁺ deposition (Figure 31(b), red
1724 line) peaks in June, while the model values (blue lines) peak earlier, in March. This in contrast to the
1725 North American NH₄⁺ comparison (Figure 19), where observed peaks occur in April and model peaks
1726 occur in June.

1727

1728



1729 Table 13. Contributions of N species towards total deposition (eq ha⁻¹ yr⁻¹ and percent of total N deposited, common
 1730 AQMEII4 EU grid, 2010, arranged in descending order of importance to the reduced ensemble average. DNH3: dry
 1731 deposition of NH₃(g). WNH4: wet deposition of NH₄⁺(aq). DHNO3: dry deposition of HNO₃(g). WNO3: wet
 1732 deposition of NO₃⁻(aq). DAM: dry deposition of particulate ammonium. DNI: dry deposition of particulate nitrate.
 1733 DNO₂: dry deposition of NO₂(g). DPAN: dry deposition of peroxyacetyl nitrate gas. DRN3: dry deposition of
 1734 organic nitrate gases. DN2O5: dry deposition of N₂O₅(g). DHNO4: dry deposition of pernitric acid gas. DNO: dry
 1735 deposition of NO(g). nr = not reported. ndd = no dry deposition

1736

Average (eq ha ⁻¹ yr ⁻¹)						
Model						
Species	WRF-Chem (IASS)	LOTOS-EUROS	WRF-Chem (UPM)	CMAQ (Hertfordshire)	Red. Ens Avg	Red. Ens. Std Dev
WNO3	1.8	77.8	174.8	96.2	116.2	42
DHNO3	50.2	38.4	120.5	78.6	79.2	33.5
WNH4	4.3	90.3	74.6	64.1	76.3	10.8
DNH3	60.5	76.8	47.9	29.6	51.5	19.4
DNI	nr	18.2	25.9	13.5	19.2	5.1
DNO2	11.6	23.6	27.5	6.3	19.2	9.2
DAM	nr	14.2	6.2	6.6	9	3.7
DPAN	2.3	ndd	2.7	5.2	4	1.2
DN2O5	5.3	1.2	ndd	1	1.1	0.1
DRN3	0.3	ndd	0.6	3.2	1.9	1.3
DHNO4	1.4	ndd	0.9	0.2	0.5	0.4
DNO	0.1	2	0.2	0.4	0.9	0.8
Total N	137.6	342.7	481.9	304.8	376.5	76.1
Percent Contribution						
Model						
Species	WRF-Chem (IASS)	LOTOS-EUROS	WRF-Chem (UPM)	CMAQ (Hertfordshire)	Red. Ens Avg	Red. Ens. Std Dev
WNO3	1.3	22.7	36.3	31.5	30.9	5.6
DHNO3	36.5	11.2	25	25.8	21	6.7
WNH4	3.1	26.4	15.5	21	20.3	4.4
DNH3	43.9	22.4	9.9	9.7	13.7	5.9
DNI	nr	5.3	5.4	4.4	5.1	0.4
DNO2	8.4	6.9	5.7	2.1	5.1	2.1
DAM	nr	4.1	1.3	2.2	2.4	1.2
DPAN	1.7	nd	0.6	1.7	1.1	0.6
DN2O5	3.8	0.3	nd	0.3	0.3	0
DRN3	0.2	nd	0.1	1.1	0.5	0.5
DHNO4	1	nd	0.2	0.1	0.1	0.1
DNO	0	0.6	0	0.1	0.2	0.2

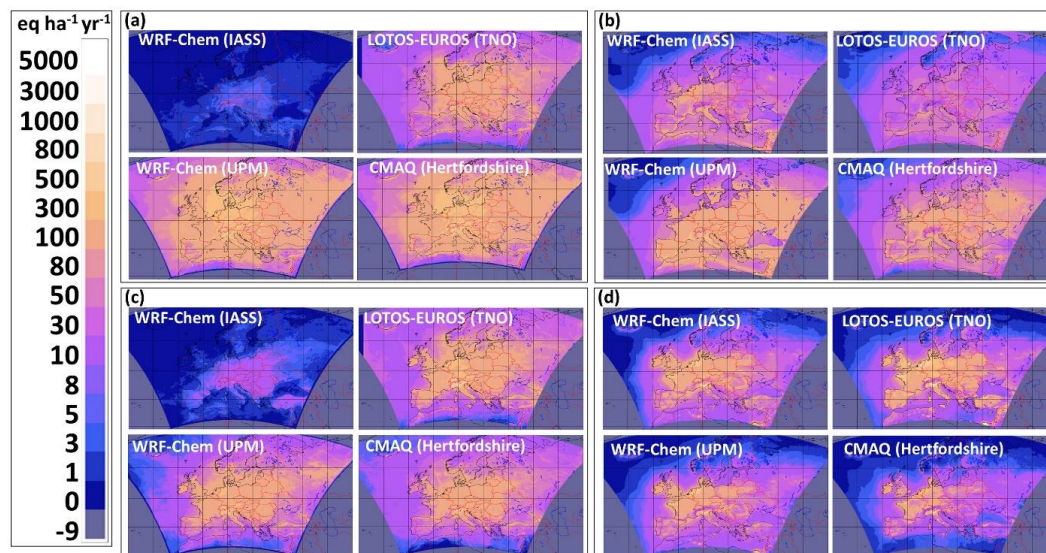
1737

1738

1739



1740 Figure 30. Spatial distribution of contributions of (a) wet nitrate ion deposition, (b) dry gaseous HNO₃
 1741 deposition, (c) wet ammonium ion deposition, and (d) dry gaseous ammonia deposition towards total N
 1742 deposition in the common AQMEII4 EU domain, 2010 (eq ha⁻¹ yr⁻¹).



1743

1744 Dry deposition of HNO₃ was the second largest source of modelled EU nitrogen deposition variability.
 1745 The spatial distribution of the relative contributions of the four pathways towards the mass flux of HNO₃
 1746 is shown in Figures S17 and S18 and are summarized for the entire grid in Figure 32. There is more
 1747 heterogeneity between the EU models regarding the relative importance of the HNO₃ deposition pathways
 1748 than was observed for the North American simulations (compare Figures 21 and 32). In the North
 1749 American simulations, the cuticle deposition pathway also dominated for all models, followed by the soil
 1750 pathways. In the EU simulations, the reported soil pathway for WRF-Chem (UPM) is several orders
 1751 of magnitude smaller than the same pathway for CMAQ (Hertfordshire). The cuticle pathway dominates
 1752 for WRF-Chem (IASS) (not shown) and CMAQ (Hertfordshire). The stomatal pathway magnitude is less
 1753 than the cuticle pathway for the EU models, but greater in general than for the North American models,
 1754 where the stomatal pathway had a smaller contribution to HNO₃ dry deposition than the lower canopy
 1755 pathway.

1756 Observations of 2010 HNO₃(g), NH₃(g), and dry particle nitrate were not available for comparison to the
 1757 model predictions. However, observations of the NO₂ concentrations, the 6th largest contributor to total N
 1758 deposition and the 5th largest contributor to model-to-model variability, were available at near-source
 1759 AIRBASE and regionally distributed EMEP stations (Table 14). Aside from having the 2nd largest
 1760 magnitude mean bias, LOTOS-EUROS (TNO) had the best performance for NO₂ relative to stations
 1761 positioned close to emissions sources (AIRBASE), while WRF-Chem (IASS) and CMAQ (Hertfordshire)
 1762 had the best performance for NO₂ for stations distributed more widely across the region (EMEP).

1763



1764 Table 14. Model performance statistics for wet deposition of nitrate and ammonium ions, and ground level
 1765 concentrations of NO₂, AQMEII4 EU domain, 2010

	Wet NO ₃ ⁻ deposition (eq ha ⁻¹ yr ⁻¹)					Wet NH ₄ ⁺ deposition (eq ha ⁻¹ yr ⁻¹)			
	WRF-Chem (IASS)	LOTOS - EUROS (TNO)	WRF-Chem (UPM)	CMAQ (Hertfordshire)		WRF-Chem (IASS)	LOTOS - EUROS (TNO)	WRF-Chem (UPM)	CMAQ (Hertfordshire)
FAC2	0.00	0.32	0.35	0.31	FAC2	0.02	0.32	0.28	0.24
MB	-1.38	-0.75	-0.04	-0.58	MB	-1.80	-0.80	-1.01	-1.13
MGE	1.38	1.04	1.33	1.11	MGE	1.81	1.52	1.55	1.53
NMGE	0.99	0.75	0.96	0.80	NMGE	0.98	0.82	0.84	0.83
RMSE	2.66	2.19	2.53	2.25	RMSE	3.83	3.37	3.45	3.42
R	0.16	0.43	0.36	0.38	R	0.18	0.33	0.32	0.33
COE	-0.10	0.17	-0.06	0.11	COE	0.00	0.15	0.14	0.15
IOA	0.45	0.59	0.47	0.56	IOA	0.50	0.58	0.57	0.58
	AIRBASE NO ₂ concentrations (µg m ⁻³)					EMEP NO ₂ concentrations (µg m ⁻³)			
	WRF-Chem (IASS)	LOTOS - EUROS (TNO)	WRF-Chem (UPM)	CMAQ (Hertfordshire)		WRF-Chem (IASS)	LOTOS - EUROS (TNO)	WRF-Chem (UPM)	CMAQ (Hertfordshire)
FAC2	0.45	0.56	0.55	0.35	FAC2	0.57	0.53	0.39	0.50
MB	-10.00	-5.68	2.38	-12.40	MB	0.36	2.35	9.54	-2.02
MGE	12.67	11.22	13.61	13.84	MGE	5.01	6.18	11.49	4.90
NMGE	0.60	0.53	0.65	0.66	NMGE	0.57	0.70	1.31	0.56
RMSE	19.25	16.76	19.19	20.41	RMSE	8.17	10.01	17.28	8.29
R	0.49	0.56	0.47	0.50	R	0.71	0.64	0.61	0.67
COE	0.10	0.20	0.03	0.02	COE	0.31	0.15	-0.59	0.32
IOA	0.55	0.60	0.52	0.51	IOA	0.65	0.57	0.21	0.66

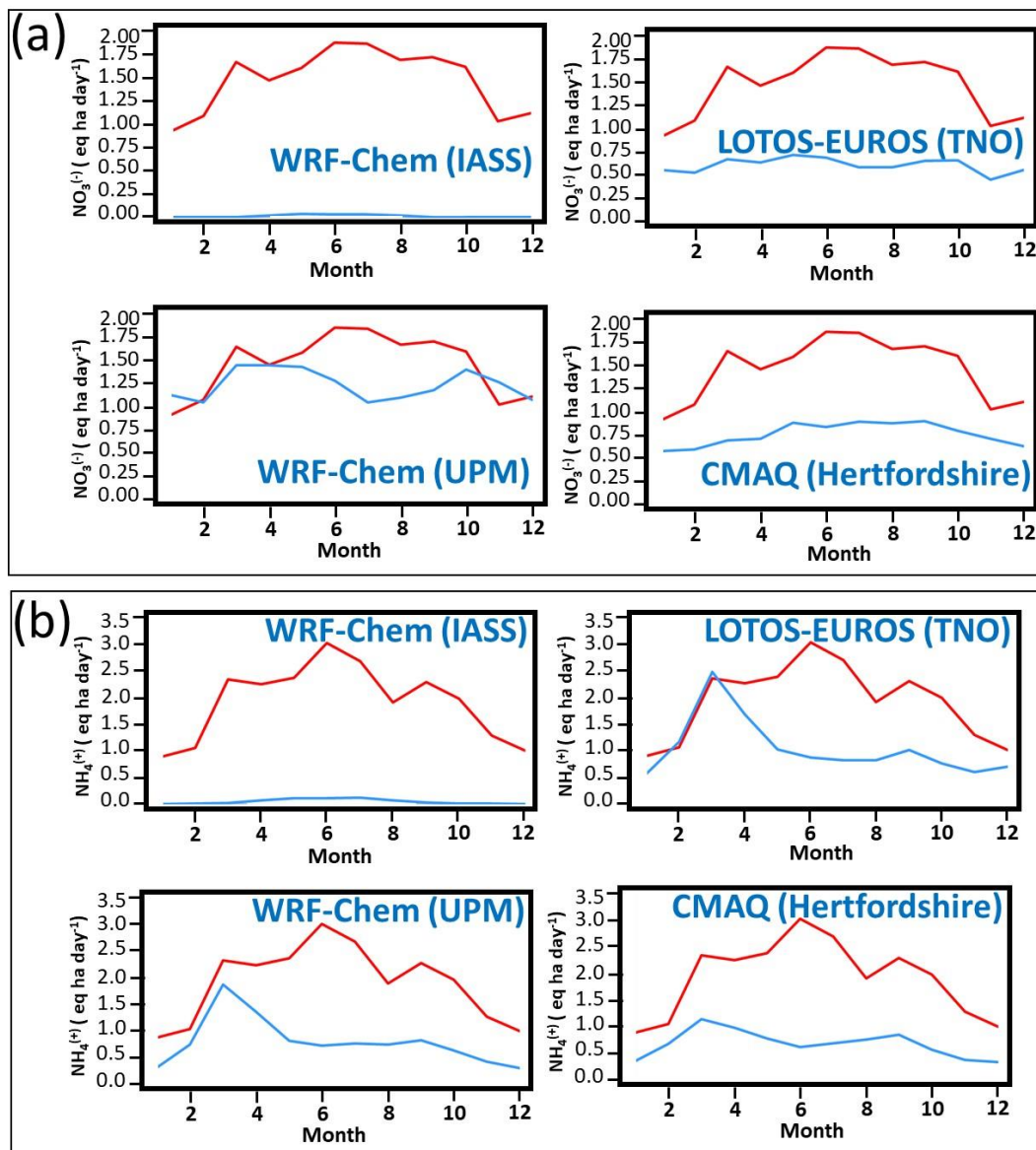
1766

1767

1768



1769 Figure 31. Monthly average comparison of wet nitrogen deposition, AQMEII4 common EU grid, 2010. (a) Average
1770 flux of NO_3^- (aq). (b) Average flux of NH_4^+ (aq). ($\text{eq ha}^{-1} \text{ day}^{-1}$)



1771

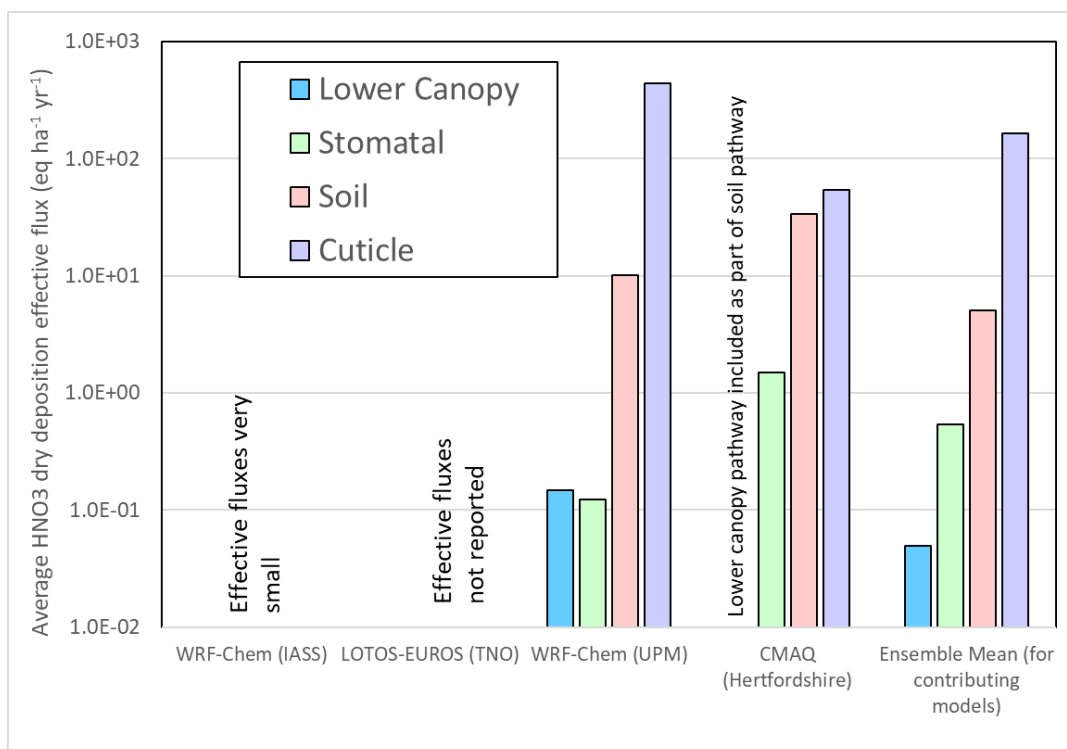
1772

1773

1774



1775 Figure 32. Averages of flux pathway contributions to HNO₃ dry deposition, AQMEII4 common EU grid,
1776 2010 (eq ha⁻¹ yr⁻¹).



1777

1778

1779 Conclusions

1780 We have used the AQMEII4 North American and European ensembles to calculate net Sulphur and
1781 Nitrogen deposition from individual models and a reduced ensemble of all models. These deposition
1782 estimates were used to calculate exceedances of critical loads for these two regions, using several critical
1783 load datasets. An in-depth analysis of the causes of model-to-model variability followed, using
1784 diagnostics designed for AQMEII4. We therefore subdivide these conclusions by the domain simulated,
1785 and the critical load exceedance and causes of model variability, within each domain.

1786 *North America, Critical Load Exceedances*

1787 All simulations showed a decrease in the size of the area in exceedance and the severity of exceedances
1788 with respect to acidification of forest ecosystems between the years 2010 and 2016. The percentage of
1789 North American forest area in exceedance of acidification critical loads was 13.2% (range 2.8% to 22.2%)
1790 in 2010, and 6.1% (1.0% to 12.9%) in 2016. Similarly, the percent exceedance with respect to acidity for
1791 aquatic ecosystems and the number of water bodies in exceedance decreased between 2010 and 2016
1792 from 21.2% (12.8 to 28.9%) in 2010 to 11.4% (7.3% to 15.8%) in 2016). The decrease in SO₂ emissions
1793 between these two years, and the resulting decreases in S deposition for all models, as well as decreases in
1794 N deposition for all models, drive these reductions in potential ecosystem damage.



1795 For sensitive epiphytic lichen species richness, all models also showed an improvement in the
1796 exceedances between 2010 and 2016. The improvement in the *total area* in exceedance predicted by
1797 most models was relatively small, but the severity of exceedance was greatly reduced. Given that the
1798 lichen community has a dose-response relationship with increasing deposition, this indicates reduced
1799 harm to forest health, even when the CL is still in exceedance. The reduced ensemble predicted a
1800 decrease in both severity and total area in exceedance from 2010 to 2016 from 81.5% (range 69.3 to 95%)
1801 in 2010 to 75.8% (range 63.7% to 90.7%) in 2016.

1802 For herbaceous species community richness, most models showed an improvement, often substantial, in
1803 both the total area in exceedance and the severity of exceedances between 2010 and 2016 (13.9%, range
1804 0.4 to 39.5%, in 2010 to 3.9%, range 0.1% to 18.4% in 2016).

1805 All models and the reduced ensemble thus showed improvements in the extent of potential ecosystem
1806 damage due to acidifying and eutrophying deposition between 2010 and 2016, in accordance with
1807 legislated emissions reductions policies coming into force between the two years. However, the amount
1808 of exceedance in any given year and the extent of reduction between the two years varied considerably
1809 between the models. Any individual model provides a similar direction of the change between the two
1810 years; the range of estimates suggests the utility of model ensembles where possible in estimating critical
1811 load exceedances.

1812 *North America, Causes of Model S Deposition Variability*

1813 The total mass of North American Sulphur deposition followed, in decreasing order of importance, wet
1814 deposition of S ($\text{SO}_4^{2-} + \text{HSO}_3^-$), dry deposition of particulate sulphate, and dry deposition of SO_2 . Dry
1815 deposition of particulate sulphate contributed the most to model-to-model variability in total Sulphur
1816 deposition, followed by wet deposition, and dry SO_2 deposition. The models with the highest wet S
1817 deposition levels had the best performance relative to monitoring network observations (CMAQ-M3Dry,
1818 CMAQ-STAGE, GEM-MACH (Ops)), though all models' wet S deposition was biased low relative to
1819 observations. A subgroup of models (GEM-MACH (Base), GEM-MACH (Zhang), GEM-MACH (Ops))
1820 had the highest positive biases in observed $\text{PM}_{2.5}$ sulphate concentrations relative to monitoring network
1821 observations, contributing to the model-to-model variability. Recent work by Ryu and Min (2022) and
1822 Ghahreman *et al.* (2024) suggests that model negative biases for wet deposition may be improved
1823 through incorporation of multiphase hydrometeor scavenging, and this may also reduce positive biases in
1824 particulate mass resulting from the implementation of the Emerson *et al.* (2020) particle dry deposition
1825 algorithm (GEM-MACH (Base) and GEM-MACH (Zhang)). Most North American reduced ensemble
1826 models were in relatively good agreement with regards to their predictions for the total dry deposition
1827 flux of $\text{SO}_2(\text{g})$.

1828 *North America, Causes of N Deposition Variability*

1829 The largest contributors to the average total nitrogen *deposition fluxes* across North America in 2016 were
1830 wet ammonium ion, dry HNO_3 , wet nitrate ion, dry particle ammonium, dry ammonia gas, dry particle
1831 nitrate and dry NO_2 , with relatively minor contributions from the other depositing gases. The largest
1832 contributors to the average total N deposition flux *variability* across models in descending order of
1833 importance were the deposition of dry particulate ammonium, wet ammonium ion, wet nitrate ion, dry
1834 nitric acid, dry particle nitrate, dry NO_2 and dry NH_3 .

1835 The first and second contributions to model-to-model variability between the members of the reduced
1836 North American ensemble were due to the three GEM-MACH implementations (Base, Zhang, and Ops)
1837 all having much higher dry particle ammonium and wet ammonium ion deposition fluxes than the other



1838 models. These models also had zero to positive biases in wet ammonium ion deposition relative to
1839 observations during the summer (all other models had negative biases throughout the year), and the
1840 largest positive biases for PM_{2.5} ammonium concentrations relative to observations. These three models
1841 employed an inorganic aerosol thermodynamics algorithm solving only the sulphate-ammonium-nitrate-
1842 water system, while the other models in the ensemble employed a solver which incorporated base cation
1843 chemistry. The presence of base cations is known to be a limiting factor on the formation of particle
1844 ammonium nitrate, with the available nitric acid preferentially partitioning to the base cations over
1845 forming particle ammonium nitrate. The positive biases in fine mode particle ammonium concentrations
1846 and positive biases in wet ammonium ion deposition for this subgroup of models are thus likely caused by
1847 the absence of this alternative sink of nitric acid, leaving only the particle ammonium formation pathway.
1848 This in turn led to higher predicted concentrations of particle ammonium, subsequent particle ammonium
1849 scavenging in clouds, and greater wet ammonium deposition in these models. Updates to these model
1850 implementations making use of a new, highly efficient solver for inorganic heterogeneous chemistry
1851 which includes the base cation reactions (Miller *et al.*, 2024) should reduce these positive biases. The
1852 absence of multiphase hydrometeor scavenging of particle mass may also play a role in the particle
1853 ammonium positive biases for these models, with improved performance associated with the
1854 incorporation of this more detailed wet scavenging approach (Ghahreman *et al.*, 2024). We note that all
1855 North American models had negative biases in wet ammonium and wet nitrate deposition, indicating
1856 insufficient uptake of gas and particle precursors into cloud and precipitation water, possibly due to the
1857 absence of multiphase hydrometeor scavenging in all models participating in the ensemble.

1858 Dry deposition of nitric acid was the second largest contributor to total nitrogen deposition fluxes in
1859 North America, and the fourth largest contributor to model-to-model variability. The cuticle deposition
1860 pathway followed by the soil pathway were shown to dominate the HNO₃ mass flux, usually by more than
1861 an order of magnitude. While effective fluxes include potential changes due to other terms such as
1862 chemical production, cuticle values also dominate for the effective conductances – deposition velocity is a
1863 key term affecting HNO₃ concentrations near the surface.

1864 Comparisons of model-predicted 2016 concentrations of NH₃(g) to both CrIS satellite-based observations
1865 (in the afternoon, at overpass time) and ground-based AMON monitoring network values (biweekly
1866 averages) showed that CMAQ-M3Dry and CMAQ-STAGE had the most negative biases in NH₃. These
1867 models, employ two different bidirectional flux algorithms for NH₃ emissions and deposition. The GEM-
1868 MACH (Base) and GEM-MACH (Zhang) models (both of which employed a common bidirectional flux
1869 algorithm) had the smallest magnitude NH₃ biases. A detailed analysis of the magnitude and direction of
1870 the bidirectional flux models showed a common diurnal behaviour of daytime emissions from agricultural
1871 and grassland areas and deposition in downwind forested areas, and nighttime deposition in all regions.
1872 However, the GEM-MACH models predicted low magnitude net emissions from forested areas
1873 downwind of agricultural areas in the early morning, while the CMAQ models predicted net deposition at
1874 all locations. Differences in the relative magnitudes of compensation point concentrations and the
1875 strength of the daytime stomatal deposition pathway were shown to be the cause for these differences.

1876 *Europe, Critical Load Exceedances*

1877 The AQMEII4 ensemble for Europe predicted similar exceedances with respect to acidity and
1878 eutrophication in 2009 and 2010, with the 3-member reduced ensemble showing slightly reduced
1879 exceedance levels for acidity, and slightly increased exceedance levels for eutrophication, in 2010. The
1880 EU percent reduced ensemble acidification exceedance and its range was 4.48% (range 2.37% to 6.85%)
1881 in 2009, and 4.32% (range 2.06% to 6.52%) in 2010. EU eutrophication exceedance areas were higher, at
1882 60.2% (range 47.3% to 73.3%) in 2009, and 62.2% (range 51.2% to 74) in 2010 .



1883 We note that the models used made use of inorganic aerosol thermodynamics algorithms which included
1884 reactions of base cations, and none made use of more recent updates to the particle dry deposition
1885 parameterization (Emerson *et al.*, 2020, Pleim *et al.*, 2022). Consequently, the magnitude of differences
1886 between the models varied from the North American models, as well as the order of importance of
1887 different forms of Sulphur towards total deposition differed from the North American ensemble.

1888 *Europe, Causes of Model S Deposition Variability*

1889 The common domain average reduced ensemble sulphur dry deposition contributions and their variability
1890 followed the same order (SO₂: 56.7%; range 47.0% to 61.4%, Wet S: 37.2%; range 34.3% to 46.4%, dry
1891 particulate sulphate: 6.0%; range 1.9 to 9.0%). WRF-Chem (IASS) had the best overall performance
1892 relative to observations for SO₂ concentrations, while CMAQ (Hertfordshire) had the best performance
1893 for wet S deposition. LOTOS-EUROS (TNO) and CMAQ (Hertfordshire) tended to overestimate
1894 regional SO₂ seasonality, with much higher concentrations in winter than summer compared to
1895 observations in the EMEP SO₂ network. Near-source observations (AIRBASE network) had higher
1896 winter than summer values, though this seasonal variation was largely absent in the observations for
1897 stations more representative of regional conditions (EMEP). The positive biases in modelled regional
1898 SO₂ concentrations for LOTOS-EUROS (TNO) and CMAQ (Hertfordshire) (the latter relative to both
1899 EMEP and AIRBASE stations) may reflect differences in plume rise distribution between the models, or
1900 in their driving meteorology's vertical stability (e.g. the modelled wintertime atmosphere may be more
1901 stable than is observed, for these models). As was the case in the North America ensemble, all models
1902 had negative biases for wet S deposition. CMAQ (Hertfordshire), with the best overall wet S deposition
1903 performance, nevertheless had a 2010 bias of -0.39 eq ha⁻¹ yr⁻¹. This may be compared to the monthly
1904 observed values which ranged from 1.0 to 1.95 eq ha⁻¹ yr⁻¹). As in North America, the manner in which
1905 cloud scavenging of particulate sulphate and SO₂ was implemented in these models may be the cause of
1906 the wet deposition negative biases. Unlike North America, speciated PM measurements were unavailable
1907 for model evaluation.

1908 EU SO₂ deposition pathways were investigated with AQMEII4 diagnostics; the soil and cuticle pathways
1909 dominated, though their relative importance varied between reporting models. The stomatal pathway was
1910 relatively unimportant (e.g., the cuticle pathway flux was approximately an order of magnitude higher
1911 than the stomatal pathway for the three models reporting these data). This order of importance may
1912 reflect diurnal and seasonal SO₂ concentration variations. SO₂ concentrations are more likely to be high
1913 under more stable atmospheric conditions (these inhibit the rise of buoyant SO₂ plumes from large stack
1914 sources); these conditions are more likely to occur more frequently at night and in the winter, when the
1915 influence of the stomatal pathway is at its minimum.

1916 *Europe, Causes of Model N Deposition Variability*

1917 The relative contributions towards total N deposition and the range in the EU domain were: wet nitrate
1918 ion (30.9%; range 22.7% to 31.5%), dry HNO₃ (21.0%; range 11.2 to 25.8%), wet ammonium ion
1919 (20.3%; range 15.5% to 26.4%), dry ammonia gas (13.7%; range 9.7% to 22.4%), dry particle nitrate
1920 (5.1%; range 4.4% to 5.4%), and dry NO₂ (5.1%; range 2.1% to 6.9%). The variations in the N deposition
1921 values between models were smaller than in North America, likely due to the use of base cation-inclusive
1922 inorganic aerosol thermodynamic algorithms in all models, and the use of older implementations of wet
1923 scavenging and particle dry deposition than in the North American models. We note that dry NH₃
1924 deposition was the 4th largest contributor to European N deposition model-to-model variability, with the
1925 model employing a bidirectional flux algorithm (LOTOS-EUROS) having the highest NH₃ deposition.
1926 While monitoring network and satellite NH₃ observations for the time periods simulated were not



1927 available for Europe, the latter data source should be used in simulations in subsequent years for
1928 evaluation of European model NH₃ performance.

1929 LOTOS-EUROS (TNO) had the best overall performance for wet nitrate deposition, wet ammonium
1930 deposition, and near source NO₂ concentrations compared to the other models. However, wet nitrate and
1931 ammonium deposition had substantial negative biases for all models, in common with the North
1932 American models. The seasonality of wet N deposition was poorly simulated, with most models failing to
1933 predict the observed summertime maximum of wet ammonium deposition. Given that this negative bias
1934 has its maximum in the summer, when agricultural NH₃ emissions are also likely to maximize, evaluation
1935 in more recent years of NH₃ predictions against satellite data is recommended.

1936 Two models for the EU comparison (WRF-Chem (UPM) and CMAQ (Hertfordshire)) reported effective
1937 flux diagnostics for all four HNO₃ dry deposition effective flux pathways: these models showed a similar
1938 result to North America, with cuticle and soil pathways being approximately an order of magnitude higher
1939 than the stomatal and (when present) the lower canopy pathways.

1940 We also note that the importance of the details of the underlying land-use database may be seen in the
1941 HNO₃ deposition flux diagnostics (Figures S17 and S18). The effective flux values are with respect to
1942 land (vegetated) regions (i.e. the relative importance of stomatal, cuticle, lower canopy and soil pathways
1943 is only relevant on land). Here, a >1% water was used as an exclusion criterion to allow a comparison
1944 between grid cells that were “mostly land”. In these Figures, the regions which do not meet this exclusion
1945 criterion are represented as grey areas. Some models clearly have a greater fraction of inland water
1946 (possibly at low land use fractions) than others in boreal forest areas, from the relative proportion of grey
1947 “no land” grid cells in these Figures (NA: (CMAQ-M3Dry, CMAQ-STAGE, GEM-MACH (Base), GEM-
1948 MACH (Zhang), GEM-MACH (Ops)) have more grey regions than (WRF-Chem (IASS), WRF-Chem
1949 (UPM), WRF-Chem (UCAR)); EU: CMAQ (Hertfordshire) has more grey regions than the other three
1950 models). Furthermore, we note that the land-use databases employed in critical load exceedance
1951 calculations may *also* differ from those used in individual models. Such mismatches are another source
1952 of uncertainty in the estimation the critical load exceedances for the dry deposition portions of total S and
1953 N deposition. The effect of land-use type classifications on model deposition fluxes for ozone will be
1954 examined in more detail in a companion paper (Hogrefe *et al.*, 2024, ACPD, in preparation).

1955 *Recommendations: Air-Quality Modelling Needs Identified by the Analysis*

1956 Our analysis suggests that model biases and model-to-model variability may be reduced through targeted
1957 research into specific model process components. These include:

1958 *Multiphase hydrometeor scavenging of gases and aerosols into clouds:* Wet deposition was usually the
1959 largest or second largest source of total S and N deposition in both ensembles for Europe and North
1960 America, however, every model in the two ensembles had negative biases for wet deposition. The portion
1961 of critical load exceedances associated with wet deposition has been underestimated, due to this model
1962 bias. Improvements in the process representation of cloud processing of S- and N-containing particles
1963 and gases is thus a priority for research. Recent papers indicate that multiphase hydrometeor scavenging
1964 implementations may reduce this bias.

1965 *Incorporation of improved particle deposition velocity algorithms – but only in combination with*
1966 *multiphase wet scavenging.* Most of the models and model simulations employed in the AQMEII4
1967 ensemble did not make use of the more recent algorithms for particle dry deposition based on an
1968 exhaustive review of available deposition observations in a variety of land use types (Emerson *et al.*,
1969 2020). However, the models which *did* incorporate these algorithms (GEM-MACH (Base), GEM-MACH



1970 (Zhang)) had substantially increased positive biases in fine mode particulate matter concentrations. An
1971 algorithm known to result in a better fit to observed *deposition velocities* thus resulted in worse *regional*
1972 *model* performance – suggesting that other factors and compensating errors in the modelling platforms
1973 may be influencing performance in the model implementations examined here.

1974 Recent work by Ryu and Min (2022) and Ghahreman *et al.* (2024) suggest that the above two issues
1975 (positive particle concentration biases and negative wet deposition flux biases) are related, and that a
1976 *combination* of particle dry deposition updates and multiphase hydrometeor wet scavenging may be
1977 required to generate a net improvement in model performance. Ryu and Min (2022) demonstrated using
1978 the WRF-Chem model that when the dry deposition updates are implemented alone, a similar effect on
1979 particulate concentrations was seen as for GEM-MACH in the current study – an increase in positive
1980 PM_{2.5} biases relative to observations. They also showed that the implementation of multiphase
1981 scavenging alone also decreased WRF-Chem performance, while simultaneously implementing both
1982 particle dry deposition velocity updates and multiphase scavenging resulted in a net improvement in
1983 performance of that model. Ghahreman *et al.* (2024) added multiphase hydrometeor scavenging to a
1984 GEM-MACH implementation incorporating the Emerson *et al.* (2020) particle dry deposition velocity
1985 updates, and showed significant improvements in sulphate fluxes relative to earlier model
1986 implementations. The need for a combined approach for these process updates is supported by the current
1987 work.

1988 *Base cation inorganic chemistry and improved base cation emissions inventory development.* A striking
1989 cause of differences between NA GEM-MACH (Base), GEM-MACH (Zhang), and GEM-MACH (Ops)
1990 in comparison to the other models were their positive biases for fine model particle nitrate and ammonium
1991 concentrations relative to observations. Unlike the other models in both ensembles, these models
1992 employed an inorganic aerosol thermodynamics algorithm which did not include base cation chemistry,
1993 and hence some of the excess fine mode particle nitrate and ammonium concentrations and fluxes may be
1994 due to the absence of coarse mode formation of base cation nitrates, allowing excessive fine mode particle
1995 ammonium and nitrate formation. Updating these models to include base cation chemistry using more
1996 recent (Fountoukis and Nenes, 2007) and highly computationally efficient/accurate algorithms now
1997 incorporated into GEM-MACH and GEOS-Chem (Miller *et al.*, 2024) should reduce these biases and
1998 overall ensemble variability.

1999 *NH₃ bidirectional fluxes.* The comparison to both surface and satellite observations for the North
2000 American ensemble models showed the potential of these algorithms to improve nitrogen deposition
2001 performance. However, the comparison also suggested that the compensation point concentrations and
2002 stomatal pathway parameterization choices for forested areas in the models compared here may have led
2003 to reduced performance in these CMAQ implementations. The balance between NH₃ emissions and
2004 deposition for this group of models in forested regions may overestimate the relative importance of
2005 deposition fluxes; a reexamination of forest stomatal pathway algorithms and compensation point
2006 concentrations for forested regions may improve the performance of this group of models. We also note
2007 that ambiguities exist in the methodology for accounting for the influence of bidirectional NH₃ fluxes
2008 towards net nitrogen deposition – this is a task for resolution by both the atmospheric modelling and
2009 critical load data communities. Furthermore, comparisons of North America regional model simulations
2010 of NH₃ with satellite data suggest that oceanic NH₃ emissions, which are included in global chemical
2011 transport modelling platforms, should also be considered for regional modelling platforms, due to
2012 negative biases observed over oceans in the simulations taking place here.

2013 *Land use type harmonization.* We note here that the databases used for land use classification may differ
2014 between models, and between the land use databases used for air-quality model simulations and those



2015 used for critical load data generation; these factors influenced the simulated NH₃ fluxes shown above, and
2016 are the subject of a separate AQMEII4 paper analyzing model O₃ deposition performance (Hogrefe *et al.*,
2017 2024, in preparation). Future work centered on harmonizing the land use classification data used for
2018 models, and between models and those used in critical load estimates, is therefore recommended.

2019 *Disclaimer: The views expressed in this article are those of the authors and do not necessarily represent*
2020 *the views or policies of the U.S. Environmental Protection Agency.*

2021 *Competing Interests: At least one of the co-authors is a member of the editorial board of Atmospheric*
2022 *Chemistry and Physics*

2023 *Author Contributions:* PAM: study design and analysis, manuscript writing, GEM-MACH simulations,
2024 generation of figures, tables. PC: study analysis support, generation of figures, tables. CH: coordination
2025 of modelling team, CMAQ-M3Dry, CMAQ-STAGE simulations, manuscript writing, analysis checking
2026 and verification. AA: GEM-MACH simulations. UA: WRF-Chem(IASS) simulations, comments on
2027 manuscript. JOB: CMAQ-STAGE (EPA) simulations, comments on manuscript. MDB: Critical load
2028 exceedance generation from model output; US critical loads for lichen and herbaceous community
2029 richness. RB: ENSEMBLE system for submission of model output, coordination of model output library.
2030 RB: ENSEMBLE system for submission of model output, coordination of model output library. T.
2031 Butler: WRF-Chem (IASS) simulations. HC: North American critical load exceedance generation for
2032 aquatic and forest ecosystems, comments on manuscript. OEC: comments on manuscript. AH: WRF-
2033 Chem (UCAR) simulations, comments on manuscript. IK: comments on manuscript, discussions on
2034 observation data. RK: LOTOS-EUROS simulations. AL: WRF-Chem (IASS) simulations, comments on
2035 paper. JAL: US aquatic ecosystem critical loads, contributions to North American critical load
2036 exceedances. KM: WRF-Chem (IASS) simulations. JLPC: WRF-Chem (UPM) simulations. JP:
2037 CMAQ-M3Dry simulations. YHR: WRF-Chem (UCAR) simulations, comments on manuscript. RSJ:
2038 WRF-Chem (UPM) simulations, reanalysis of WRF-Chem output. DS: Discussions on initial AQMEII4
2039 work, including the work described in this manuscript. TS: European critical load exceedance analysis,
2040 design of common format for critical load exceedance bar charts, comments on the manuscript. RSS:
2041 CMAQ(Hertfordshire) simulations, comments on manuscript. SG: ENSEMBLE model output
2042 submission system coordination, co-chairing regular meetings at which the manuscript was discussed.
2043 PAM, CH, OEC, DS, SG: AQMEII4 steering committee coordination, manuscript discussion.

2044 References

- 2045 Abdul-Razzak, H. and Ghan, S.J.. A parameterization of aerosol activation: 2. Multiple aerosol types. J.
2046 Geophys. Res. Atm., 105, 6837-6844, 2000. <https://doi.org/10.1029/1999JD901161>
- 2047 Aherne, J., & Jeffries, D., Critical Load Assessments and Dynamic WRF-Chem (IASS) applications for
2048 Lakes in North America. In W. de Vries, J.-P. Hettelingh, & M. Posch (Eds.), Critical Loads and
2049 Dynamic Risk Assessments: Nitrogen, Acidity and Metals in Terrestrial and Aquatic Ecosystems
2050 (pp. 485–503). Springer Netherlands., 2015. https://doi.org/10.1007/978-94-017-9508-1_19
- 2051 Akingunola, A., Makar, P.A., Zhang, J., Darlington, A., Li, S.-M., Gordon, M., Moran, M.D., and Zheng,
2052 Q., A chemical transport model study of plume-rise and particle size distribution for the
2053 Athabasca oil sands, Atmos. Chem. Phys., 18, 8667–8688, 2018. [https://doi.org/10.5194/acp-18-](https://doi.org/10.5194/acp-18-8667-2018)
2054 [8667-2018](https://doi.org/10.5194/acp-18-8667-2018)
- 2055 AMoN, 2024: <https://nadp2.slh.wisc.edu/data/AMoN/>, with data downloaded from
2056 <https://nadp2.slh.wisc.edu/dataLib/AMoN/csv/all-rep.csv>, and metadata available at
2057 https://nadp.slh.wisc.edu/wp-content/uploads/2022/08/amon_metadata_v2.pdf



2058 Anderson, J., Hardy, E., Roach, J., and Witmer, R., A land use and land cover classification system for
2059 use with remote sensor data. U.S. Geological Survey, Geological survey professional paper 96,
2060 1976. <https://pubs.usgs.gov/publication/pp964>
2061 Anlauf, K., Li, S.-M., Leaitch, R., Brook, J., Hayden, K., Toom-Sauntry, D., Wiebe, A., Ionic
2062 composition and size characteristics of particles in the Lower Fraser Valley: Pacific 2001 field
2063 study, *Atm. Env.*, 40, 2662-2675, 2006. <https://doi.org/10.1016/j.atmosenv.2005.12.027>
2064 Appel, K. W., Bash, J.O., Fahey, K.M., Foley, K.M., Gilliam, R.C., Hogrefe, C., Hutzell, W.T., Kang, D.,
2065 Mathur, R., Murphy, B.N., Napelenok, S.L., Nolte, C.G., Pleim, J.E., Pouliot, G.A., Pye, H.O.T.,
2066 Ran, L., Roselle, S.J., Sarwar, G., Schwede, D.B., Sidi, F.I., Spero, T.L., and Wong, D. C., The
2067 Community Multiscale Air Quality (CMAQ) model versions 5.3 and 5.3.1: system updates and
2068 evaluation, *Geosci. CMAQ (Hertfordshire)ev.*, 14, 2867–2897, 202.
2069 <https://doi.org/10.5194/gmd-14-2867-2021>
2070 Banzhaf, S., Schaap, M., Kerschbaumer, A., Reimer, E., Stern, R., Van Der Swaluw, E., Bultjes, P.,
2071 Implementation and evaluation of pH-dependent cloud chemistry and wetdeposition in the
2072 chemical transport model REM-Calgrid, *Atmos. Environ.*, 49, 378-390, 2012.
2073 <https://doi.org/10.1016/j.atmosenv.2011.10.069>
2074 Bash, J. O., Cooter, E. J., Dennis, R. L., Walker, J. T., & Pleim, J. E., Evaluation of a regional air-quality
2075 model with bidirectional NH₃ exchange coupled to an agroecosystem
2076 model. *Biogeosciences*, 10(3), 1635–1645, 2013. <https://doi.org/10.5194/bg-10-1635-2013>
2077 Belair, S., Brown, R., Mailhot, J., Bilodeau, B., Crevier, L.-P., Operational implementation of the ISBA
2078 land surface scheme in the Canadian regional weather forecast model. Part II: cold season results.
2079 *J. Hydrometeor.* 4, 371-386, 2003b. [https://doi.org/10.1175/1525-](https://doi.org/10.1175/1525-7541(2003)4<371:OIOTIL>2.0.CO;2)
2080 [7541\(2003\)4<371:OIOTIL>2.0.CO;2](https://doi.org/10.1175/1525-7541(2003)4<371:OIOTIL>2.0.CO;2)
2081 Belair, S., Crevier, L.-P., Mailhot, J., Bilodeau, B., Delage, Y., Operational implementation of the ISBA
2082 land surface scheme in the Canadian regional weather forecast model. Part I: warm season results.
2083 *J. Hydrometeor.* 4, 352-370, 2003a. [https://doi.org/10.1175/1525-](https://doi.org/10.1175/1525-7541(2003)4<352:OIOTIL>2.0.CO;2)
2084 [7541\(2003\)4<352:OIOTIL>2.0.CO;2](https://doi.org/10.1175/1525-7541(2003)4<352:OIOTIL>2.0.CO;2)
2085 Bermejo, R., and Conde, J., A conservative quasi-monotone semi-Lagrangian scheme, *Mon. Wea. Rev.*,
2086 130, 423-430, 2002. [https://doi.org/10.1175/1520-0493\(2002\)130<0423:ACQMSL>2.0.CO;2](https://doi.org/10.1175/1520-0493(2002)130<0423:ACQMSL>2.0.CO;2)
2087 Binkowski F.S., and Roselle, S.J., Models-3 Community Multiscale Air Quality(CMAQ) model aerosol
2088 component I. Model description, *J. Geophys. Res.* 108, No. D6, 4183, 18pp, 2003.
2089 <https://doi.org/10.1029/2001JD001409>
2090 Binkowski, F.S., and Shankar, U., The Regional Particulate Matter Model: 1. Model description and
2091 preliminary results, *J. Geophys. Res.*, 100, no D12, 26,191-26,209, 1995.
2092 <https://doi.org/10.1029/95JD02093>
2093 Bobbink, R., Loran, C., Tomassen, H. (2022). Review and revision of empirical critical loads of nitrogen
2094 for Europe. Dessau-Roßlau, UBA TEXTE 02/2022.
2095 <https://www.umweltbundesamt.de/en/publikationen/review-revision-of-empirical-critical-loads-of>
2096 Bower, K.N. and T.W. Choulaton, A parameterisation of the effective radius of ice free clouds for use in
2097 global climate models, *Atmospheric Research*, 27, 305-339, 1992. [https://doi.org/10.1016/0169-](https://doi.org/10.1016/0169-8095(92)90038-C)
2098 [8095\(92\)90038-C](https://doi.org/10.1016/0169-8095(92)90038-C)
2099 Briggs, G. A.: Plume rise and buoyancy effects, atmospheric sciences and power production, in:
2100 DOE/TIC-27601 (DE84005177), edited by: Randerson, D., TN, Technical Information Center,
2101 U.S. Dept. of Energy, Oak Ridge, USA, 327–366, 1984
2102 Carter, W.P.L., Development of the SAPRC-07 chemical mechanism, *Atm. Env.*, 44, 5324-5335, 2010.
2103 <https://doi.org/10.1016/j.atmosenv.2010.01.026>
2104 Cathcart, H., Aherne, J., Jeffries, D. S., & Scott, K. A., Critical loads of acidity for 90,000 lakes in
2105 northern Saskatchewan: A novel approach for mapping regional sensitivity to acidic deposition.
2106 *Atm. Env.*, 146, 290–299, 2016. <https://doi.org/10.1016/j.atmosenv.2016.08.048>
2107 Chapman, E. G., Gustafson Jr., W. I., Easter, R. C., Bamard, J. C., Ghan, S. J., Pekour, M. S., and Fast, J.
2108 D., Coupling aerosol-cloud-radiative processes in the WRF-Chem model: Investigating the



- 2109 radiative impact of elevated point sources, *Atmos. Chem. Phys.*, 9, 945–964, 2009.
2110 <https://doi.org/10.5194/acp-9-945-2009>
- 2111 Chaumerliac, N., Evaluation des Termes de Captation Dynamique dans un Modele Tridimensionel a`
2112 Mesoechelle de Lessivage de L'Atmo-sphere, thesis, Univ. de Clermont II, U.E.R. de Rech. Sci.
2113 et Tech., 1984.
- 2114 Chen, X., Day, D., Schichtel, B., Malm, W., Matzoll, A.K., Mjica, J., McDade, C.E., Hardison, E.D.,
2115 Hardison, D.L., Walters, S., Van De Water, M., Collett, J.L. Jr., Seasonal ambient ammonia and
2116 ammonium concentrations in a pilot IMPROVE NHx monitoring network in the western United
2117 States, *Atm. Env.*, 91, 118–126, 2104.
- 2118 Clifton, O. E., Fiore, A. M., Massman, W. J., Baublitz, C. B., Coyle, M., Emberson, L., Fares, S., Farmer,
2119 D. K., Gentine, P., Gerosa, G, Guenther, A. B., Helmig, D., Lombardozzi, D. L., Munger, J. W.,
2120 Patton, E. G., Pusede, S. E., Schwede, D. B., Silva, S. J., Sörgel, M., Steiner, A. L., and Tai, A. P.
2121 K.: Dry deposition of ozone over land: processes, measurement, and modeling, *Rev. Geophys.*,
2122 58, e2019RG000670, 62pp., 2020a. <https://doi.org/10.1029/2019RG000670>
- 2123 Clifton, O. E., Fiore, A. M., Munger, J. W., Malyshev, S., Horowitz, L. W., Shevliakova, E., Paulot, F.,
2124 Murray, L. T., and Griffin, K. L.: Interannual variability in ozone removal by a temperate
2125 deciduous forest, *Geophys. Res. Lett.*, 44, 542–552, 2017.
2126 <https://doi.org/10.1002/2016GL070923>
- 2127 Clifton, O. E., Paulot, F., Fiore, A. M., Horowitz, L. W., Correa, G., Baublitz, C. B., Fares, S., Goded, I.,
2128 Goldstein, A. H., Gruening, C., Hogg, A. J., Loubet, B., Mammarella, I., Munger, J. W., Neil, L.,
2129 Stella, P., Uddling, J., Vesala T., and Weng, E.: Influence of dynamic ozone dry deposition on
2130 ozone pollution, *J. Geophys. Res.-Atmos.*, 125, e2020JD032398, 2020b.
2131 <https://doi.org/10.1029/2020JD032398>
- 2132 Clifton, O.E., Schwede, D., Hogrefe, C., Bash, J.O., Bland, S., Cheung, P., Coyle, M., Emberson, L.,
2133 Flemming, J., Fredj., E., Galmarini, S., Ganzeveld, L., Gazetas, O., Goded, I., Holmes, C.D.,
2134 Horváth, L., Huijnen, V., Li, Q., Makar, P.A., Mammarella, I., Manca, G., Munger, J.W., Pérez-
2135 Camanyo, J.L., Pleim, J., Ran, L., San Jose, R., Silva, S.J., Staebler, R., Sun, S., Tai, A.P.K, Tas,
2136 E., Vesala, T., Weidinger, T., Wu, Z. and Zhang, L., A single-point modeling approach for the
2137 intercomparison and evaluation of ozone dry deposition across chemical transport models
2138 (Activity 2 of AQMEII4), *Atmos. Chem. Phys.*, 23, 9911–9961, 2023.
2139 <https://acp.copernicus.org/articles/23/9911/2023/>
- 2140 Clifton, O.E., Bauer, S.E., Tsigaridis, K., Aleinov, I., Cowan, T.G., Faluvegi, G., and Kelley, M.,
2141 Influence of more mechanistic representation of particle dry deposition on 1850–2000 changes in
2142 global aerosol burdens and radiative forcing, *J. Adv. Mod. Earth Systems*, 16, e2023MS003952,
2143 19 pp., 2024. <https://doi.org/10.1029/2023MS003952>
- 2144 CLRTAP, 2023: UNECE CLRTAP (2023). Manual on Methodologies and Criteria for Modelling and
2145 Mapping Critical Loads and Levels and Air Pollution Effects, Risks, and Trends. Dessau-Roßlau,
2146 UBA TEXTE 109/2023. [https://www.umweltbundesamt.de/en/publikationen/manual-on-](https://www.umweltbundesamt.de/en/publikationen/manual-on-methodologies-criteria-for-modelling-0)
2147 [methodologies-criteria-for-modelling-0](https://www.umweltbundesamt.de/en/publikationen/manual-on-methodologies-criteria-for-modelling-0)
- 2148 Côté, J., Gravel, S., Méthot, A., Patoine, A., Roch, M., and Staniforth, A.: The operational CMC/MRB
2149 global environmental multiscale (GEM) model. Part 1: design considerations and formulation,
2150 *Mon. Weather Rev.*, 126, 1373–1395, 1998. [https://doi.org/10.1175/1520-](https://doi.org/10.1175/1520-0493(1998)126<1373:TOCMGE>2.0.CO;2)
2151 [0493\(1998\)126<1373:TOCMGE>2.0.CO;2](https://doi.org/10.1175/1520-0493(1998)126<1373:TOCMGE>2.0.CO;2)
- 2152 Daly, C., Halbleib, M., Smith, J.I., Gibson, W.P., Doggett, M.K., Taylor, G.H., Curtis, J., Pasteris, P.P.,
2153 Physiographically sensitive mapping of climatological temperature and precipitation across the
2154 conterminous United States, *Int. J. Climatol.*, 2031–2064, 2008.
2155 <https://rmets.onlinelibrary.wiley.com/doi/10.1002/joc.1688>
- 2156 de Vries, W., Hettelingh, J.-P., and Posch, M.: Critical Loads and Dynamic Risk Assessments: Nitrogen,
2157 Acidity and Metals in Terrestrial and Aquatic Ecosystems, Springer, Dordrecht, Netherlands, 647
2158 pp., 2015. <https://link.springer.com/book/10.1007/978-94-017-9508-1>



- 2159 Dewitz, J., National Land Cover Database (NLCD) 2019 Products (ver. 2.0, June 2021). U.S. Geological
2160 Survey. 2021 <https://doi.org/10.5066/P9KZCM54>
- 2161 Dupont, J., Clair, T. A., Gagnon, C., Jeffries, D. S., Kahl, J. S., Nelson, S. J., & Peckenham, J. M.,
2162 Estimation of Critical Loads of Acidity for Lakes in Northeastern United States and Eastern
2163 Canada. *Environmental Monitoring and Assessment*, 109(1–3), 275–292, 2005.
2164 <https://doi.org/10.1007/s10661-005-6286-x>
- 2165 Easter, R.C., Ghan, S.J., Zhang, Y., Saylor, R.D., Chapman, E.G., Laulainen, N.S., Abdul-Razzak, H.,
2166 Leung, L.R., Bian, X., Zaveri, R.A., 2004. MIRAGE: Model description and evaluation of
2167 aerosols and trace gases. *Journal of Geophysical Research*, 109, 46 pp., 2004.
2168 <https://doi.org/10.1029/2004JD004571>
- 2169 EEA 2000: CORINE Land Cover 2000, [https://trac.osgeo.org/geonetwork/raw-](https://trac.osgeo.org/geonetwork/raw-attachment/ticket/650/GeoNetwork-chrome-simple.pdf)
2170 [attachment/ticket/650/GeoNetwork-chrome-simple.pdf](https://trac.osgeo.org/geonetwork/raw-attachment/ticket/650/GeoNetwork-chrome-simple.pdf), Last accessed December 26, 2023.
- 2171 EEA: CLC2006 technical guidelines. EEA Technical report 17/2007. ISBN 978-92-9167-968-3,
2172 https://www.eea.europa.eu/ds_resolveuid/6ee7e1406e694f6adacf6cd349aff89a , 2007.
- 2173 Emerson, E.W., Hodshire, A.L., DeBolt, H.M., Bilsback, K.R., Pierce, J.R., McMeeking, G.R., and
2174 Farmer, D.K., Revisiting particle dry deposition and its role in radiative effect estimates, *Proc.*
2175 *Nat. Acad. Sci.*, 117, 26076–26082, 2020. www.pnas.org/cgi/doi/10.1073/pnas.2014761117
- 2176 Emmons, L. K., Walters, S., Hess, P. G., Lamarque, J.-F., Pfister, G. G., Fillmore, D., Granier, C.,
2177 Guenther, A., Kinnison, D., Laepple, T., Orlando, J., Tie, X., Tyndall, G., Wiedinmyer, C.,
2178 Baughcum, S. L., and Kloster, S.: Description and evaluation of the Model for Ozone and Related
2179 chemical Tracers, version 4 (MOZART-4), *Geosci. CMAQ (Hertfordshire)ev.*, 3, 43–67, 2010.
2180 <https://doi.org/10.5194/gmd-3-43-2010>
- 2181 Fahey, K.M., Carlton, A.G., Pye, H.O.T., Baeka, J., Hutzell, W.T., Stanier, C.O., Baker, K.R., Appel,
2182 K.W., Jaoui, M. and Offenberg, J.H., A framework for expanding aqueous chemistry in the
2183 Community Multiscale Air Quality (CMAQ) model version 5.1, *Geosci. CMAQ*
2184 *(Hertfordshire)ev.*, 10, 1587–1605, 2017. <https://doi.org/10.5194/gmd-10-1587-2017>
- 2185 Fakhraei, H.A., Driscoll, C.T., Selvendiran, P., DePinto, J.V., Bloomfield, J., Quinn, S. and Rowell, H.C.,
2186 Development of a total maximum daily load (TMDL) for acid-impaired lakes in the Adirondack
2187 region of New York, *Atm. Env.*, 95, 277–287, 2014.
2188 <https://doi.org/10.1016/j.atmosenv.2014.06.039>
- 2189 Fast, J. D.: Coupling aerosol-cloud-radiative processes in the WRF-Chem model: Investigating the
2190 radiative impact of elevated point sources, *Atmos. Chem. Phys.*, 9, 945–964, 2009.
2191 <https://doi.org/10.5194/acp-9-945-2009>
- 2192 Friedl, M.A., Sulla-Menashe, D., Tan, B., Schneider, A., Ramankutty, N., Sibley, A., Huang, X., MODIS
2193 Collection 5 global land cover: Algorithm refinements and characterization of new datasets,
2194 *Remote Sensing of Environment*, 114, 168–182, 2010. <https://doi.org/10.1016/j.rse.2009.08.016>
- 2195 Fountoukis, C. and Nenes, A., ISORROPIAII: a computationally efficient thermodynamic equilibrium
2196 model for K^+ - Ca^{2+} - Mg^{2+} - NH_4^+ - Na^+ - SO_4^{2-} - NO_3^- - Cl^- - H_2O aerosols. *Atmos. Chem. Phys.*, 7, 4639–
2197 4659, 2007. <https://doi.org/10.5194/acp-7-4639-2007>
- 2198 Galmarini, S., Hogrefe, C., Brunner, D. Makar, P., Baklanov, A., Preface, *Atm. Env.*, 115, 340–344, 2015.
2199 <https://doi.org/10.1016/j.atmosenv.2015.06.009>
- 2200 Galmarini, S., Koffi, B., Solazzo, E., Keating, T., Hogrefe, C., Schulz, M., Benedictow, A., Griesfeller,
2201 J.J., Janssens-Maenhout, G., Carmichael, G., Fu, J., and Dentener, F., Technical note:
2202 Coordination and harmonization of the multi-scale, multi-model activities HTAP2, AQMEII3,
2203 and MICS-Asia3: simulations, emission inventories, boundary conditions, and model output
2204 formats, *Atmos. Chem. Phys.*, 17, 1543–1555, 2017. <https://doi.org/10.5194/acp-17-1543-2017>
- 2205 Galmarini, S., Makar, P., Clifton, O.E., Hogrefe, C., Bash, J.O., Bellasio, R., Bianconi, R., Beiser, J.,
2206 Butler, T., Ducker, J., Flemming, J., Hodzic, A., Holmes, C.D., Kioutsioukis, I., Kranenberg, R.,
2207 Lupascu, A., Perez-Cmarty, J.L., Pleim, J., Ryu, Y.-H., San Jose, R., Schwede, D., Silva, S., and
2208 Wolke, R., Technical note: AQMEII4 Activity 1: evaluation of wet and dry deposition schemes



- 2209 as an integral part of regional-scale air quality models, *Atmos. Chem. Phys.*, 21, 15663–15697,
2210 2021. <https://doi.org/10.5194/acp-21-15663-2021>
- 2211 Galmarini, S., Rao, S.T., and Steyn, D.G., Preface, *Atm. Env.*, 53, 1-3, 2012.
2212 <https://doi.org/10.1016/j.atmosenv.2012.03.001>
- 2213 Geiser, L. H., Nelson, P.R., Jovan, S.E., Root, H.T., and Clark, C.M., Assessing Ecological Risks from
2214 Atmospheric Deposition of Nitrogen and Sulfur to US Forests Using Epiphytic Macrolichens,
2215 *Diversity* 11(6): 87, 2019. <https://doi.org/10.3390/d11060087>
- 2216 Gery, M. W., Whitten, G. Z., Killus, J. P., and Dodge, M. C.: A photochemical kinetics mechanism for
2217 urban and regional scale computer modeling, *J. Geophys. Res.*, 94, 12925–12956, 1989.
2218 <https://doi.org/10.1029/JD094iD10p12925>
- 2219 Geupel, M., Loran, C., Scheuschner, T., and Wohlgenuth, L., CCE Status Report. Dessau-Roßlau, UBA
2220 TEXTE 135/2022, 2022. [https://www.umweltbundesamt.de/en/publikationen/cce-status-report-](https://www.umweltbundesamt.de/en/publikationen/cce-status-report-2022)
2221 [2022](https://www.umweltbundesamt.de/en/publikationen/cce-status-report-2022), last accessed December 21, 2023.
- 2222 Ghahreman, R., Gong, W., Makar, P.A., Lupu, A., Cole, A., Banwait, K., Lee, C., Akingunola, A.,
2223 Modelling below-cloud scavenging of size resolved particles in GEM-MACHv3.1, *Geo. CMAQ*
2224 (Hertfordshire)ev., 17, 685-707, 2024. <https://gmd.copernicus.org/articles/17/685/2024/>
- 2225 Gibson, J. J., Birks, J. S., Jeffries, D. S., Kumar, S., Scott, K. A., Aherne, J., & Shaw, P. D., Site-specific
2226 estimates of water yield applied in regional acid sensitivity surveys across western Canada.
2227 *Journal of Limnology*, 69(1s), 67, 2010. <https://doi.org/10.4081/jlimnol.2010.s1.67>
- 2228 Giorgi, F., A particle dry-deposition parameterization scheme for use in tracer transport models, *J.*
2229 *Geophys. Res. Atm.*, 91, 9794–9806, 1986. <https://doi.org/10.1029/JD091iD09p09794>
- 2230 Ginoux, P., Chin, M., Tegen, I., Prospero, J. M., Holben, B., Dubovik, O., & Lin, S.-J., Sources and
2231 distributions of dust aerosols simulated with the GOCART model. *Journal of Geophysical*
2232 *Research: Atmospheres*, 106(D17), 20255–20273. <https://doi.org/10.1029/2000JD000053>. 2001.
- 2233 Girard, C., Plante, A., Desgagne, M., McTaggart-Cowan, R., Cote, J., Charron, M., Gravel, S., Lee, V.,
2234 Patoine, A., Qaddouri, A., Roch, M., Spacek, L., Tanguay, M., Vaillancourt, P. A., and Zadra, A.,
2235 Staggered vertical discretization of the Canadian Environmental Multiscale (GEM) model using a
2236 coordinate of the log-hydrostatic-pressure type, *Mon. Weather Rev.*, 142, 1183–1196, 2014.
2237 <https://doi.org/10.1175/MWR-D-13-00255.1>
- 2238 Gong, S. L., Barrie, L. A., Blanchet, J.-P., von Salzen, K., Lohmann, U., Lesins, G., Spacek, L., Zhang, L.
2239 M., Girard, E., Lin, H., Leaitch, R., Leighton, H., Chylek, P., and Huang, P.: Canadian Aerosol
2240 Module: a size-segregated simulation of atmospheric aerosol processes for climate and air quality
2241 models. 1. Module development, *J. Geophys. Res.*, 108, 4007, 2003.
2242 <https://doi.org/10.1029/2001JD002002>
- 2243 Gong, S. L., Barrie, L. A., & Blanchet, J.-P., Modeling sea-salt aerosols in the atmosphere: 1. Model
2244 development. *Journal of Geophysical Research: Atmospheres*, 102(D3), 3805–3818, 1997.
2245 <https://doi.org/10.1029/96JD02953>
- 2246 Grell GA, SE Peckham, R Schmitz, and SA McKeen, G Frost, WC Skamarock, and B Eder, Fully
2247 coupled 'online' chemistry in the WRF model. *Atm. Env.*, 39, 6957-6976, 2005.
2248 <https://doi.org/10.1016/j.atmosenv.2005.04.027>
- 2249 Grell, G. A. and Devenyi, D.: A generalized approach to parameterizing convection combining ensemble
2250 and data assimilation techniques, *Geophys. Res. Lett.*, 29, 38-1–38-4, 2002.
2251 <https://doi.org/10.1029/2002GL015311>
- 2252 Grell, G.A. and Freitas, S.R., A scale and aerosol aware stochastic convective parameterization for
2253 weather and air quality modeling, *Atmos. Chem. Phys.*, 14, 5233–5250, 2014.
2254 <https://doi.org/10.5194/acp-14-5233-2014>
- 2255 Guenther, A., Karl, T., Harley, P., Wiedinmyer, C., Palmer, P. I., and Geron, C.: Estimates of global
2256 terrestrial isoprene emissions using MEGAN (Model of Emissions of Gases and Aerosols from
2257 Nature), *Atmos. Chem. Phys.*, 6, 3181–3210, 2006. <https://doi.org/10.5194/acp-6-3181-2006>



- 2258 Hardacre, C., Wild, O., and Emberson, L.: An evaluation of ozone dry deposition in global scale
2259 chemistry climate models, *Atmos. Chem. Phys.*, 15, 6419–6436, 2015.
2260 <https://doi.org/10.5194/acp15-6419-2015>
- 2261 Henriksen, A. and Posch, M., Steady-state models for calculating critical loads of acidity for surface
2262 waters, *Water Air Soil Poll.*, 375–398, 2001. <https://doi.org/10.1023/A:1011523720461>
- 2263 Henriksen, A., Dillon, P. J., & Aherne, J., *Critical loads of acidity for surface waters in south-central*
2264 *Ontario, Canada: Regional application of the Steady-State Water Chemistry (SSWC) model*, *Can.*
2265 *J. Fish. Aquat. Sci.*, 59, 9., 2002. <https://doi.org/10.1139/f02-092>
- 2266 Hogrefe, C., Bash, J.O., Pleim, J.E., Schwede, D.B., Gilliam, R.C., Foley, K.M., Appel, K.W., and
2267 Mathur, R., An analysis of CMAQ gas-phase dry deposition over North America through grid-
2268 scale and land-use-specific diagnostics in the context of AQMEII4, *Atmos. Chem. Phys.*, 23,
2269 8119–8147, 2023. <https://doi.org/10.5194/acp-23-8119-2023>
- 2270 Hogrefe, C., Galmarini, S., Solazzo, E., Bianconi, R., Bellasio, R., Liu, P., and Mathur, R.: Continental-
2271 Scale Analysis of Atmospheric Deposition Over North America and Europe Using the AQMEII
2272 Database, in: *Air Pollution Modeling and its Application XXVI, ITM 2018*, edited by: Mensink,
2273 C., Gong, W., and Hakami, A., Springer Proceedings in Complexity, Springer, Cham, 2020.
2274 https://doi.org/10.1007/978-3-030-22055-6_48
- 2275 Hong, S.Y., Noh, Y., and Dudhia, J., A new vertical diffusion package with an explicit treatment of
2276 entrainment processes, *Mon. Wea. Rev.*, 134, 2318–2341, 2006.
2277 <https://doi.org/10.1175/MWR3199.1>
- 2278 Hong, S.Y., A new stable boundary-layer mixing scheme and its impact on the simulated East Asian
2279 summer monsoon, *Q.J.R. Met. Soc.*, 136, 1481–1496, 2010. <https://doi.org/10.1002/qj.665>
- 2280 Huang, L., Zhu, Y., Zhai, H., Xue, S., Zhu, T., Shao, Y., Liu, Z., Emery, C., Yarwood, G., Wang, Y., Fu,
2281 J., Zhang, K., and Li, L., Recommendations on benchmarks for numerical air quality model
2282 applications in China – Part 1: PM_{2.5} and chemical species, *Atmos. Chem. Phys.*, 21, 2725–2743,
2283 2021. <https://doi.org/10.5194/acp-21-2725-2021>
- 2284 Hyder, P., Edwards, J.M., Allan, R.P., Hewitt, H.T., Bracegirdle, T.J., Gregory, J.M., Wood, R.A.,
2285 Meijers, A.J.S., Mulcahy, J., Field, P., Furtado, K., Bodas-Salcedo, A., Williams, K.D., Copesy,
2286 D., Josey, S.A., Liu, C., Robverts, C.D., Sanchez, C., Ridley, J., Thrope, L., Hardiman, S.C.,
2287 Mayer, M., Berry, D.I., and Belcher, S.E., Critical Southern Ocean climate model biases traced to
2288 atmospheric model cloud errors, *Nat Commun*, 9, 3625 (2018). <https://doi.org/10.1038/s41467-018-05634-2>
- 2289
- 2290 Hruska, J., Köhler, S., Laudon, H., Bishop, K., Comparison of acid/base character of organic acids in
2291 boreal zone of Sweden and mountainous regions in the Czech Republic. *Water Air Soil Pollut*
2292 (S4-2), p. 100 (in: *Acid Raing 2000, Proceedings from the 6th International Conference on Acid*
2293 *Deposition, Kenichi Satake, Ed.*), 2001. [https://link.springer.com/book/10.1007/978-94-007-](https://link.springer.com/book/10.1007/978-94-007-0810-5)
2294 [0810-5](https://link.springer.com/book/10.1007/978-94-007-0810-5)
- 2295 Iacono, M. J., J. S. Delamere, E. J. Mlawer, M. W. Shephard, S. A. Clough, and W. D. Collins, Radiative
2296 forcing by long-lived greenhouse gases: Calculations with the AER radiative transfer models. *J.*
2297 *Geophys. Res.*, 113, D13103, 2008. <https://doi.org/10.1029/2008JD009944>
- 2298 Inness, A., Ades, M., Agustí-Panareda, A., Barré, J., Benedictow, A., Blechschmidt, A.-M., Dominguez,
2299 J. J., Engelen, R., Eskes, H., Flemming, J., Huijnen, V., Jones, L., Kipling, Z., Massart, S.,
2300 Parrington, M., Peuch, V.-H., Razinger, M., Remy, S., Schulz, M., and Suttie, M.: The CAMS
2301 reanalysis of atmospheric composition, *Atmos. Chem. Phys.*, 19, 3515–3556, 2019.
2302 <https://doi.org/10.5194/acp-19-3515-2019>
- 2303 Janjić, Z.I., Nonsingular Implementation of the Mellor–Yamada Level 2.5 Scheme in the NCEP Meso
2304 model, Technical Report, National Centers for Environmental Prediction, Office Note No. 437,
2305 61 pp., 2001. <http://www.emc.ncep.noaa.gov/officenotes/newernotes/on437.pdf>
- 2306 Jeffries, D. S., Semkin, R. G., Gibson, J. J., & Wong, I., Recently surveyed lakes in northern Manitoba
2307 and Saskatchewan, Canada: Characteristics and critical loads of acidity. *Journal of Limnology*,
2308 69(1s), 45, 2010. <https://doi.org/10.4081/jlimnol.2010.s1.45>



- 2309 Kain, J. S.: The Kain–Fritsch convective parameterization: an update, *J. Appl. Meteorol.*, 43, 170–181,
2310 2004. [https://doi.org/10.1175/1520-0450\(2004\)043<0170:TKCPAU>2.0.CO;2](https://doi.org/10.1175/1520-0450(2004)043<0170:TKCPAU>2.0.CO;2)
- 2311 Kain, J.S. and Fritsch, J.M., A one-dimensional entraining/detraining plume model and its application in
2312 convective parameterizations, *J. Atmos. Sci.*, 47, 2784–2802, 1990. [https://doi.org/10.1175/1520-0469\(1990\)047<2784:AODEPM>2.0.CO;2](https://doi.org/10.1175/1520-0469(1990)047<2784:AODEPM>2.0.CO;2)
- 2313
- 2314 Knote, C., Hodzic, A., & Jimenez, J. L., The effect of dry and wet deposition of condensable vapors on
2315 secondary organic aerosols concentrations over the continental US. *Atmospheric Chemistry and*
2316 *Physics*, 15(1), 1– 18, 2015. <https://doi.org/10.5194/acp-15-1-2015>
- 2317 Knote, C., Hodzic, A., Jimenez, J. L., Volkamer, R., Orlando, J. J., Baidar, S., Brioude, J., Fast, J.,
2318 Gentner, D.R., Goldstein A.H., Hayes, P.L., Knighton, W.B., Oetjen, H., Setyan, A., Stark, H.,
2319 Thalman, R., Tyndall, G., Washenfelder, R., Waxman, E., and Zhang, Q., Simulation of semi-
2320 explicit mechanisms of SOA formation from glyoxal in aerosol in a 3-D model. *Atmospheric*
2321 *Chemistry and Physics*, 14(12), 6213– 6239, 2014. <https://doi.org/10.5194/acp-14-6213-2014>
- 2322 Lawrence, G. B., T. J. Sullivan, D. A. Burns, S. W. Bailey, B. J. Cosby, M. Dovciak, H. A. Ewing, T. C.
2323 McDonnell, R. Minocha, R. Riemann, J. Quant, K. C. Rice, J. Siemion, and K. Weathers, Acidic
2324 deposition along the Appalachian Trail corridor and its effects on acid-sensitive terrestrial and
2325 aquatic resources: Results of the Appalachian Trail MEGA-transect atmospheric deposition
2326 effects study. Natural Resource Report NPS/NRSS/ARD/NRR—2015/996. National Park
2327 Service, Fort Collins, Colorado, 2015. <https://irma.nps.gov/DataStore/Reference/Profile/2223220>
- 2328 Li, J. and Barker, H.W., A radiation algorithm with correlated k-distribution. Part I: local thermal
2329 equilibrium, *J. Atmos. Sci.*, 62, 286–309, 2005. <https://doi.org/10.1175/JAS-3396.1>
- 2330 Lien, L., Raddum, G. G., Fjellheim, A., & Henriksen, A., A critical limit for acid neutralizing capacity in
2331 Norwegian surface waters, based on new analyses of fish and invertebrate responses. *Science of*
2332 *The Total Environment*, 177(1–3), 173–193, 1996. [https://doi.org/10.1016/0048-9697\(95\)04894-4](https://doi.org/10.1016/0048-9697(95)04894-4)
- 2333
- 2334 Luecken, D.J., Yarwood, G., & Hutzell, W.H., Multipollutant of ozone, reactive nitrogen and HAPs
2335 across the continental US with CMAQ-CB6. *Atmospheric Environment*, 201, 62–72, 2019.
2336 <https://doi.org/10.1016/j.atmosenv.2018.11.060>
- 2337 Lydersen, E., Larssen, T., & Fjeld, E., The influence of total organic carbon (TOC) on the relationship
2338 between acid neutralizing capacity (ANC) and fish status in Norwegian lakes. *Science of The*
2339 *Total Environment*, 326(1), 63–69, 2004. <https://doi.org/10.1016/j.scitotenv.2003.12.005>
- 2340 Lynch, J.A., Phelan, J., Pardo, L.H., McDonnell, T.C., Clark, C.M., and Bell, M.D., Detailed
2341 Documentation of the National Critical Load Database (NCLD) for U.S. Critical Loads of Sulfur
2342 and Nitrogen, version 3.2.1, National Atmospheric Deposition Program, Wisconsin State
2343 Laboratory of Hygiene, Madison, WI., 2022.
2344 https://nadp.slh.wisc.edu/filelib/claddb/DB_Version/Documentation/NCLD_Documentation_v32.1.pdf
- 2345
- 2346 Makar, P. A., Akingunola, A., Aherne, J., Cole, A. S., Aklilu, Y.-A., Zhang, J., Wong, I., Hayden, K., Li,
2347 S.-M., Kirk, J., Scott, K., Moran, M. D., Robichaud, A., Cathcart, H., Baratzedah, P., Pabla, B.,
2348 Cheung, P., Zheng, Q., and Jeffries, D. S., Estimates of exceedances of critical loads for
2349 acidifying deposition in Alberta and Saskatchewan, *Atmos. Chem. Phys.*, 18, 9897–9927, 2018.
2350 <https://doi.org/10.5194/acp-18-9897-2018>
- 2351 Makar, P. A., Stroud, C., Akingunola, A., Zhang, J., Ren, S., Cheung, P., and Zheng, Q.: Vehicle-induced
2352 turbulence and atmospheric pollution, *Atmos. Chem. Phys.*, 21, 12291–12316, 2021.
2353 <https://doi.org/10.5194/acp-21-12291-2021>
- 2354 Makar, P., Staebler, R., Akingunola, A., Zhang, J., McLinden, C., Kharol, S.K., Pabla, B., Cheung, P.,
2355 Zheng, Q., The effects of forest canopy shading and turbulence on boundary layer ozone. *Nat*
2356 *Commun* 8, 15243, 2017. <https://doi.org/10.1038/ncomms15243>
- 2357 Makar, P.A., Gong, W., Hogrefe, C., Zhang, Y., Curci, G., Žabkar, R., Milbrandt, J., Im, U., Balzarini,
2358 A., Baró, R., Bianconi, R., Cheung, P., Forkel, R., Gravel, S., Hirtl, M., Honzak, L., Hou, A.,
2359 Jiménez-Guerrero, P., Langer, M., Moran, M.D., Pabla, B., Pérez, J.L., Pirovano, G., San José,



- 2360 R., Tuccella, P., Werhahn, J., Zhang, J., Galmarini, S., Feedbacks between air pollution and
2361 weather, part 2: Effects on chemistry, *Atm. Env.*, 115, 499-526, 2015.
2362 <https://doi.org/10.1016/j.atmosenv.2014.10.021>
- 2363 Makar, P.A., Gong, W., Milbrandt, J., Hogrefe, C., Zhang, Y., Curci, G., Žabkar, R., Im, U. Balzarini, A.,
2364 Baro, R., Bianconi, R., Cheung, P., Forkel, R., Gravel, S., Hirtl, M., Honzak, L., Hou, A.,
2365 Jiménez-Guerrero, P., Langer, M., Moran, M.D., Pabla, B., Pérez, J.L., Pirovano, G., San José,
2366 R., Tuccella, P., Werhahn, J., Zhang, J., and Galmarini, S., Feedbacks between air pollution and
2367 weather, Part 1: Effects on weather, *Atm. Env.*, 115, 442-469, 2015.
2368 <https://doi.org/10.1016/j.atmosenv.2014.12.003>
- 2369 Makar, P.A., Nissen, R., Teakles, A., Zhang, J., Zheng, J., Zheng, Q., Moran, M.D., Yau, H., diCenzo, C.,
2370 Turbulent transport, emissions and the role of compensating errors in chemical transport models,
2371 *Geosci. CMAQ (Hertfordshire)ev.*, 7, 1001–1024, 2014. [https://doi.org/10.5194/gmd-7-1001-](https://doi.org/10.5194/gmd-7-1001-2014)
2372 [2014](https://doi.org/10.5194/gmd-7-1001-2014)
- 2373 Makar, P.A., Vouchet, V.S., Nenes, A., Inorganic chemistry calculations using HETV—a vectorized
2374 solver for the SO_4^{2-} - NO_3^- - NH_4^+ system based on the ISORROPIA algorithms, *Atm. Env.*, 37,
2375 2279-2294, 2003. [https://doi.org/10.1016/S1352-2310\(03\)00074-8](https://doi.org/10.1016/S1352-2310(03)00074-8)
- 2376 Makar, P.A., Wiebe, H.A., Staebler, R.M., Li, S.M. and Anlauf, K., Measurement and modeling of
2377 particle nitrate formation, *J. Geophys. Res. Atm.*, 103, 13095-13110, 1998.
2378 <https://doi.org/10.1029/98JD00978>
- 2379 Manders, A. M. M., Builjtes, P. J. H., Curier, L., Denier van der Gon, H. A. C., Hendriks, C., Jonkers, S.,
2380 Kranenburg, R., Kuenen, J. J. P., Segers, A. J., Timmermans, R. M. A., Visschedijk, A. J. H.,
2381 Wichink Kruit, R. J., van Pul, W. A. J., Sauter, F. J., van der Swaluw, E., Swart, D. P. J., Douros,
2382 J., Eskes, H., van Meijgaard, E., van Ulft, B., van Velthoven, P., Banzhaf, S., Mues, A. C., Stern,
2383 R., Fu, G., Lu, S., Heemink, A., van Velzen, N., and Schaap, M., Curriculum vitae of the
2384 LOTOS–EUROS (v2.0) chemistry transport model, *Geosci. CMAQ (Hertfordshire)ev.*, 10, 4145–
2385 4173, 2017. <https://doi.org/10.5194/gmd-10-4145-2017>
- 2386 Marchuk, G.I., Splitting and alternating direction methods, *Handbook of Numerical Analysis*, 1, 197-462,
2387 1990.
- 2388 Massad, R. S., Nemitz, E., & Sutton, M. A., Review and parameterization of bi-directional ammonia
2389 exchange between vegetation and the atmosphere. *Atmospheric Chemistry and Physics*, 10(21),
2390 10,359–10,386, 2010. <https://doi.org/10.5194/acp-10-10359-2010>
- 2391 McDonnell, T.C., C.T. Driscoll, T.J. Sullivan, D.A. Burns, B.P. Baldigo, S. Shao, G.B. Lawrence,
2392 Regional target loads of atmospheric nitrogen and sulfur deposition for the protection of stream
2393 and watershed soil resources of the Adirondack Mountains, USA. *Environmental Pollution* 281,
2394 117110, 2021. <https://doi.org/10.1016/j.envpol.2021.117110>
- 2395 McDonnell, T.C., Cosby, B. J., and Sullivan, T. J., Regionalization of soil base cation weathering for
2396 evaluating stream water acidification in the Appalachian Mountains, USA. *Environmental*
2397 *Pollution*, 162: 338-344, 2012. <https://doi.org/10.1016/j.envpol.2011.11.025>.
- 2398 McDonnell, T.D., Sullivan, T. J., Hessburg, P.F., Reynolds, K.M., Povak, N.A., Cosby, B. J., Jackson,
2399 W., and Salter, R.B., Steady-state sulfur critical loads and exceedances for protection of aquatic
2400 ecosystems in the U.S. southern Appalachian Mountains. *Journal of Environmental Management*
2401 146 (2014) 407-419, 2014. <http://dx.doi.org/10.1016/j.jenvman.2014.07.019>
- 2402 McNulty, S. G., Cohen, E. C., & Myers, J. A. M., Climate change impacts on forest soil critical acid
2403 loads and exceedances at a national scale. In: Potter, Kevin M.; Conkling, Barbara L., Eds.
2404 *Forest Health Monitoring: National Status, Trends, and Analysis 2010*. Gen. Tech. Rep. SRS-
2405 GTR-176. Asheville, NC: U.S. Department of Agriculture Forest Service, Southern Research
2406 Station. 95-108., 176, 95–108, 2013.
- 2407 McNulty, S. G., Cohen, E. C., Moore Myers, J. A., Sullivan, T. J., & Li, H., Estimates of critical acid
2408 loads and exceedances for forest soils across the conterminous United States. *Environmental*
2409 *Pollution*, 149(3), 281–292, 2017. <https://doi.org/10.1016/j.envpol.2007.05.025>



- 2410 Milbrandt, J. A. and Morrison, H., Parameterization of Cloud Microphysics Based on the Prediction of
2411 Bulk Ice Particle Properties. Part III: Introduction of Multiple Free Categories, *J. Atmos. Sci.*, 73,
2412 975-995, 2016. <https://doi.org/10.1175/JAS-D-15-0204.1>
- 2413 Miller, E., *Steady-state critical loads and exceedances for terrestrial and aquatic ecosystems in the*
2414 *northeastern United States*. Technical report, National Park Service, Air Resources Division,
2415 2011.
- 2416 Miller, S.J., Makar, P.A., and Lee, C.J., HETerogeneous vectorized or Parallel (HETPv1.0): An updated
2417 inorganic heterogeneous chemistry solver for metastable state $\text{NH}_4^+ - \text{Na}^+ - \text{Ca}^{2+} - \text{K}^+ - \text{Mg}^{2+} - \text{SO}_4^{2-} -$
2418 $\text{NO}_3^- - \text{Cl}^-$ based on ISORROPIA II, *Geo. Mod. Dev.*, 17, 2197-2219, 2024.
2419 <https://doi.org/10.5194/gmd-17-2197-2024>.
- 2420 Morrison, H. and Milbrandt, J. A., Parameterization of Cloud Microphysics Based on the Prediction of
2421 Bulk Ice Particle Properties. Part I: Scheme Description and Idealized Tests, *J. Atmos. Sci.*, 72,
2422 287-311, 2015. <https://doi.org/10.1175/JAS-D-14-0065.1>
- 2423 Morrison, H., Thompson, G., and Tatarskii, V., Impact of cloud microphysics on the development of
2424 trailing stratiform precipitation in a simulated squall line: comparison of one- and two-moment
2425 schemes, *Mon. Weather Rev.*, 137, 991-1007, 2009. <https://doi.org/10.1175/2008MWR2556.1>
- 2426 Nakanishi, M. and Niino, H., An Improved Mellor-Yamada Level-3 Model: Its Numerical Stability and
2427 Application to a Regional Prediction of Advection Fog, *Bound.-Lay. Meteorol.*, 119, 397-407,
2428 2006. <https://doi.org/10.1007/s10546-005-9030-8>
- 2429 Nenes, A., Pandis, S.N., and Pilinis, C., Isorropia: A new thermodynamic equilibrium model for
2430 multiphase multicomponent inorganic aerosols, *Aquatic Geochemistry*, 4, 123-152, 1998.
2431 <https://doi.org/10.1023/A:1009604003981>
- 2432 Neu, J. L. and Prather, M. J., Toward a more physical representation of precipitation scavenging in global
2433 chemistry models: cloud overlap and ice physics and their impact on tropospheric ozone, *Atmos.*
2434 *Chem. Phys.*, 12, 3289-3310, 2012. <https://doi.org/10.5194/acp-12-3289-2012>
- 2435 Nilsson, J., and Grennfelt, P., Critical loads for sulphur and nitrogen, in: Report from a workshop held at
2436 Skokloster, Sweden 19-24 March 1988, J. Nilsson, Ed., Miljörappport, Volume 15 of Nordic
2437 Council of Ministers-Publications-Nord, 418pp, 1988.
- 2438 Niu, G-Y., Yang, Z-L., Mitchell, K.E., Ek, M.B., Barlage, M., Kumar, A., Manning, K., Niyogi, D.,
2439 Rosero, E., Tewari, M., Xia, Y., The community Noah land surface model with
2440 multiparameterization options (Noah-MP): 1. Model description and evaluation with local-scale
2441 measurements, *J. Geophys. Res.*, 116, D12109, 2011. <https://doi.org/10.1029/2010JD015139>
- 2442 Ott, L.E., Pickering, K.E., Stenchikov, G.L., Allen, D.J., DeCaria, A.J., Ridley, B., Line, R-F., Lang, S.,
2443 and Tao, W-K., Production of lightning NO_x and its vertical distribution calculated from three-
2444 dimensional cloud-scale chemical transport model simulations, *J. Geophys. Res. Atm.*, 115,
2445 D04301, 2010. <https://agupubs.onlinelibrary.wiley.com/doi/full/10.1029/2009JD011880>
- 2446 Paulot, F., Jacob, D.J., Johnson, M.T., Bell, T.G., Baker, A.R., Keene, W.C., Lima, I.D., Doney, S.C.,
2447 Stock, C.A., Global oceanic emission of ammonia: Constraints from seawater and atmospheric
2448 observations, *Global Geochem. Cycles*, 29, 1165-1178, 2015.
2449 <https://doi.org/10.1002/2015GB005106>
- 2450 Paulot, F., Malyshev, S., Nguyen, T., Crouse, J. D., Shevliakova, E., & Horowitz, L. W., Representing
2451 sub-grid scale variations in nitrogen deposition associated with land use in a global Earth system
2452 model: implications for present and future nitrogen deposition fluxes over North America.
2453 *Atmospheric Chemistry and Physics*, 18(24), 17963-17978, 2018. [https://doi.org/10.5194/acp-18-](https://doi.org/10.5194/acp-18-17963-2018)
2454 [17963-2018](https://doi.org/10.5194/acp-18-17963-2018)
- 2455 Paulot, F., Stock, C., John, J.G., Zadeh, N., Horowitz, L.W., Ocean Ammonia Outgassing: Modulation by
2456 CO₂ and Anthropogenic Nitrogen Deposition, *J. Adv. Mod. Earth Sys.*, 12, e2019MS002026,
2457 2020. <https://doi.org/10.1029/2019MS002026>
- 2458 Pleim, J. E., Ran, L., Appel, W., Shephard, M. W., & Cady-Pereira, K., New bidirectional ammonia flux
2459 model in an air quality model coupled with an agricultural model, *Journal of Advances in*
2460 *Modeling Earth Systems*, 11, 2934-2957, 2019. <https://doi.org/10.1029/2019MS0017282934>



- 2461 Pleim, J. E., Ran, L., Saylor, R. D., Willison, J., & Binkowski, F. S. (2022). A new aerosol dry deposition
2462 model for air quality and climate modeling. *Journal of Advances in Modeling Earth Systems*, 14,
2463 e2022MS003050. <https://doi.org/10.1029/2022MS003050>
- 2464 Posch, M., de Smet, P. A., Hettelingh, J.-P., & Downing, R. J., *Modelling and mapping of critical*
2465 *thresholds in Europe: Status Report 2001*. Citeseer.
2466 [https://citeseerx.ist.psu.edu/document?repid=rep1&type=pdf&doi=a585c6eff5f0c93938e4ef2187](https://citeseerx.ist.psu.edu/document?repid=rep1&type=pdf&doi=a585c6eff5f0c93938e4ef21874d4dc9425fd282)
2467 [4d4dc9425fd282](https://citeseerx.ist.psu.edu/document?repid=rep1&type=pdf&doi=a585c6eff5f0c93938e4ef21874d4dc9425fd282), last accessed December 22, 2023.
- 2468 Pruppacher, H.R., Klett, J.D., Growth of Cloud Drops by Collision and Coalescence. In: *Microphysics of*
2469 *Clouds and Precipitation*. Springer, Dordrecht., 1978. [https://doi.org/10.1007/978-94-009-9905-](https://doi.org/10.1007/978-94-009-9905-3_15)
2470 [3_15](https://doi.org/10.1007/978-94-009-9905-3_15)
- 2471 Ran, L., E. Cooter, D. Yang, V. Benson, Y. Yuan, A. Hanna, AND V. Garcia. User's Guide for the
2472 Fertilizer Emission Scenario Tool for CMAQ (FEST-C) Version 1.4. U.S. EPA Office of
2473 Research and Development, Washington, DC, 2018. [https://www.cmascenter.org/fest-](https://www.cmascenter.org/fest-c/documentation/1.4/FESTC_v1_4_UserManual.pdf)
2474 [c/documentation/1.4/FESTC_v1_4_UserManual.pdf](https://www.cmascenter.org/fest-c/documentation/1.4/FESTC_v1_4_UserManual.pdf)
- 2475 Reinds G.J., Thomas D., Posch M., Slootweg J., Critical loads for eutrophication and acidification for
2476 European terrestrial ecosystems. Final report. Dessau-Roßlau, 2021.
2477 <https://pure.iiasa.ac.at/id/eprint/17341/>
- 2478 Reinds, G., Posch, M., Aheme, J., Forsius, M., Assessment of Critical Loads of Sulphur and Nitrogen and
2479 Their Exceedances for Terrestrial Ecosystems in the Northern Hemisphere. In: de Vries, W.,
2480 Hettelingh, J.P., Posch, M. (eds) *Critical Loads and Dynamic Risk Assessments*. Environmental
2481 Pollution, vol 25. Springer, Dordrecht, 2015. https://doi.org/10.1007/978-94-017-9508-1_15
- 2482 Russell, A.G., McRae, G.J., and Cass, G.R., The dynamics of nitric acid production and the fate of
2483 nitrogen oxides, *Atm. Env.*,(1967) 19893-903, 1985.
- 2484 Ryu, Y.-H., & Min, S.-K., Improving wet and dry deposition of aerosols in WRF-Chem: Updates to
2485 below-cloud scavenging and coarse-particle dry deposition. *Journal of Advances in Modeling*
2486 *Earth Systems*, 14, e2021MS002792, 2022. <https://doi.org/10.1029/2021MS002792>
- 2487 Sandu, A. and Sander, R.: Technical note: Simulating chemical systems in Fortran90 and Matlab with the
2488 Kinetic PreProcessor KPP-2.1, *Atmos. Chem. Phys.*, 6, 187–195, 2006.
2489 <https://doi.org/10.5194/acp-6-187-2006>
- 2490 Scott, K., Wissel, B., Gibson, J., & Birks, S., Chemical characteristics and acid sensitivity of boreal
2491 headwater lakes in northwest Saskatchewan. *Journal of Limnology*, 69, 33–44, 2010.
2492 <https://doi.org/10.4081/jlimnol.2010.s1.33>
- 2493 Scheffe, R. D., Lynch, J. A., Reff, A., Hubbell, B., Greaver, T. L., and Smith, J. T., The Aquatic
2494 Acidification Index: A New Regulatory Metric Linking Atmospheric and Biogeochemical
2495 Models to Assess Potential Aquatic Ecosystem Recovery. *Water Air Soil Pollution*, 225:1838,
2496 2014. <https://doi.org/10.1007/s11270-013-1838-0>
- 2497 Shao, Y., Ishizuka, M., Mikami, M., and Leys, J. F.: Parameterization of size-resolved dust emission and
2498 validation with measurements, *J. Geophys. Res.*, 116, D08203, 2011.
2499 <https://doi.org/10.1029/2010JD014527>
- 2500 Simkin, S. M., Allen, E.B., Bowman, W.D., Clark, C.M., Belnap, J., Brooks, M.L., Cade, B.S., Collins,
2501 S.L., Geiser, L.H., Gilliam, F.S., Jovan, S.E., Pardo, L.H., Schulz, B.K., Stevens, C.I., Suding,
2502 K.N., Throop, H.L., and Waller, D.M., Conditional vulnerability of plant diversity to atmospheric
2503 nitrogen deposition across the United States, *Proc. Nat. Acad. Sci.*, 113(15), 4086-4091, 2016.
2504 <https://doi.org/10.1073/pnas.1515241113>
- 2505 Skamarock, W. C., J. B. Klemp, J. Dudhia, D. O. Gill, Z. Liu, J. Berner, W. Wang, J. G. Powers, M. G.
2506 Duda, D. M. Barker, and X.-Y. Huang, A Description of the Advanced Research WRF Version 4.
2507 NCAR Tech. Note NCAR/TN-556+STR, 145 pp., 2019. <https://doi.org/10.5065/1dfh-6p97>
- 2508 Slinn, W. G. N., Precipitation Scavenging, in *Atmospheric Science and Power Production*, CH. 11,
2509 edited by: 680 Randerson, D., Tech. Inf. Cent., Off. of Sci. and Techn. Inf., Dep. of Energy,
2510 Washington DC, USA, 466–532, 1984.



- 2511 Slinn, W. G. N., Predictions for particle deposition to vegetative canopies, *Atmos. Environ.*, 16, 1785–
2512 1794, 1982. [https://doi.org/10.1016/0004-6981\(82\)90271-2](https://doi.org/10.1016/0004-6981(82)90271-2)
- 2513 Solazzo, E., Riccio, A., Van Dingenen, R., Valentini, L., and Galmarini, S., Evaluation and uncertainty
2514 estimation of the impact of air quality modelling on crop yields and premature deaths using a
2515 multi-model ensemble, *Sci. Total Environ.*, 633, 1437–1452, 2018.
2516 <https://doi.org/10.1016/j.scitotenv.2018.03.317>
- 2517 Sorensen, B., Kaas, E., Korsholm, U.S., A mass-conserving and multi-tracer efficient transport scheme in
2518 the online integrated Enviro-HIRLAM model, *Geos. Mod. Dev.*, 6, 1029-1042, 2013.
2519 <https://doi.org/10.5194/gmd-6-1029-2013>
- 2520 Stockwell, W. R. and Lurmann, F. W.: Intercomparison of the ADOM and RADM gas-phase chemical
2521 mechanisms, Electric Power Institute Topical Report, Electric Power Institute, Palo Alto,
2522 California, 323 pp., 1989.
- 2523 Stroud, C. A., Makar, P. A., Zhang, J., Moran, M. D., Akingunola, A., Li, S.-M., Leithead, A., Hayden,
2524 K., and Siu, M.: Improving air quality model predictions of organic species using measurement-
2525 derived organic gaseous and particle emissions in a petrochemical-dominated region, *Atmos.*
2526 *Chem. Phys.*, 18, 13531–13545, 2018. <https://doi.org/10.5194/acp-18-13531-2018>
- 2527 Stroud, C., Moran, M., Makar, P., Gong, W., Gong, S., Mourneau, G., Bouchet, V., Dann, T., Wang, D.,
2528 and Huang, L, Impact of Updates to BEIS v3 Boreal Forest Emissions on Canadian Air Quality
2529 Forecasts, 2nd International Workshop on Air Quality Forecasting Research, Quebec, Canada,
2530 2010.
- 2531 Sullivan, T.J., Cosby, B.J., McDonnell, T.C., Porter, E.M., Blett, T., Haeuber, R., Huber, C.M., and
2532 Lynch, J., Critical loads of acidity to protect and restore acid-sensitive streams in Virginia and
2533 West Virginia. *Water Air Soil Pollution*, 223:5759-5771, 2012. [https://doi.org/10.1007/s11270-](https://doi.org/10.1007/s11270-012-1312-4)
2534 [012-1312-4](https://doi.org/10.1007/s11270-012-1312-4).
- 2535 Sullivan, T.J., Cosby, B.J., Tonnesen, K.A. and Clow, D.W., Surface water acidification responses and
2536 critical loads of sulfur and nitrogen deposition in Loch Vale watershed, Colorado. *WATER*
2537 *RESOURCES RESEARCH*, VOL. 41, W01021, 2005. <https://doi.org/10.1029/2004WR003414>
- 2538 Sundqvist, H., Berge, E., and Kristjansson, J.E., Condensation and cloud parameterization studies with a
2539 mesoscale numerical weather prediction model. *Mon. Wea. Rev.*, 117, 1641-1657, 1989.
2540 [https://doi.org/10.1175/1520-0493\(1989\)117<1641:CACPSW>2.0.CO;2](https://doi.org/10.1175/1520-0493(1989)117<1641:CACPSW>2.0.CO;2)
- 2541 Sverdrup, H. and de Vries, W., Calculating critical loads for acidity with the simple mass balance method,
2542 *Water Air Soil Poll.*, 72, 143–162, 1994. <https://doi.org/10.1007/BF01257121>
- 2543 Sverdrup, H., and Warfvinge, P., The role of weathering and forestry in determining the acidity of Lakes
2544 in Sweden. *Water, Air, and Soil Pollution*, 52(1), 71–78, 1990.
2545 <https://doi.org/10.1007/BF00283115>
- 2546 Sverdrup, H., De Vries, W., and Henriksen, A., *Mapping critical loads* (Miljörapport 14). Nordic Council
2547 of Ministers, 124pp., 1990.
- 2548 Timmermans, R., van Pinxteren, D., Kranenburg, R., Hendriks, C., Fomba, K. W., Herrmann, H., Schaap,
2549 M., Evaluation of modelled LOTOS-EUROS with observational based PM10 source attribution,
2550 *Atm. Env.:* X, 14, 100173, 2022. <https://doi.org/10.1016/j.aeaoa.2022.100173>
- 2551 US EPA 2020: US EPA Office of Research and Development, 2020: CMAQ (5.3.2). Zenodo.
2552 <https://doi.org/10.5281/zenodo.4081737>
- 2553 US EPA, 2023: NHDPlus (National Hydrography Dataset Plus), [https://www.epa.gov/waterdata/nhdplus-](https://www.epa.gov/waterdata/nhdplus-national-hydrography-dataset-plus)
2554 [national-hydrography-dataset-plus](https://www.epa.gov/waterdata/nhdplus-national-hydrography-dataset-plus), last accessed December 26, 2023.
- 2555 Van Zanten, M.C., Sauter, F.J., Wichink Kruit, R.J., Van Jaarsveld, J.A., Van Pul, W.A.J., Description of
2556 the DEPAC module: dry deposition modelling with DEPAC GCN2010 RIVM Rep., 2010.
2557 <https://rivm.openrepository.com/handle/10029/256555>
- 2558 VDEC, 2003: Vermont Department of Environmental Conservation (VDEC), (2003, 2004, 2012).
2559 TOTAL MAXIMUM DAILY LOADS: Acid Impaired Lakes. Watershed Management
2560 Division, 103 South Main Street, Building 10 North, Waterbury, VT 05671-0408.



- 2561 Vehkamäki, H., Kulmala, M., Napari, I., Lehtinen, K.E.J., Timmreck, C., Noppel, M., and Laaksonen, A.
2562 An improved parameterization for sulfuric acid – water nucleation rates for tropospheric and
2563 stratospheric conditions, *J. Geophys. Res.*,107(D22),4622, 2002.
2564 <https://doi.org/10.1029/2002JD002184>
- 2565 Venkatram, A., and Pleim, J., The electrical analogy does not apply to modeling dry deposition of
2566 particles, *Atm. Env.*, 33, 3075-3076, 1999. [https://doi.org/10.1016/S1352-2310\(99\)00094-1](https://doi.org/10.1016/S1352-2310(99)00094-1)
- 2567 Vivanco, M. G., Theobald, M. R., García-Gómez, H., Garrido, J. L., Prank, M., Aas, W., Adani, M.,
2568 Alyuz, U., Andersson, C., Bellasio, R., Bessagnet, B., Bianconi, R., Bieser, J., Brandt, J.,
2569 Briganti, G., Cappelletti, A., Curci, G., Christensen, J. H., Colette, A., Couvidat, F., Cuvelier, C.,
2570 D'Isidoro, M., Flemming, J., Fraser, A., Geels, C., Hansen, K. M., Hogrefe, C., Im, U., Jorba, O.,
2571 Kitwiroon, N., Manders, A., Mircea, M., Otero, N., Pay, M.-T., Pozzoli, L., Solazzo, E., Tsyro,
2572 S., Unal, A., Wind, P., and Galmarini, S., Modeled deposition of nitrogen and sulfur in Europe
2573 estimated by 14 air quality model systems: evaluation, effects of changes in emissions and
2574 implications for habitat protection, *Atmos. Chem. Phys.*, 18, 10199– 10218, 2018.
2575 <https://doi.org/10.5194/acp-18-10199-2018>
- 2576 Vizuete, W., Nielsen-Gammon, J., Dickey, J., Couzo, E., Blanchard, C., and Breitenbach, P.,
2577 Meteorological based parameters and ozone exceedances in Houston and other cities in Texas, *J.*
2578 *Air & Waste Man.*, 72, 969-984, 2002. <https://doi.org/10.1080/10962247.2022.2064004>
- 2579 Vukovich, J.M., and Pierce, T., The Implementation of BEIS3 within the SMOKE modeling framework,
2580 Proceedings of the 11th International Emissions Inventory Conference, Atlanta, Georgia, USA ,
2581 2002. <https://www.epa.gov/sites/default/files/2015-10/documents/vukovich.pdf>
- 2582 Wang, X., L. Zhang, and M. D.: Moran Development of a new semi-empirical parameterization for
2583 below-cloud scavenging of size resolved aerosol particles by both rain and snow, *Geosci. CMAQ*
2584 (Hertfordshire)ev., 7, 799–819, 2014. <https://doi.org/10.5194/gmd-7-799-2014>
- 2585 Wesely, M. L., Parameterization of surface resistances to gaseous dry deposition in regional-scale
2586 numerical models. *Atmospheric Environment* (1967), 23(6), 1293– 1304, 1989.
2587 [https://doi.org/10.1016/0004-6981\(89\)90153-4](https://doi.org/10.1016/0004-6981(89)90153-4)
- 2588 Wesely, M.L., Parameterization of surface resistances to gaseous dry deposition in regional-scale
2589 numerical models, *Atmospheric Environment*, 23, 1293-1304, 1989.
2590 <https://doi.org/10.1016/j.atmosenv.2007.10.058>
- 2591 Whitfield, C. J., Aherne, J., Watmough, S. A., Dillon, P. J., & Clair, T. A., Recovery from acidification in
2592 Nova Scotia: Temporal trends and critical loads for 20 headwater lakes. *Canadian Journal of*
2593 *Fisheries and Aquatic Sciences*, 63(7), 1504–1514, 2016. <https://doi.org/10.1139/f06-053>
- 2594 Whitten, G., Hogo, H., Killus, J., The carbon bond mechanism for photochemical smog, *Environ. Sci.*
2595 *Technol.*, 14, pp. 14690-14700, 1980.
- 2596 Wichink Kruit, R.J., Schaap, M., Sauter, F.J., van Zanten, W.A.J., van Pul, M.C., Modeling the
2597 distribution of ammonia across Europe including bi-directional surface–atmosphere exchange
2598 *Biogeosciences*, 9, 5261-5277, 2012. <https://doi.org/10.5194/bg-9-5261-2012>
- 2599 Wiedinmyer, C., Sakulyanontvittaya, T., and Guenther, A. , MEGAN FORTRAN code v2.04 User Guide ,
2600 2007. <https://www.acom.ucar.edu/webt/MEGAN/MEGANguideFORTRAN204.pdf> last accessed
2601 Dec 12, 2023.
- 2602 Williams, J. R., The EPIC model. In V. P. Singh (Ed.), *Computer models in watershed hydrology* (Chapter
2603 25, (pp. 909–1000), 1995. Littleton, CO: Water Resources Publications.
- 2604 Williston, P., Aherne, J., Watmough, S., Marmorek, D., Hall, A., de la Cueva Bueno, P., Murray, C.,
2605 Henolson, A., & Laurence, J. A., Critical levels and loads and the regulation of industrial
2606 emissions in northwest British Columbia, Canada. *Atmospheric Environment*, 146, 311–323,
2607 2016. <https://doi.org/10.1016/j.atmosenv.2016.08.058>
- 2608 Wu, Z., Schwede D. B., Vet R., Walker J. T., Shaw M., Staebler R., and Zhang L.: Evaluation and
2609 intercomparison of five North American dry deposition algorithms at a mixed forest site, *J. Adv.*
2610 *Model. Earth Sy.*, 10, 1571–1586, <https://doi.org/10.1029/2017MS001231>, 2018.



- 2611 Xu, L., Pye, H. O. T., He, J., Chen, Y. L., Murphy, B. N., Ng, N. L., Experimental and model estimates
2612 of the contributions from biogenic monoterpenes and sesquiterpenes to secondary organic aerosol
2613 in the southeastern United States. *Atmos. Chem. Phys.*, 18: 12613-12637, 2018.
2614 <https://doi.org/10.5194/acp-18-12613-2018>
- 2615 Yarwood, G., Jung, J., Whitten, G., Heo, G., J. M., and M, E.: Updates to the Carbon Bond Mechanism
2616 for Version 6 (CB6), in: 9th Annual CMAS Conference, Chapel Hill, NC, 11–13 October 2010,
2617 pp. 1–4, 2010.
2618 https://cmasceneter.org/conference/2010/abstracts/emery_updates_carbon_2010.pdf Young, T.R.
2619 and Boris, J.P., A numerical technique for solving stiff ordinary differential equations associated
2620 with the chemical kinetics of reactive-flow problems., *J. Phys. Chem.*, 81, 2424-2427, 1977.
- 2621 Zaveri, R. A., Easter, R. C., Fast, J. D., and Peters, L. K.: Model for Simulating Aerosol Interactions and
2622 Chemistry (MOSAIC), *Journal of Geophysical Research*, 113, D13 204, 2008.
2623 <https://doi.org/10.1029/2007JD008782>
- 2624 Zaveri, R.A., and L.K. Peters, A new lumped structure photochemical mechanism for large-scale
2625 applications, *J. Geophys. Res.*, 104, 30,387 - 30,415, 1999.
2626 <https://doi.org/10.1029/1999JD900876>
- 2627 Zhang, J., Moran, M.D., Makar, P.A., and Kharol, S., Examination of MODIS Leaf Area Index (LAI)
2628 Product for Air Quality Modelling, 19th Annual CMOS Conference, 2020,
2629 https://www.cmasceneter.org/conference/2020/slides/ZhangJ_MODIS_LAI_CMAS_2020.pdf, last
2630 accessed December 19, 2023.
- 2631 Zhang, L., Brook, J. R., and Vet, R.: A revised parameterization for gaseous dry deposition in air-quality
2632 models, *Atmos. Chem. Phys.*, 3(6), 2067–2082, 2003. <https://doi.org/10.5194/acp-3-2067-2003>
- 2633 Zhang, L., Gong, S., Padro, J., & Barrie, L., A size-segregated particle dry deposition scheme for an
2634 atmospheric aerosol module. *Atmos-pheric Environment*, 35(3), 549–560, 2001.
2635 [https://doi.org/10.1016/S1352-2310\(00\)00326-5](https://doi.org/10.1016/S1352-2310(00)00326-5)
- 2636 Zhang, L., Gong, S., Padro, J., and Barrie, L.: A size-segregated particle dry deposition scheme for an
2637 atmospheric aerosol module, *Atmos. Environ.*, 35, 549–560, 2001. [https://doi.org/10.1016/S1352-
2638 2310\(00\)00326-5](https://doi.org/10.1016/S1352-2310(00)00326-5)
- 2639 Zhang, L., Moran, M. D., Makar, P. A., Brook, J.R., and Gong, S.: Modelling gaseous dry deposition in
2640 AURAMS: a unified regional air-quality modelling system, *Atmos. Environ.*, 36(3), 537–560,
2641 2002. [https://doi.org/10.1016/S1352-2310\(01\)00447-2](https://doi.org/10.1016/S1352-2310(01)00447-2), 2002.
- 2642 Zhang, L., Wright, L. P., and Asman, W. A. H.: Bi-directional air-surface exchange of atmospheric
2643 ammonia: A review of measurements and a development of a big-leaf model for applications in
2644 regional-scale air-quality models, *J. Geophys. Res.*, 115, D20310, 2010.
2645 <https://doi.org/10.1029/2009JD013589>